

AD A058 612

2003 1028 163

Unclassified

SECURITY CLASSIFICATION OF THIS PAGE (When Data Entered)

19 REPORT DOCUMENTATION PAGE		READ INSTRUCTIONS BEFORE COMPLETING FORM
1 REPORT NUMBER NCSC/TM-238-78 ✓	2. GOVT ACCESSION NO.	3 RECIPIENT'S CATALOG NUMBER
4 TITLE (and Subtitle) METHODS FOR PREDICTING SUBMERSIBLE HYDRODYNAMIC CHARACTERISTICS.		5. TYPE OF REPORT & PERIOD COVERED Final Technical Report 5/10/76 - 7/10/77
7 AUTHOR(s) John E./Fidler Charles A./Smith		14 6. PERFORMING ORG. REPORT NUMBER NEAR-TR-139 ✓
9 PERFORMING ORGANIZATION NAME AND ADDRESS Nielsen Engineering & Research, Inc. 510 Clyde Avenue Mountain View, CA 94043		15 8. CONTRACT OR GRANT NUMBER(s) N61339-76-C-0076
11 CONTROLLING OFFICE NAME AND ADDRESS Naval Coastal System Laboratory Panama City, Florida 32407		10. PROGRAM ELEMENT PROJECT, TASK AREA & WORK UNIT NUMBERS None 12 179 p.
14 MONITORING AGENCY NAME & ADDRESS (if different from Controlling Office) Same		13 REPORT DATE 11 July 1978
		16 SECURITY CLASS. (of this report) Unclassified
18 DISTRIBUTION STATEMENT (of this Report) Approved for public release, distribution unlimited		17 NUMBER OF PAGES 179
17 DISTRIBUTION STATEMENT (of the abstract entered in Block 20, if different from Report) N/A		18a DECLASSIFICATION/DOWNGRADING SCHEDULE N/A
10 SUPPLEMENTARY NOTES None		9 Final technical report. 19 May 76 - 10 Jul 77.
19 KEY WORDS (Continue on reverse side if necessary and identify by block number) Hydrodynamic Configurations Wind tunnels Submersibles Testing Predictions Methods		DDO SEP 14 1978 A
20 ABSTRACT (Continue on reverse side if necessary and identify by block number) Methods were constructed for predicting the hydrodynamic characteristics of submersible vehicles in pitching attitudes with undeflected tailfins. An extensive set of models was built, representing the geometries of a wide range of submersibles. These models were then tested in a wind tunnel to obtain systematic data over relevant ranges of attitudes and flow conditions. The data were then used, coupled with		

Block No. 20. (continued)

→ theoretical results, to develop the prediction methods. The methods deal with the characteristics of individual vehicle components (bodies, tails), and with their mutual interactions when combined into complete configurations. Each method is presented in self-contained form, along with directions for its use. It is shown that the methods provide good accuracy for prediction of hydrodynamic characteristics.



Unclassified

SUMMARY

This document describes the construction of methods for predicting the hydrodynamic characteristics of submersible vehicles in pitching attitudes with undeflected tailfins. Following an approach used successfully in missile aerodynamics, a set of models was built and tested to obtain systematic data over relevant ranges of geometry and flow conditions. These data were then used, in conjunction with theoretical results, to develop the prediction methods. The methods deal with the characteristics of individual vehicle components (bodies, tails) and with their mutual interactions when combined into complete configurations. Each method is presented in self-contained form, along with directions for its use. It is shown that the methods provide good accuracy for prediction of hydrodynamic characteristics.

ACQUISITION NO.	
KEY	White Section <input checked="" type="checkbox"/>
REF	Left Section <input type="checkbox"/>
DATE	
BY	
APPROVED FOR RELEASE	
CLASS. AND EXT. USE	
A	

NOMENCLATURE

a_0	coefficient of zero-order term in expression for nondimensional load or moment
a_1	coefficient of first-order term in expression for nondimensional load or moment
a_2	coefficient of second-order term in expression for nondimensional load or moment
AR	fin aspect ratio - two panels
b	total span of two fin panels placed together
b_v	distance between vortices or span of vortex wake
B_1	conical base section, 1 caliber in length
B_2	conical base section, 2 calibers in length
B_3	conical base section, 3 calibers in length
C_y	fin local chord length
C_{d_c}	crossflow drag coefficient
C_f	turbulent flat plate skin-friction coefficient based on exposed surface area, S_w
C_l	rolling moment coefficient
C_{o_b}	base drag coefficient
C_{o_f}	skin-friction drag coefficient, based on S_R
C_A	axial-force coefficient
C_L	lift coefficient

NCSC TM-238-78

NOMENCLATURE - CONTINUED

C_M	pitching-moment coefficient
C_N	normal-force coefficient
C_R	fin root chord
C_T	fin tip chord
CA	cylindrical center section, 2-1/2 calibers in length
CB	cylindrical center section, 1-1/2 calibers in length
CC	cylindrical center section, 3 calibers in length
C1	cylindrical center section, 2-1/2 calibers in length, consisting of CA
C2	cylindrical center section, 4 calibers in length, consisting of CA + CB
C3	cylindrical center section, 5-1/2 calibers in length, consisting of CA + CC
C4	cylindrical center section, 7 calibers in length, consisting of CA + CB + CC
d	maximum diameter of body cross section; also reference length
d_b	diameter of effective or equivalent base (i.e., diameter of base section of body where the axial flow separates)
f	transverse force per unit length
$f_1(r_o/s)$	multiplicative factor used in $C_{NB(T)}$ for effect of fin span
$f_2(\lambda)$	multiplicative factor used in $C_{NB(T)}$ for effect of fin taper ratio
$f_3(l_{LE}/d)$	multiplicative factor used in $C_{NB(T)}$ for effect of fin position

NOMENCLATURE - CONTINUED

K_m	empirical factor used in C_{M_B}
$K_{B(T)}$	
$K_{T(B)}$	ratio of normal force curve slopes: tail on body/tail alone
$K_2 - K_1$	apparent mass factor of Munk
l	length
l_{sa}	length of body exposed to potential flow (i.e., distance from nose to x_{sa})
l_{LE}	axial distance from start of base section to fin root chord leading edge
NF	normal force
N1	hemispherical nose
N2	ellipsoidal nose, 1 caliber in length
N3	ellipsoidal nose, 2 calibers in length
q	dynamic pressure, $\rho_\infty V_\infty^2 / 2$
r	local body radius
r_0	maximum radius of body
r_1	body radius at fin leading edge
r_2	body radius at fin trailing edge
$R_{T(B)}$	ratio of normal forces: tail on body/tail alone = $C_{N_{T(B)}} / C_{N_T}$
R_0	constant term of tail normal-force amplification factor
R_1	first order term of tail normal-force amplification factor

NOMENCLATURE - CONTINUED

Re	Reynolds number based on body length
Re_{CR}	Reynolds number based on root chord of fin
Re_d	Reynolds number based on body maximum cross-sectional diameter
Re_n	crossflow Reynolds number, $V_\infty ds \sin \alpha / \nu$
Re_{sa}	Reynolds number based on length of body exposed to potential flow
RM	rolling moment
s	fin maximum semispan measured from body centerline
S	local cross-sectional area of body
S_b	cross-sectional area of equivalent base, $\pi d_b^2 / 4$
S_p	area of body planform
S_{pc}	planform area of portion of body in separated crossflow (i.e., from x_{sc} to end of body)
S_R	maximum area of body cross section, $\pi d^2 / 4$, reference area
S_T	fin planform area, single panel
S_w	surface area of body
V_B	body volume
V_∞	free-stream velocity
x	axial or chordwise coordinate
\bar{X}	axial distance to center of pressure
x_m	axial location of moment reference center
x_{sa}	axial location, measured from beginning of body base section, where the axial flow separates

NOMENCLATURE - CONTINUED

x_{sc}	axial distance on body, measured from nose, where crossflow begins to separate
\bar{X}_N	center of pressure of body carryover loading, $C_{NB(T)}$
y	lateral co-ordinate
\bar{Y}	lateral distance to center of pressure
α	angle of attack
α_u	angle of attack of upwash flow
Γ	vortex strength
δ	tail deflection
Δ	incremental contribution; used in $R_{T(B)}$ development
$\Delta\bar{X}$	correction to \bar{X}_T to give $\bar{X}_{T(B)}$
η	correction for three-dimensional effects on body crossflow drag
λ	fin taper ratio
ρ_∞	free-stream density
σ	complex distance between a vortex and its image inside a cylinder

Subscripts

A	aft tail location
R	incremental contribution due to fin aspect ratio effects; used in $R_{T(B)}$ development
b	base
B	body

NOMENCLATURE - CONCLUDED

BT	complete body-tail combination
B(T)	carryover on the body, in the presence of the tails
c	centroid of body region between fins
C	center section
d/b	contribution attributed to span effects; used in $R_{T(B)}$ development
F	forebody, or forward tail location
l	incremental contribution due to location of fin on base section; used in $R_{T(B)}$ development
LE	denotes value at leading edge of root chord
M	mid tail location
nl	non-linear term
N	nose
pot	potential term
Re	incremental contribution due to Reynolds number effects; used in $R_{T(B)}$ development
T	tail alone
T(B)	tail, in the presence of the body
o	denotes value at zero angle of attack
α	denotes differentiation with respect to α
λ	incremental contribution due to fin taper ratio effects; used in $R_{T(B)}$ development

(Reverse Page 8 Blank)

TABLE OF CONTENTS		<u>Page</u>
<u>Section</u>		
FOREWORD		1
SUMMARY		1
NOMENCLATURE		2
LIST OF ILLUSTRATIONS		11
I. INTRODUCTION		17
II. MODELS		19
III. WIND TUNNEL TESTS		31
IV. FORMULATIONS		35
V. ISOLATED BODIES		39
1. General Considerations		39
2. Body-Alone Normal Force Coefficient		44
3. Body-Alone Pitching Moment Coefficient		56
4. Body-Alone Axial Force Coefficient		70
VI. ISOLATED TAILS		81
1. General Considerations		81
2. Tail-Alone Normal Force Coefficient		81
3. Tail-Alone Chordwise Center of Pressure		98
VII. COMPLETE CONFIGURATIONS		111
1. General Considerations		111
2. Body Carryover Normal Force Coefficient		113
3. Body Carryover Load Center of Pressure		120
4. Tail Normal Force Amplification Factor		122
5. Tail-on-Body Chordwise Center of Pressure		140
6. Tail-on-Body Spanwise Center of Pressure		144
7. Use of Methods to Predict Complete Configuration Characteristics		153

<u>Section</u>	<u>Page</u>
VIII. CONCLUSIONS AND RECOMMENDATIONS	173
REFERENCES	.75

LIST OF ILLUSTRATIONS

<u>Figure</u>		<u>Page</u>
1	Nose shapes.	20
2	Center sections.	21
3	Base B2.	22
4	Tail geometry.	24
5	Reflection plane.	25
6	Tail balance.	26
7	Model noses.	27
8	Model bases.	28
9	Tail geometries.	29
10	Model pieces in sequence.	30
11	Tail on reflection plane.	34
12	Body alone Model N2C1B2.	34
13	Body tail Model N2C2B2T11 _A .	34
14	Symmetric vortex wake (from ref. 3).	40
15	Oil flow photograph of base B1.	42
16	Oil flow photograph of base B1.	43
17	Position of axial flow separation based on normal force curve slope.	47
18	Variation of crossflow drag coefficient with crossflow Reynolds number for circular cylinders (ref. 9).	49
19	Body configuration N2C2B2.	51
20	Comparison between predicted and experimental body-alone normal force coefficient.	53

LIST OF ILLUSTRATIONS (CONTINUED)

<u>Figure</u>		<u>Page</u>
21	Comparison between predicted and experimental body-alone normal force coefficient.	54
22	Comparison between predicted and experimental body-alone normal force coefficient.	55
23	Body-vortex characteristics - vortex strength (ref. 8).	59
24	Body-vortex characteristics - horizontal vortex position (ref. 8).	60
25	Apparent mass factor (from ref. 5).	62
26	Empirical factor used in pitching-moment-curve slope.	62
27	Ratio crossflow-drag coefficient for a finite length cylinder to that for an infinite length cylinder (from ref. 12).	63
28	Comparison between predicted and experimental body-alone pitching-moment coefficient.	67
29	Comparison between predicted and experimental body-alone pitching-moment coefficient.	68
30	Comparison between predicted and experimental body-alone pitching-moment coefficient.	69
31	Zero-angle base drag vs. afterbody fineness ratio.	72
32	Skin friction drag coefficient on plane surface in incompressible flow (ref. 14).	73
33	First order term for body-alone axial force coefficient.	75
34	Comparison between predicted and experimental body-alone axial force coefficient.	77

LIST OF ILLUSTRATIONS (CONTINUED)

<u>Figure</u>		<u>Page</u>
35	Comparison between predicted and experimental body-alone axial force coefficient.	78
36	Comparison between predicted and experimental body-alone axial force coefficient.	79
37	Vortex formation on low aspect ratio tail.	82
38	Measured values of lift-curve slope.	84
39	Effect of cropping trailing edge on lift curve slope (ref. 16).	86
40(a)	Curve for lift-curve slope prediction for blunt trailing edges.	87
40(b)	Curves for lift-curve slope prediction for sharp trailing edges.	88
41(a)	Recommended curves for prediction of a_2 , coefficient of nonlinear term of tail-alone normal force coefficient. $\lambda = 1.0$	90
41(b)	Recommended curves for prediction of a_2 , coefficient of nonlinear term of tail-alone normal force coefficient. $\lambda = 0.5$	91
41(c)	Recommended curves for prediction of a_2 , coefficient of nonlinear term of tail-alone normal force coefficient. $\lambda = 0.0$	92
42	Comparison between predicted and experimental tail-alone normal force coefficient.	93
43	Comparison between predicted and experimental tail-alone normal force coefficient.	95
44	Comparison between predicted and experimental tail-alone normal force coefficient.	96
45	Comparison between predicted and experimental tail-alone normal force coefficient.	97
46	Tail-alone chordwise center of pressure at zero angle.	100

LIST OF ILLUSTRATIONS (CONTINUED)

<u>Figure</u>		<u>Page</u>
47(a)	Tail-alone chordwise center of pressure prediction curve. $AR = 0.5$	101
47(b)	Tail-alone chordwise center of pressure prediction curve. $AR = 1.0$	102
47(c)	Tail-alone chordwise center of pressure prediction curve. $AR = 2.0$	103
48	Comparison between predicted and experimental tail-alone chordwise center of pressure.	106
49	Comparison between predicted and experimental tail-alone chordwise center of pressure.	107
50	Comparison between predicted and experimental tail-alone chordwise center of pressure.	109
51	Oil flow photograph of tail/body junction.	112
52	Basic term for $C_{NB(T)}$.	115
53	Correction for effect of r/s .	117
54	Correction for effect of taper ratio.	118
55	Correction for effect of fin position.	119
56	Region of carryover loading.	121
57	Effect of fin span on R_o .	125
58	Effect of aspect ratio on R_o .	126
59	Effect of taper ratio on R_o .	127
60	Incremental effect of Reynolds number on R_o .	128
61	Effect of fin position on R_o .	129
62	Effect of fin span on $R_{T(B)}$ slope.	131
63	Effect of aspect ratio on R_1 .	132

LIST OF ILLUSTRATIONS (CONTINUED)

<u>Figure</u>		<u>Page</u>
64	Effect of taper ratio on R_1 .	133
65	Incremental effect of Reynolds number on R_1 .	134
66	Effect of fin position on R_1 .	135
67	Body-tail configuration N2C2B2T9 _M .	138
68	Tail normal-force amplification comparison.	139
69	Tail-alone chordwise center of pressure, base B1.	142
70	Correction to \bar{X}_T for determining $\bar{X}_{T(B)}$.	143
71	Comparison between predicted and experimental chordwise center of pressure of tail.	145
72	Spanwise center of pressure (ref. 23).	148
73	Comparison between predicted and experimental spanwise center of pressure of tail.	149
74(a)	Comparison between predicted and experimental spanwise center of pressure of tail.	150
74(b)	Comparison between predicted and experimental spanwise center of pressure of tail.	151
74(c)	Comparison between predicted and experimental spanwise center of pressure of tail.	152
75	Comparison between predicted and experimental total body-tail normal force coefficient.	163
76	Comparison between predicted and experimental total body-tail normal force coefficient.	164
77	Comparison between predicted and experimental total body-tail normal force coefficient.	165

LIST OF ILLUSTRATIONS (CONCLUDED)

<u>Figure</u>		<u>Page</u>
78	Comparison between predicted and experimental total body-tail normal force coefficient.	166
79	Comparison between predicted and experimental total body-tail pitching moment coefficient.	168
80	Comparison between predicted and experimental total body-tail pitching moment coefficient.	169
81	Comparison between predicted and experimental total body-tail pitching moment coefficient.	170
82	Comparison between predicted and experimental total body-tail pitching moment coefficient.	171

I. INTRODUCTION

A recurring problem in submersible vehicle design has been the lack of accurate methods for predicting configuration hydrodynamic characteristics.

Without accurate methods, submersible design is an uncertain process, requiring extensive testing and modification of models and full-scale vehicles before an acceptable configuration is defined. As a result, development times are lengthened and both time and cost schedules may be adversely affected. It cannot be said that the availability of accurate methods is a sufficient condition for removal of all obstacles to effective designs. However, it is certainly a necessary one.

The main obstacles to construction of such methods have been (a) the inability of classical hydrodynamic theory to handle viscous-flow situations and (b) the lack of suitable data to guide semi-empirical-method construction.

Classical theory has been proven quite reliable in cases where configuration flow fields are not significantly affected by viscous-flow phenomena, i.e., by boundary layers and wakes. For submersible vehicles, whose base regions produce thick or separated boundary layers and their associated wakes, and which deploy their control fins in precisely those viscosity-dominated regions, classical theory provides only a rough guide to performance. Of course, theoretical results may be supplemented and modified through reference to experimental data. However, if the data are unsystematic (as are those from specific vehicle designs) there is little chance of constructing methods having wide utility for broad classes of vehicles. What is required is a theoretical base, supplemented by systematic data and it is this approach which has been used in the present work.

Following an approach used successfully in missile aerodynamic design, Ref. 1, the work described here set out first to design, build and test a large number of models whose geometric parameters systematically covered the ranges typical of submersible designs. Data from these tests were

then used to supplement theoretical results in the construction of semi-empirical methods for predicting submersible hydrodynamic characteristics.

To facilitate data generation and instrumentation design, the tests were carried out in a wind tunnel, not in water. Following the wind tunnel tests, however, a limited investigation was made in a small water tunnel to determine whether test medium had an effect on the data. The results of these tests are given in a separate report.

The contents of this report are as follows: Descriptions are given of the models, tests, data generated and method construction. Each individual method is presented in self-contained form and includes: discussion of method construction, description of use, a numerical example, charts, graphs and tables, and a comparison between method predictions and experimental data. Discussions of configuration hydrodynamic behavior are given to supplement the methods descriptions.

II. MODELS

The models were designed to cover, systematically, those ranges of geometry typical of submersible vehicles, viz.,

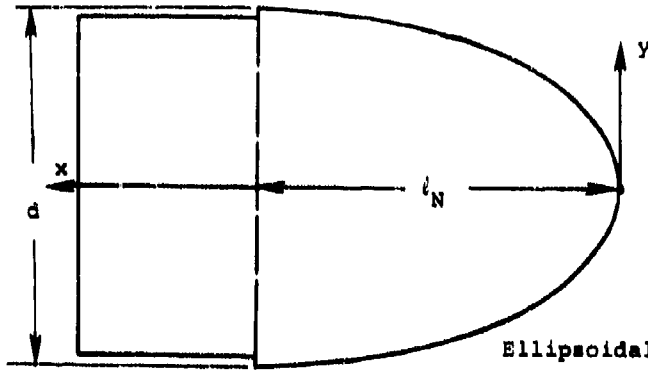
- Bodies having overall slenderness ratios varying from four to twelve.
- Noses having mainly ellipsoidal shapes, of varying length from 0.5 to 2.0 diameters.
- Bases of conical form (idealized shapes) having slenderness ratios from one to three.
- Tails of varying aspect ratio (0.5 to 2.0), taper ratio (0 to 1.0) and body diameter/exposed tailspan ratio (1.0 to 1.8).

More detailed descriptions of the models follows:

Model centerbody diameter was 7 inches. Nose shapes are as shown in figure 1. Three ellipsoidal noses are available having length/diameter ratios 0.5, 1.0 and 2.0, plus a torpedo-like nose having a profile of equation shown. The noses are designed to be readily interchangeable. Each can be fixed to the model centerbody.

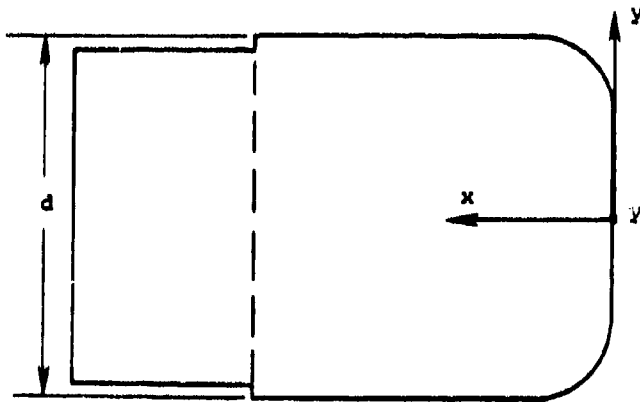
Model centerbody is composed of three separate sections as shown in figure 2. The section CA accommodates the main recording balance during test. Additional sections CB and CC can be deployed forward and aft of CA respectively. These center sections permit the cylindrical portion slenderness ratio to be varied from 2.5 to 7.0.

A typical model base is shown in figure 3. In all, three bases were built, lengths 1, 2 and 3 calibers. Each is of conical shape. The bases are made of aluminum and are machined to accommodate the three-component balances to which the tails are fixed. When no tails are required, the holes are filled by dummy plugs.



Nose	$\frac{l_N}{d}$
N1	0.5 (spherical)
N2	1.0
N3	2.0

Ellipsoidal noses, $\frac{(l_N - x)^2}{l_N^2} + \frac{y^2}{(\frac{d}{2})^2} = 1$

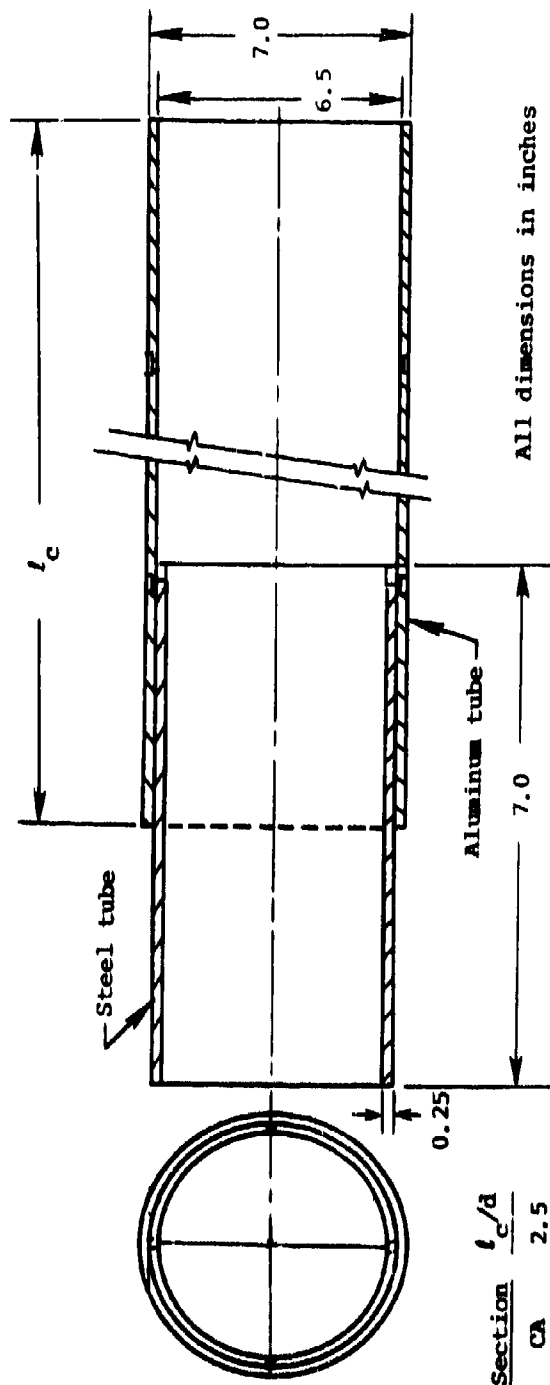


Torpedo nose, N4

$$y^3 = x^2(3x^2 - 8x + 6) - 4x(x-1)^3$$

$$l_N = d$$

FIGURE 1. NOSE SHAPES.



These center sections were combined into configurations as follow:

	l_c/d
C1 - CA alone	2.5
C2 - CA plus CB forward	4.0
C4 - CA plus CB forward plus CC aft	7.0

FIGURE 2. CENTER SECTIONS.

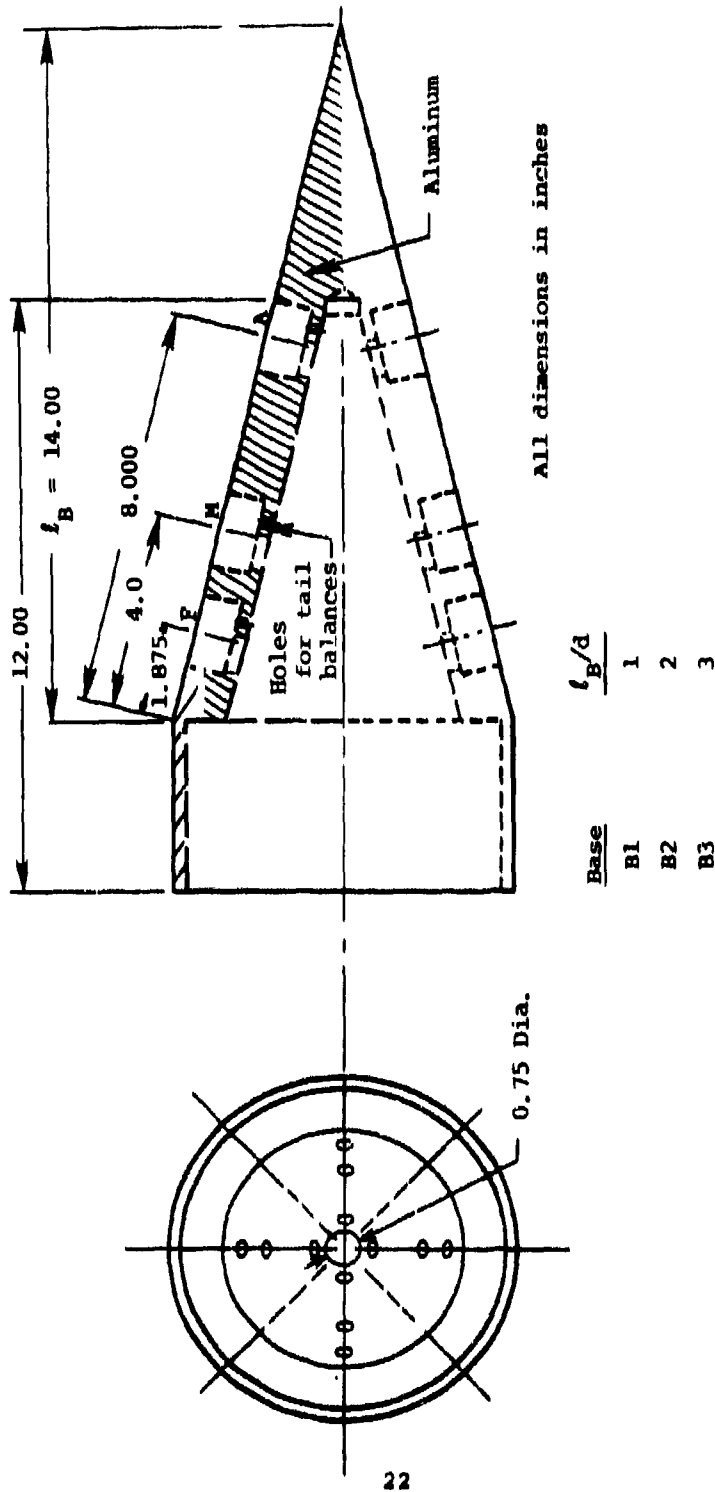
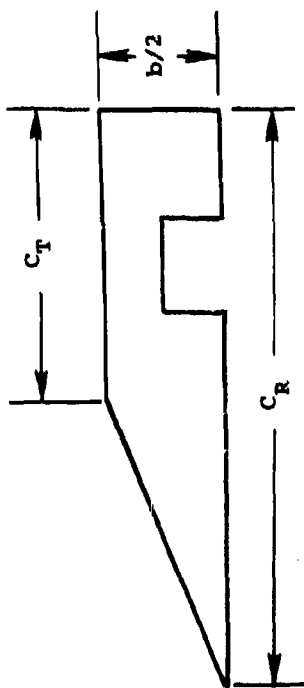


FIGURE 3. BASE B2.

Tail geometry and sizes are shown in figure 4. The tails are deployable on the bases and also on a reflection plane which is shown in figure 5. This plane permits testing of half-tails and yields results which are representative of complete, two-panel tails. The tails are mounted on three-component strain gauge balances which were specially-built for this program. These balances are shown in figure 6. They measure tail normal force, pitching moment and rolling moment. On the reflection plane, tail angle of attack is changed by rotating the plane. In the model, tail deflection is changed by means of index plates which mate to the balances. Each tail may be deflected to the angles 0, ± 10 , ± 20 , ± 30 degrees. During these initial tests, the tails were undeflected.

Photographs of various model pieces are shown in figures 7 through 10.



Tail No.	Taper Ratio	Aspect Ratio (2 Panels)	$b/2$ (In.)	Tip Chord C_T (In.)	Root Chord C_R (In.)	Single Panel Area (In. ²)
2	0.5	1.0	1.95	2.597	5.187	7.581
5	0.5	1.0	3.5	4.62	9.31	24.26
7	0	0.5	2.5	0	20.0	25.0
8	0	1.0	↑	0	10.0	12.5
9	0	2.0		0	5.0	6.25
10	0.5	0.5		6.664	13.328	25.0
11	0.5	1.0		3.332	6.664	12.5
12	0.5	2.0		1.666	3.332	6.25
13	1.0	0.5		10.0	10.0	25.0
14	1.0	1.0		5.0	5.0	12.5
15	1.0	2.0		2.5	2.625	6.563

FIGURE 4. TAIL GEOMETRY.

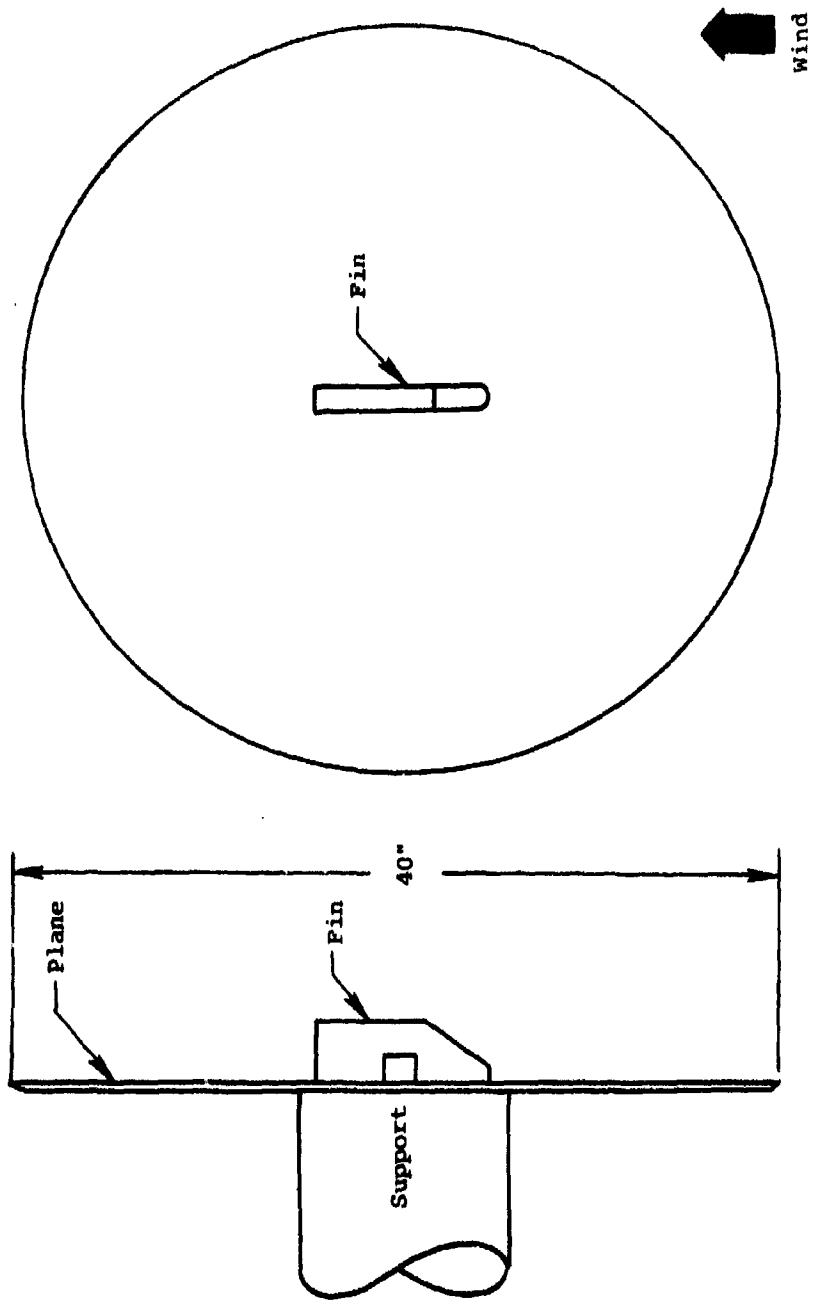
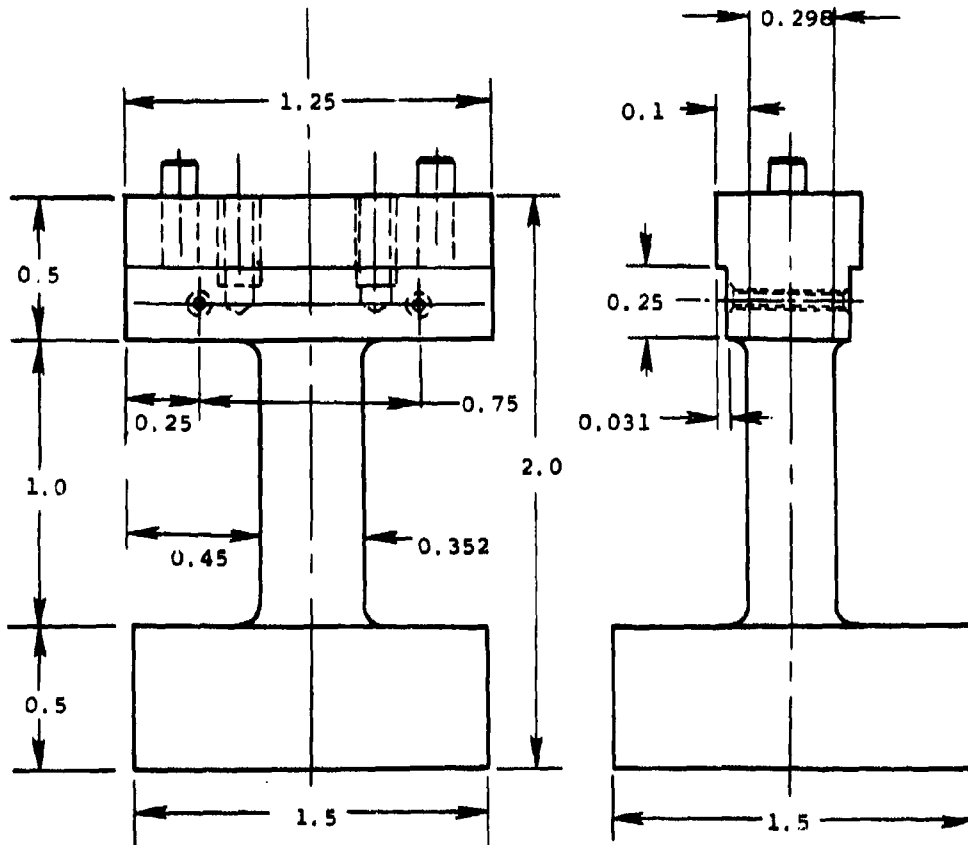


FIGURE 5. REFLECTION PLANE.



All dimensions in inches

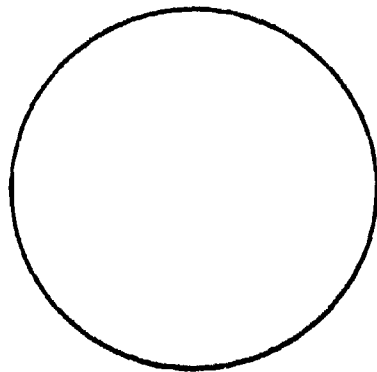


FIGURE 6. TAIL BALANCE.

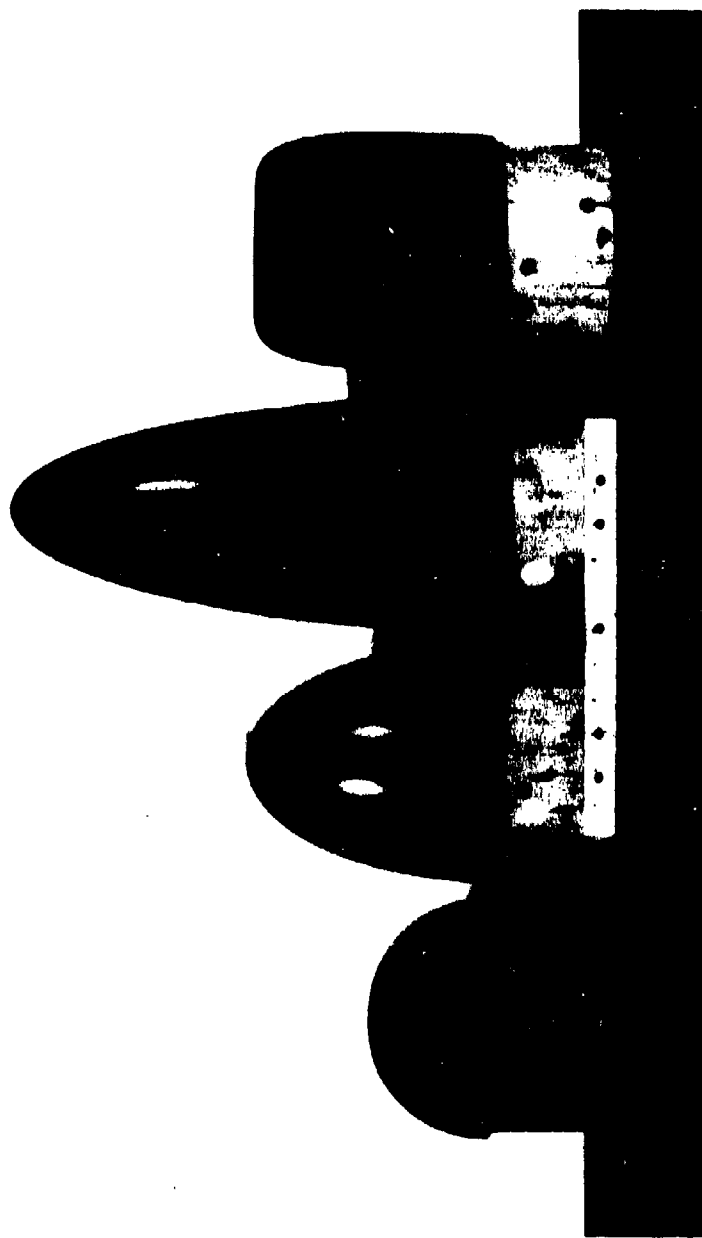


FIGURE 7. MODEL NOSES.

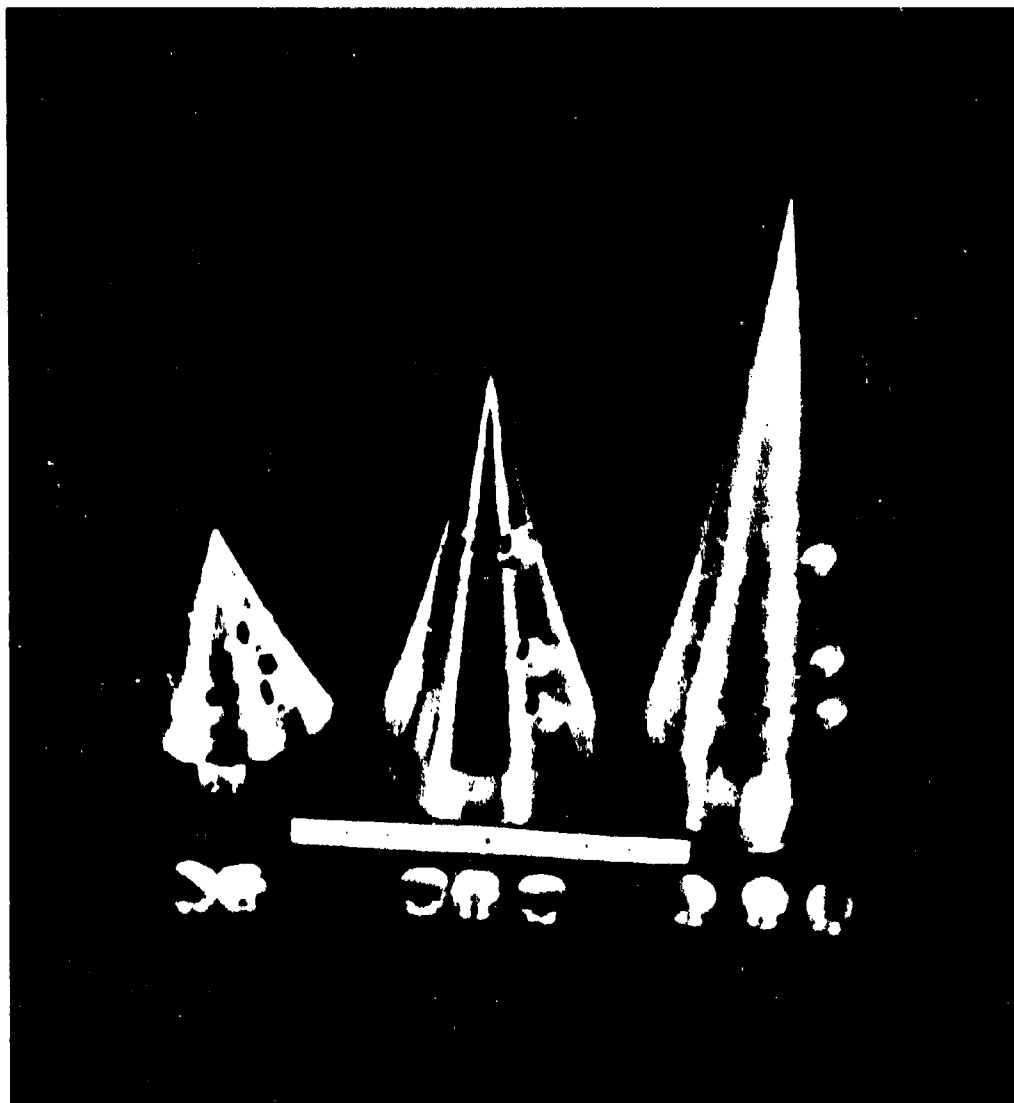


FIGURE 8. MODEL BASES.

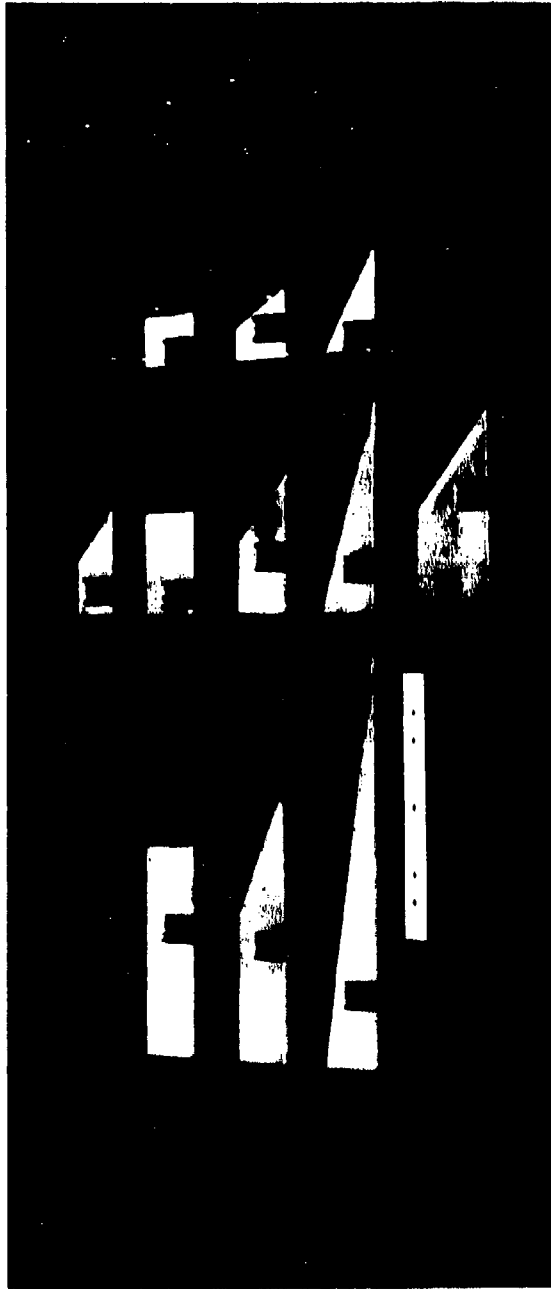


FIGURE 9. TAIL GEOMETRIES.

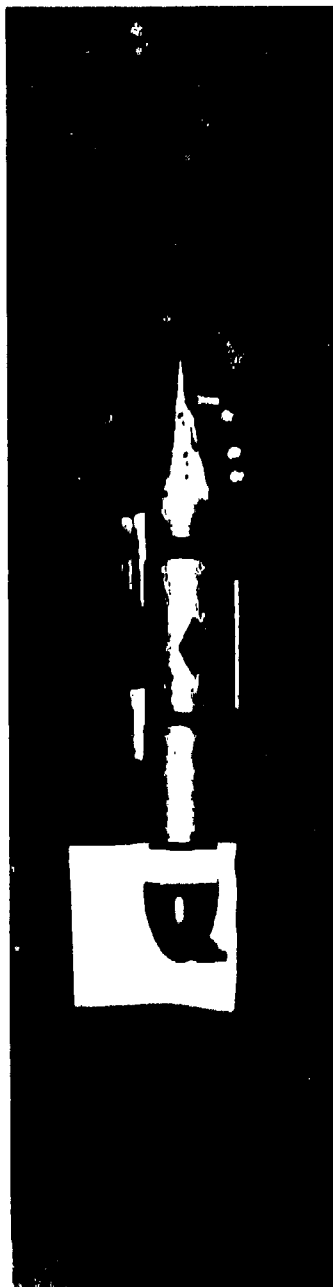


FIGURE 10. MODEL PIECES IN SEQUENCE.

III. WIND TUNNEL TESTS

The tests were conducted in the 12-Foot Pressure Wind Tunnel at NASA/Ames Research Center, Moffett Field, California. Wind tunnel testing was chosen for the following reasons.

- Theoretically there is no difference between dynamic characteristics in water and in air so long as the test Reynolds numbers are equal.
- Testing in air is far simpler than in water, particularly where electrical apparatus is involved.

A summary of the test configurations is given in Table 1. In general, each configuration was tested at the free stream Reynolds numbers, 4×10^5 and 8.5×10^5 per foot. Body and Body Tail configurations were mounted on a strut; tails were mounted on a reflection plane. Tail angles were varied from -3° to $+30^\circ$ on the reflection plane. On the body, the tails were undeflected. Body angle was varied from -3° to $+15^\circ$. Typical test configurations including the reflection plane, an isolated body and a body tail combination are shown in figures 11 through 13. Before proceeding to method construction, the data were corrected for zero shifts where necessary.

The data generated included:

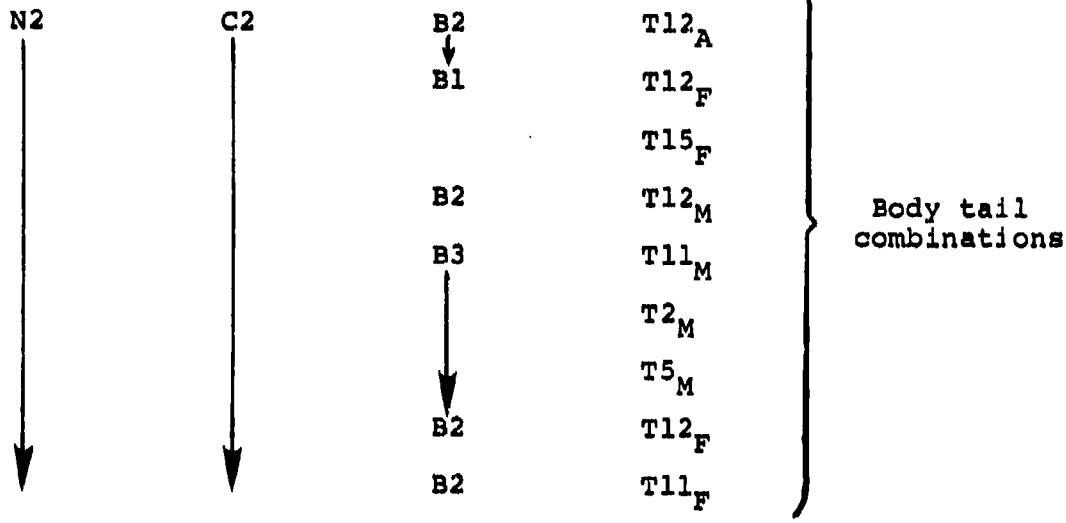
- Six-components of forces and moments from a Task balance located inside the body.
- Three-components of force and moment from each tail.

In addition, oil-flow visualizations were made of several configurations. Still photographs and videotape recordings were made.

TABLE I. CONFIGURATIONS TESTED

T11				}	Isolated tails
T14					
T8					
T9					
T13					
T15					
T12					
T10					
T7					
N2	C1	B2		}	Isolated bodies
N3	C2	B2			
N1	C2	B2			
N2	C2	B2			
N2	C2	B3			
N2	C4	B2			
N3	C4	B3			
N1	C1	B1			
N2	C2	B1			
N4	C2	B3			
N2	C2	B2	T11 _M		
↓	↓	↓	T5 _M		
			T14 _M		
			T2 _M		
			T9 _M		
			T13 _M		
		B1	T11 _A		
		↓	T2 _A		
		B2	T12 _A		
		↓	T10 _A		
			T8 _A		
			T11 _A		

TABLE I. CONCLUDED.



A - Aft tail location.
M - Mid tail location.
F - Forward tail location.



FIGURE 11. TAIL ON REFLECTION PLANE

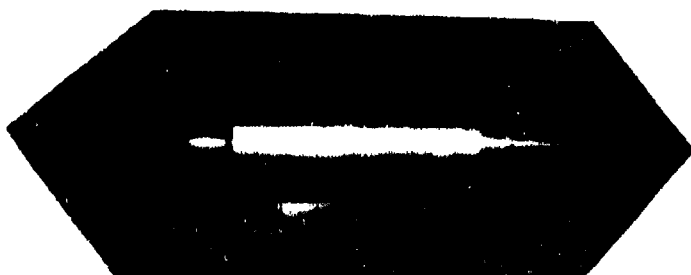


FIGURE 12. BODY ALONE MODEL N2C1B2



FIGURE 13. BODY TAIL MODEL N2C2B2T1_A

IV. FORMULATIONS

Following the practice widespread in aerospace work, the hydrodynamic characteristics of complete configurations were formulated by considering first the characteristics of isolated components (bodies, tails) and then combining these, accounting for their mutual interactions.

From the reflection plane tests, the following quantities are obtained.

- C_{N_T} Isolated tail normal-force coefficient
- \bar{X}_T Isolated tail chordwise center of pressure

Isolated body tests yielded

- C_{N_B} Body normal-force coefficient
- C_{M_B} Body pitching-moment coefficient
- C_{A_B} Body axial-force coefficient

For body/tail configurations, more complex quantities are obtained, as described in the following.

The various quantities associated with the hydrodynamic pitching behavior of a cruciform submersible are written below. The horizontal tail half-panels are treated as though they had arbitrary deflection δ at body pitch angle α . (During the tests δ was kept equal to zero). The deflection δ is assumed positive leading-edge-up relative to the tail neutral position. The body is assumed fixed in roll altitude and the vertical tails are undeflected, thus generating no force.

$$C_{1_{BT}} = \sum_{i=1}^2 C_{N_T} R_{T(B)_i} \cos \delta_i \frac{V_{T(B)_i}}{d} \frac{S_T}{S_R} \quad (1)$$

Here, $R_{T(B)_i}$ and $\bar{Y}_{T(B)_i}$ are the normal-force amplification and center of pressure location on the i^{th} horizontal tail panel.

$$R_{T(B)_i} = \frac{C_{N_{T(B)_i}}}{C_{N_T}} \quad (2)$$

This is analogous to the $K_{T(B)}$ factor of reference 2. Hence, $R_{T(B)_i}$ and $\bar{Y}_{T(B)_i}$ are functions of α , δ_i , and geometry.

With these quantities available, it is possible to write the axial-force coefficient as

$$C_{A_{BT}} = \sum_{i=1}^2 \left[C_{N_T} R_{T(B)_i} \right] \sin \delta_i + C_{A_B} \quad (3)$$

Note that the effects of tail leading-edge suction have been ignored. For these tails they are negligible.

The other configuration coefficients are:

$$C_{N_{BT}} = C_{N_B} + \sum_{i=1}^2 \left[C_{N_T} R_{T(B)_i} \right] \cos \delta_i \frac{S_T}{S_R} + C_{N_{B(T)}} \quad (4)$$

$$C_{M_{BT}} = C_{M_B} + \sum_{i=1}^2 \left[C_{N_T} R_{T(B)_i} \right] \frac{\bar{X}_{T(B)_i}}{d} \cos \delta_i \frac{S_T}{S_R} + C_{N_{B(T)}} \frac{\bar{X}_N}{d} \quad (5)$$

where $C_{N_{B(T)}}$ is the carryover body normal force (related to $K_{B(T)}$ of ref. 2) and \bar{X}_N is its center of pressure. The value $\bar{X}_{T(B)_i}$ is the chordwise center of pressure location of the i^{th} horizontal tail.

To summarize then, the methods to be constructed deal with the following quantities.

C_{A_B}	body axial-force coefficient
C_{N_B}	body normal-force coefficient
C_{N_T}	tail-alone normal-force coefficient
$C_{N_{B(T)}}$	carryover loading on body due to presence of the horizontal tails
$R_{T(B)_i}$	amplification of tail-alone normal force in presence of the body
\bar{X}_N	center of pressure of $C_{N_{B(T)}}$
$\bar{X}_{T(B)_i}$	chordwise center of pressure of tail on body
$\bar{Y}_{T(B)_i}$	spanwise center of pressure of tail on body
C_{M_B}	body pitching-moment coefficient
\bar{X}_T	chordwise center of pressure of tail

Methods were constructed for all these quantities. Each method contains a background discussion, a description of method construction, directions for use, numerical example, comparison with independent data, references, charts, graphs and tables.

(Reverse Page 38 Blank)

V. ISOLATED BODIES

V.1 GENERAL CONSIDERATIONS

When a slender, cylindrical body is placed at an angle of attack α in an air stream of velocity V_∞ , the flow may be considered as consisting of two components. One component is parallel to the body axis and is termed axial flow $V_\infty \cos \alpha$. The other component is normal to the body axis and is the crossflow, $V_\infty \sin \alpha$. At angles of attack greater than about 6° , the boundary layers associated with the crossflow separate on either side of the body and form a lee-side wake as depicted in figure 14 taken from reference 3. This wake takes the form of a pair of symmetrically disposed, counter-rotating vortices and is fed by vorticity shed from the separating boundary layer. Initially, the separated region is quite small and is located near the rear of the body. Eventually, however, the separation region extends over virtually the entire body as angle increases. At angles of attack greater than about 25° an asymmetric vortex flow pattern may appear. This report does not consider the latter type of flow pattern.

The loads on a cylindrical body at angle of attack are usually described in terms of a normal force, an axial force, and a pitching moment. In general, all three quantities are linear with angle of attack for small angles. At larger angles, however, these quantities demonstrate nonlinear behavior, due to the separated crossflow discussed in the previous paragraph. The axial force shows relatively little variation with angle of attack up to at least 15° but the normal force and pitching moment can show quite large variations, depending upon the particular configuration. Past studies (e.g., ref. 4) have been quite successful in applying potential flow theory to predict the linear behavior of these quantities and a crossflow drag analogy to predict the nonlinear behavior. According to this latter concept, each section along the body experiences a cross force equal to the drag force the section would experience with the axis of revolution normal to a stream moving at a velocity $V_\infty \sin \alpha$ (ref. 4).

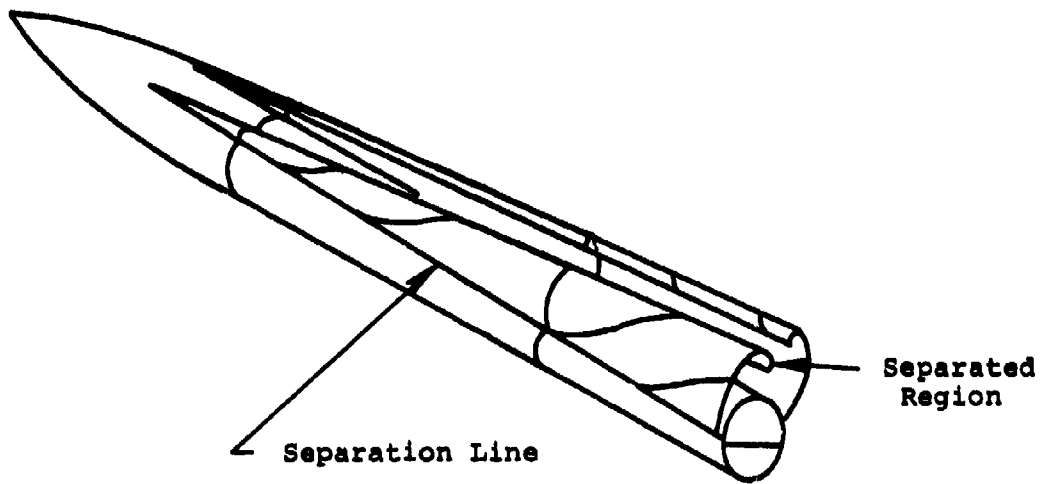


FIGURE 14. SYMMETRIC VORTEX WAKE (FROM REF. 3).

The use of potential flow theory in the prediction of the transverse force on a body of revolution is well established, having been initiated by Munk in connection with his work on airships (ref. 5). Munk showed that the cross force per unit length can be expressed as

$$f = q \frac{dS}{dx} \sin 2\alpha \quad (6)$$

Thus, applied to bodies that are closed at the base, as in the present test, potential flow theory yields a zero net force, but a nonzero pitching moment. This means that the load on such a body is in the form of a pure couple. The center of pressure of such a load is at upstream infinity. This result is true only for angles of attack near zero. In reality, the boundary layer along the body separates somewhere upstream of the end of the body. The location of this separation point, x_{sa} , can thus be used to determine the amount of potential lift on the body. The essential linearity of the transverse force with α at small angles shown by equation (6) is borne out by experiment. Hence, at small angles of attack, the normal force on an isolated body is due to potential lift which extends back to the location x_{sa} .

At higher angles of attack the crossflow-drag analogy is used to explain the nonlinear viscous crossflow effects on the loads. The crossflow normal force has the form

$$C_{N_{nl}} = n C_{d_c} \frac{S_p}{S_R} \sin^2 \alpha \quad (7)$$

It is important to note two points associated with the viscous crossflow. First, the crossflow does not begin to separate at the nose but at some downstream position x_{sc} which is a function of the angle of attack. Second, vortex size and strength, in general, increase toward the rear of the body. Thus, the proper distribution of crossflow force, expressed in the term $C_{d_c}(x)$ is necessary to properly

account for the nonlinear pitching moment.

In the following sections these concepts will be utilized to aid in developing methods for the calculation of body-alone normal-force coefficient, axial-force coefficient, and pitching-moment coefficient.

The results of the flow visualization investigation of the isolated bodies brought out an interesting feature of the flow over the one caliber base. Figures 15 and 16 are oil flow photos of the one caliber base and reveal the presence of two concentrated symmetric vortices located beneath the base. The presence of this vortex structure can entirely dominate the hydrodynamic characteristics of bodies with this size base. Even at low angles of attack this highly viscous region means that linear potential flow theories do not provide accurate load estimates. The locations for the horizontal fins are seen clearly in Figure 15 and the direction of the flow at that location means the fins will be in a region of separated flow, greatly reducing their effectiveness. This is discussed in more detail in Section VII.1. When applying the various methods to bodies with a one caliber base, the presence of this wake structure should be borne in mind. A similar investigation of longer bases did not reveal the presence of any concentrated vortex structure - the flow was smooth and attached out to the end of the base.

V.2 BODY-ALONE NORMAL-FORCE COEFFICIENT

This method permits calculation of the normal-force coefficient on isolated bodies in incompressible flow for angles of attack up to 15° . The method consists of two steps. The first determines the normal-force-curve slope from the effective base and potential flow theory. The second calculates the nonlinear viscous force. Comparisons between the method and experimental data show good agreement.

The normal force on an isolated slender body of revolution at angle of attack is made up of contributions due to potential lift and viscous crossflow effects. At small angles of attack the normal force is well-approximated by potential flow theory and is essentially linear with angle of attack. When the body exceeds an angle of attack of about 6° a lee-side vortex wake forms and the normal force becomes nonlinear. Past work has shown (e.g., ref. 4) that the total normal force can be quite successfully described by a combination of potential flow theory (to describe the linear behavior) and a second nonlinear term derived from the cross-flow-drag analogy described in the previous section. Hence, the normal-force coefficient is assumed to be of the form

$$C_{N_B} = a_1\alpha + a_2\alpha^2 \quad (8)$$



FIGURE 15. OIL FLOW PHOTOGRAPH OF BASE B1



FIGURE 16. OIL FLOW PHOTOGRAPH OF BASE B1.

The following boundary condition has been applied:

$$C_{NB} (\alpha = 0) = 0 \quad (9)$$

Therefore, taking the derivative of equation (8), the result is derived that a_1 is equal to the zero angle normal-force-curve slope, i.e.,

$$a_1 = \left(\frac{dC_{NB}}{d\alpha} \right)_0 \quad (10)$$

The coefficient a_2 is the value given by determining the crossflow drag of the particular body.

Description of Method

Potential Force. For a body not closed at the rear, the normal force can be expressed as (Ref. 6)

$$NF = q \frac{\pi}{4} d_b^2 \sin 2\alpha \approx 2q\alpha S_b^2 \quad (11)$$

where S_b and d_b are the cross-sectional area and diameter respectively of the base. In this relation the normal-force coefficient becomes

$$C_{N_{pot}} = 2 \frac{S_b}{S_R} \alpha \quad (12)$$

where S_R is the maximum cross-sectional area of the body. Stated in terms of the normal-force-curve slope, potential flow theory thus gives

$$C_{N_\alpha} = 2 \frac{S_b}{S_R} = 2 \left(\frac{d_b}{d} \right)^2 \quad (13)$$

In the configurations used in the present test the body is closed at the base. This implies that d_b and hence C_{N_α} are zero. However, the experimental values of C_{N_α} are non-zero and equation (13) can be used to determine the diameter of the "effective base" caused by boundary layer separation or thickening. Then, from the body surface coordinates, the location of axial-flow separation can be

determined. This result is useful when tail fins are placed in this region as it will be possible to estimate how much of the fin is immersed in separated flow and how much is immersed in the external potential flow.

Examination of the data from the present test revealed that the normal-force-curve slope was a function of the base length (or equivalently ds/dx of the base) and of the forebody slenderness ratio (that portion of the body ahead of the conical base section). Correlation curves were prepared from the experimental values of $C_{N\alpha}$, along with equation (13),

to determine the location of x_{sa} , the position of boundary-layer separation of the axial flow. These curves are given in figure 17. The distance x_{sa} is measured from the start of the conical base section. Hopkins, in a previous study (ref. 7) was able to correlate x_{sa} measured from the nose with the distance from the nose to the point at which ds/dx has a maximum negative value (x_1). This is essentially similar to the curves in figure 17. All the bodies used in Hopkins' study had smooth and continuous variations in the cross-sectional area. In the bodies examined in the present experimental study, the location of the maximum negative value of ds/dx always occurs at the start of the base section. Thus, l_F/d , the forebody slenderness ratio, corresponds to x_1 in Hopkins' work. However, since models of the present design can result in relatively long forebodies and relatively short bases with steep variation in local diameter, a small error in location of x_{sa} could result in a large error in d_b if x_{sa} was measured from the nose. Hence, much more accurate results are obtained in the present case by measuring x_{sa} from the beginning of the base section. Once x_{sa} , and thereby d_b , is determined from the figure, the potential force can be calculated from equation (12).

Viscous Crossflow Force. Crossflow separation usually begins at the base of the body when an angle of attack of approximately 6° is reached. With increasing angle of attack, the location of this crossflow separation occurs further upstream, so that eventually most of the body is in separated crossflow. A previous correlation of available data (ref. 8) has shown that the location of the beginning of crossflow separation can be expressed as

$$\frac{x_{sc}}{d} = 1 + \frac{5}{\alpha - 4} \quad (14)$$

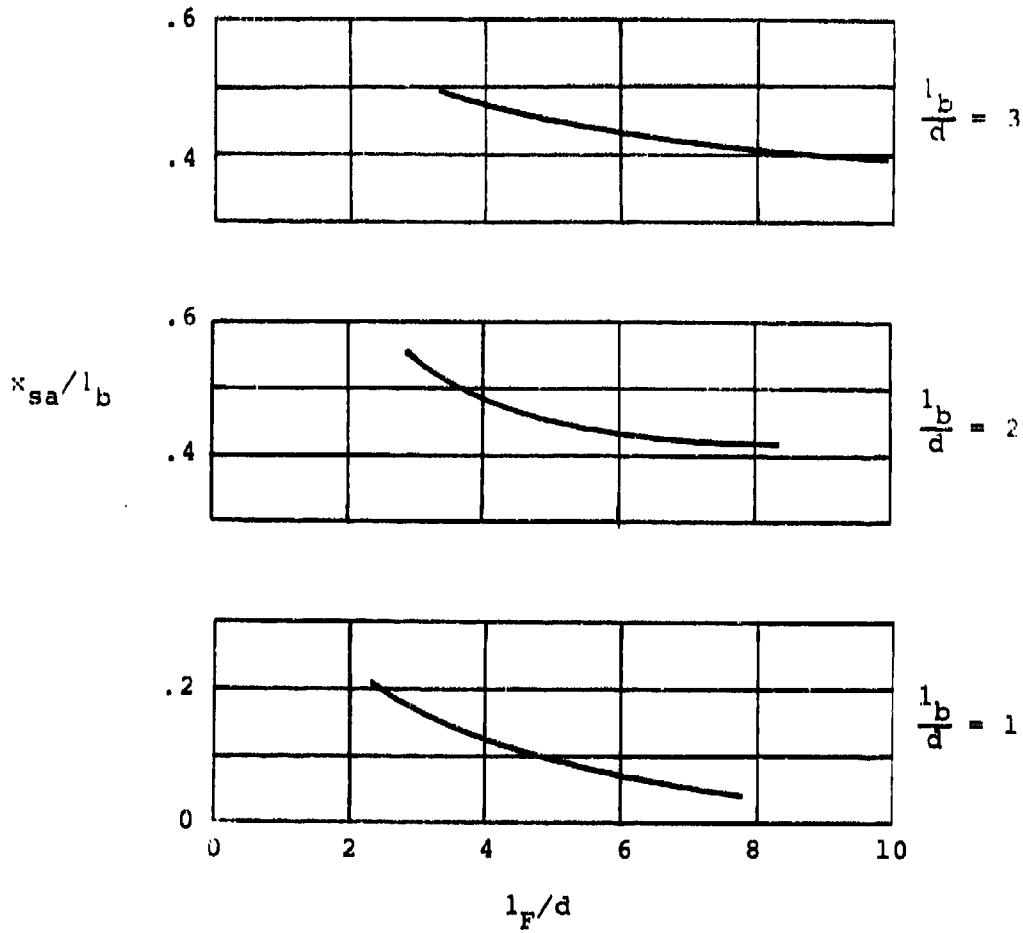


FIGURE 17. POSITION OF AXIAL FLOW SEPARATION BASED ON NORMAL FORCE CURVE SLOPE.

The value of the viscous force term can be written as

$$C_{N_{nl}} = C_{d_c} \frac{S_{pc}}{S_R} \sin^2 \alpha \quad (15)$$

where S_{pc} is the planform area of that portion of the body in separated crossflow. The crossflow-drag coefficient is a function of the local crossflow Reynolds number. Therefore, for sections of changing diameter a different value for C_{d_c} is required for every section. Values of C_{d_c} are obtained from figure 18, taken from reference 9. These values of C_{d_c} are average values over the entire separated region. This is all that is necessary for the computation of normal force. However, when computing pitching moment, the axial distribution of crossflow drag is required. This point is discussed in more detail in the next section.

This method for calculating the viscous crossflow force is contained in equations (14) and (15) plus figure 18. It is a well-established and documented procedure which has been adapted to bodies of the present type.

A description of method use will now be given, followed by a numerical example.

Use of Method

The parameters required to determine the body-alone normal-force coefficient are

Slenderness ratio of forebody, l_F/d

Local body radius distribution, $r(x)$

The procedure to be followed is:

- (1) Given the base and l_F/d , determine x_{sa} from figure 17.
- (2) From x_{sa} , determine d_b , the diameter of the base at x_{sa} . This is the effective base of the body.

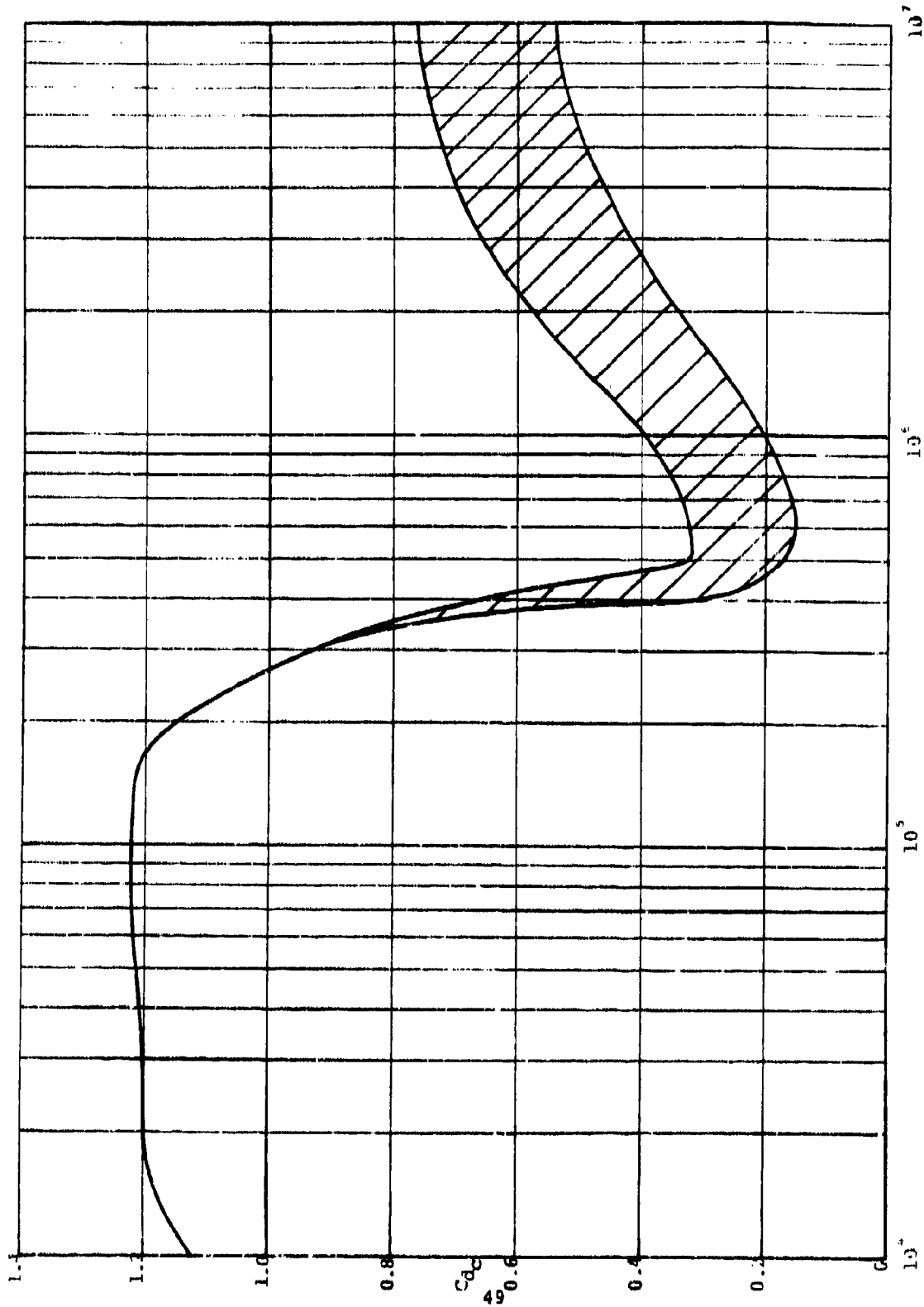


FIGURE 18. VARIATION OF CROSSFLOW DRAG COEFFICIENT WITH CROSSFLOW REYNOLDS NUMBER FOR CIRCULAR CYLINDERS (REF. 2).

- (3) Use d_b in equation (13) to calculate C_{N_α} .
- (4) Find $C_{N_{pot}}$ from equation (12).
- (5) For each angle of attack at which the value of C_{N_B} is required, determine x_{sc} from equation (14).
- (6) Knowing the location of crossflow separation, determine S_{pc} .
- (7) Determine C_{d_c} from figure 18 for each local section behind x_{HC} .
- (8) Calculate $C_{N_{n1}}$ from equation (15).
- (9) Add the results from steps (4) and (8) to determine total C_{N_B} .

Numerical Example. This example compares the method to data from the present test. The configuration chosen is N2C2B2, at a free stream Reynolds number of 35×10^6 . The values of the required parameters are

Forebody slenderness ratio: $l_F/d = 5$

Nose section: One caliber ellipsoid

Base section: Two caliber circular cone

Body diameter: 7.0 in.

A sketch of this configuration is given in figure 19.

- (1) From figure 17, $x_{sa}/l_b = 0.455$.
- (2) The equation for the diameter of a cone two calibers in length is

$$d_x = d(1 - \frac{x}{d})$$

where d is the diameter of the base of the cone. Thus $d_b = 3.815$ in. and $d_b/d = 0.545$.

- (3) From equation (13), $C_{N_\alpha} = 0.594$ per radian.



FIGURE 19. BODY CONFIGURATION N2C2B2

- (4) Use $C_{N_{pot}} = C_{N_{\alpha}} \alpha$ to find potential force as a function of angle of attack.
- (5) Determine x_{sc} from equation (14) for each angle of attack required.
- (6) Calculate planform area from each x_{sc} in step (5) to end of body.
- (7) Find the appropriate value of C_{d_c} for each local section at each crossflow Reynolds number.

In the present example $C_{d_c} = 0.290$ throughout.

- (8) Use equation (15) to find $C_{N_{nl}}$.
- (9) Add result from step (4) to result from step (8) to find C_{N_B} .

Steps (4) through (9) are summarized in the table below.

α	Step (4) $C_{N_{pot}}$	Step (5) x_{sc}/d	Step (6) $S_{pc} (ft^2)$	Step (7) C_{d_c}	Step (8) $C_{N_{nl}}$	Step (9) C_{N_B}
2	0.0207	-	-	-	-	0.0207
4	0.0414	-	-	-	-	0.0414
6	0.0621	3.500	0.8897	0.290	0.0106	0.0727
8	0.0827	2.250	1.3537	0.290	0.0285	0.1112
10	0.1031	1.833	1.5250	0.290	0.0499	0.1530
12	0.1235	1.625	1.6234	0.290	0.0762	0.1997
14	0.1437	1.500	1.6924	0.290	0.1075	0.2512
16	0.1637	1.417	1.7466	0.290	0.1440	0.3077

This is compared to the experiment in figure 20. The agreement is quite good throughout the angle of attack range. Further comparisons between estimates and data are shown in figures 21 and 22.

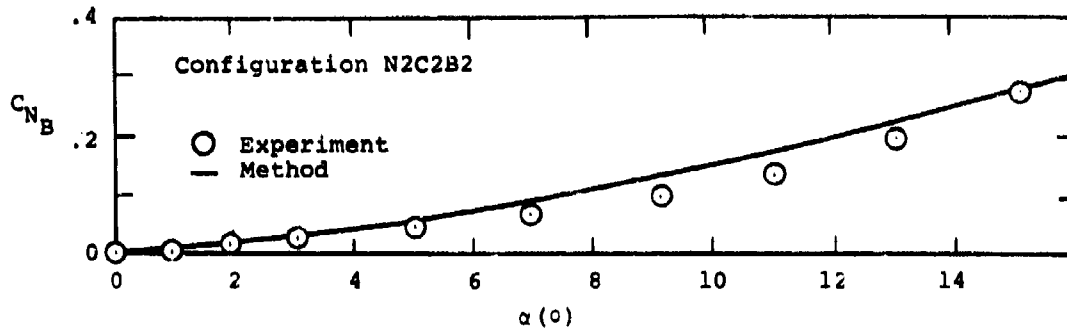


FIGURE 20. COMPARISON BETWEEN PREDICTED AND EXPERIMENTAL BODY-ALONE NORMAL FORCE COEFFICIENT.

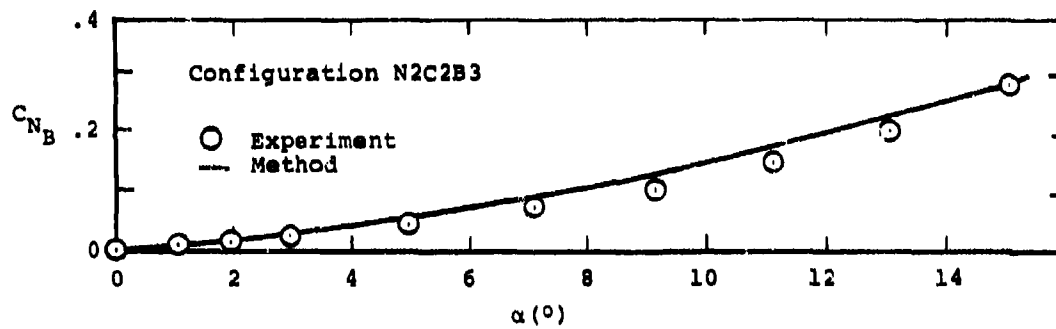


FIGURE 21. COMPARISON BETWEEN PREDICTED AND EXPERIMENTAL BODY-ALONE NORMAL FORCE COEFFICIENT.

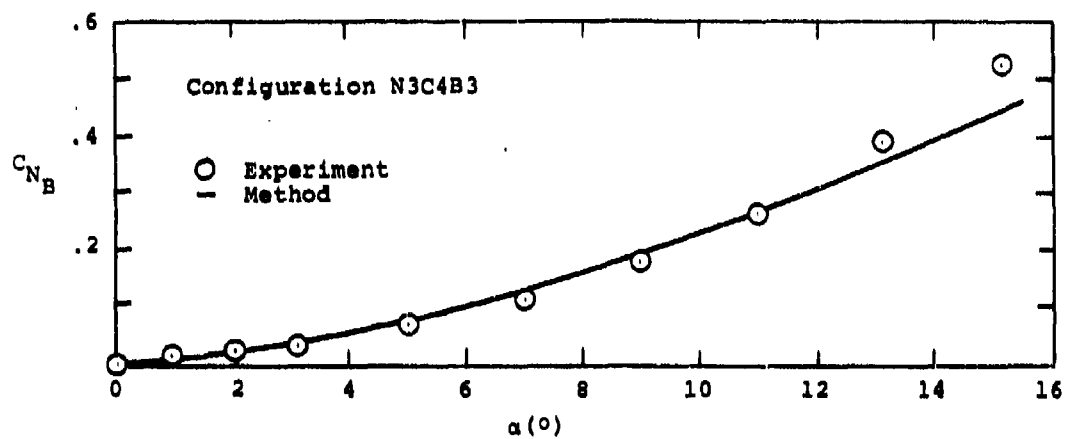


FIGURE 22. COMPARISON BETWEEN PREDICTED AND EXPERIMENTAL BODY-ALONE NORMAL FORCE COEFFICIENT.

V.3 BODY-ALONE PITCHING-MOMENT COEFFICIENT

This method permits estimation of the pitching-moment coefficient on isolated bodies at angles of attack up to 15° . The method consists of a linear term derived from potential-flow theory and a nonlinear term which is the contribution from viscous crossflow. Included in the nonlinear term is an estimation of the axial distribution of the cross-flow normal force. Comparison with data from the present experiment shows reasonable agreement for both terms.

An adequate estimation of the pitching moment on a slender body of revolution has been, in the past, a very elusive objective. It requires not only a suitable estimate of the normal force, but also a knowledge of the axial distribution of that normal force. As developed in the previous section, the normal force consists of a linear term due to potential lift and a nonlinear viscous term. Thus, the distribution of two forces are actually required. However, in addition this means that the pitching moment also can be treated as the sum of a linear term (potential flow) and a nonlinear term (viscous flow). Thus, the objective of this section is to develop an expression for pitching-moment coefficient of the form

$$C_{M_B} = a_1 \alpha + a_2 \alpha^2 \quad (16)$$

Applying slender body theory, Allen and Perkins (ref. 4) found the following expression for the pitching moment;

$$C_{M_B} = \frac{1}{S_R d} \int_0^{l_B} \frac{dS}{dx} (x - x_m) dx \left(\sin 2\alpha \cos \frac{\alpha}{2} \right) \quad (17)$$

$$= \frac{V_B - S_b (l_B - x_m)}{S_R d} \sin 2\alpha \cos \frac{\alpha}{2} \quad (18)$$

This analysis, applied to bodies that are closed at the base ($S_b = 0$), as were those here, yields the result that the pitching moment is only a function of the size (i.e., volume) of the body. But, as discussed in the previous section on normal-force coefficient, there is an effective base due to the separation or thickening of the axial-flow boundary layer. The axial location of the effective base, x_{sa} , marks the downstream extent of the potential flow.

Thus, it seems more realistic to use this position, rather than the end of the body, as the upper limit of integration in equation (17).

The usual practice of estimating the contribution to the pitching moment due to viscous crossflow (e.g., see ref. 7 or 10) is to assume a relation of the form

$$C_{M_{nl}} \approx \frac{2n\alpha^2}{S R^d} \int_{x_{sc}}^{x_B} C_{d_c} r(x_m - x) dx \quad (19)$$

In this expression C_{d_c} assumes the value corresponding to the local crossflow Reynolds number. For a cylindrical body then, C_{d_c} is usually assumed constant with x and equation (19) gives a viscous force distribution that is uniform in x . The result of this assumption usually is that the nonlinear pitching moment is under-predicted (ref. 7). For this reason a brief analysis of the expected form of the viscous force axial distribution is helpful.

If the separated crossflow boundary layer is represented by a set of point vortices, then the vortex impulse theorem for moderate angles of attack gives the following expression for the loading on an infinitesimal length of the body in the presence of vortices (ref. 11)

$$dN = \text{Real} \sum_{j=1}^{N_v} d(\Gamma \sigma)_j \quad (20)$$

where Γ is the vortex strength, σ is the complex distance between a vortex and its image inside the cylinder, and N_v is the number of vortices. For moderate angles of attack the lee-side vortex wake normally can be represented by two vortices which reduces equation (20) to

$$dN = d(\Gamma b_v) = b_v d\Gamma + \Gamma db_v \quad (21)$$

where b_v is the distance between the vortices or the span of the vortex wake. Thus, the axial distribution of the vortex-induced force becomes

$$\frac{dN}{dx} = b_v \frac{d\Gamma}{dx} + \Gamma \frac{db_v}{dx} \quad (22)$$

Measurements of both b_v and Γ have been correlated in reference 8 by Mendenhall and Nielsen, who show that, to a first approximation, both terms are linear in x . These results are reproduced in figures 23 and 24.

Since db_v/dx is small it can be ignored in equation (22) so that

$$\frac{dN}{dx} = \frac{d\Gamma}{dx}$$

And, since $\Gamma = x$, then the normal force will be distributed in an approximately linear fashion along the body. Therefore, for purposes of estimating the pitching moment due to the viscous normal force, the crossflow-drag coefficient can be represented by the relation

$$C_{d_c}(x) = \left(\frac{2x}{x_B - x_{sc}} \right) C_{d_c} \quad (23)$$

This relation distributes the crossflow-drag force linearly from the position of crossflow separation x_{sc} to the end of the body. The crossflow-drag coefficient, C_{d_c} , is the value based on local crossflow Reynolds number and is given in figure 18.

Description of Method

Pitching-Moment-Curve Slope. The present method involves an equation of the form given in equation (16) and repeated here for convenience.

$$C_{M_B} = a_1 \alpha + a_2 \alpha^2$$

The one boundary condition available is

$$C_{M_B}(\alpha = 0) = 0 \quad (24)$$

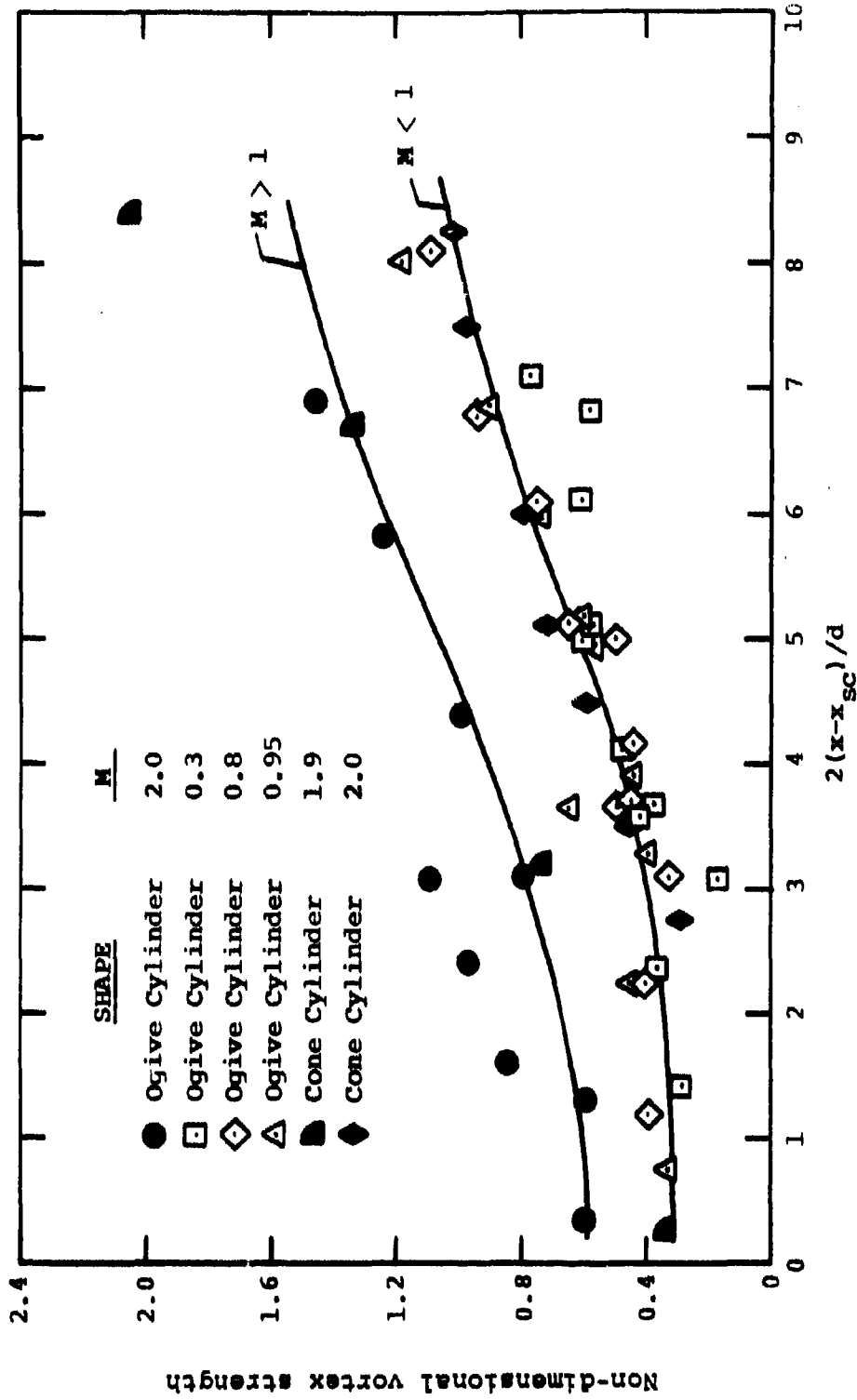


FIGURE 23. BODY-VORTEX CHARACTERISTICS - VORTEX STRENGTH (REF. 8).

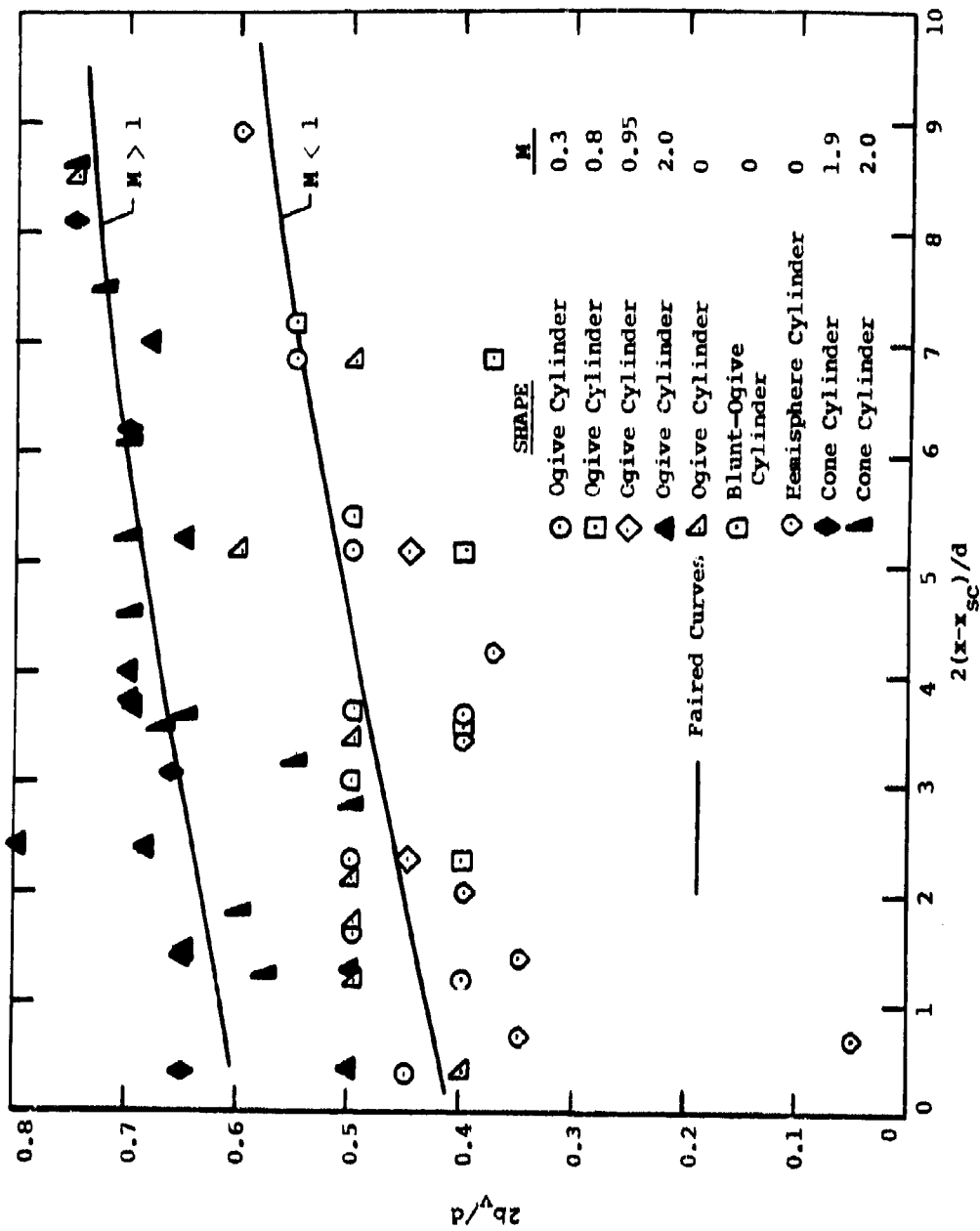


FIGURE 24. BODY-VORTEX CHARACTERISTICS - HORIZONTAL VORTEX POSITION (REF. 8).

Differentiating equation (16) with respect to x yields the result that

$$a_1 = \left(\frac{dC_{M_B}}{d\alpha} \right)_0 = C_{M_\alpha} \quad (25)$$

i.e., a_1 is the pitching-moment-curve slope. In the present method, the following expression is used to estimate C_{M_α} .

$$C_{M_\alpha} = 2 \frac{K_m (K_2 - K_1)}{S_R d} \int_0^{x_{sa}} \frac{dS}{dx} (x_m - x) dx \quad (26)$$

The term $(K_2 - K_1)$ is the apparent mass factor of Munk (ref. 5) for ellipsoid-shape bodies and is given in figure 25. The term K_m is an empirical factor derived from the data and applied^m to the apparent mass term. This term is shown in figure 26. The upper limit of integration is the axial location of the effective base. This quantity, along with a more complete discussion of the procedure used to obtain its value can be found in Section V.2.

Nonlinear Pitching Moment. It is assumed that the viscous crossflow exerts a force on the body from x_{sc} , the axial location of crossflow separation, to the end of the body, and that, along this length, the viscous force varies linearly with x . With these assumptions the following term represents the pitching moment due to viscous crossflow.

$$C_{M_{n1}} = \frac{4\eta\alpha^2}{S_R d} \left(\frac{l_B}{x_B - x_{sc}} \right) \int_{x_{sc}}^{x_B} C_{d_c} r(x) (x_m - x) dx \quad (27)$$

The crossflow drag coefficient is the value corresponding to the local crossflow Reynolds number at each section of the body between x_{sc} and x_B . Curves for C_{d_c} are given in

figure 18. The term η is the ratio of the drag on a finite cylinder to the drag on an infinite cylinder and is applied as a correction factor for finite length. Values for η are obtained from data given by Goldstein in reference 12 and are presented in figure 27. The lower limit of

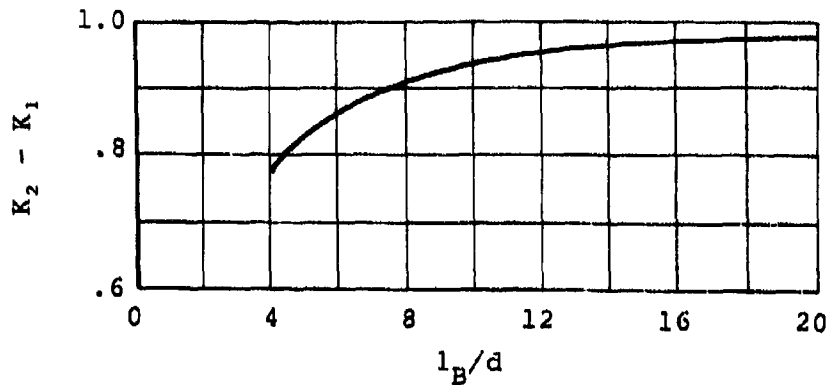


FIGURE 25. APPARENT MASS FACTOR (FROM REF. 5).

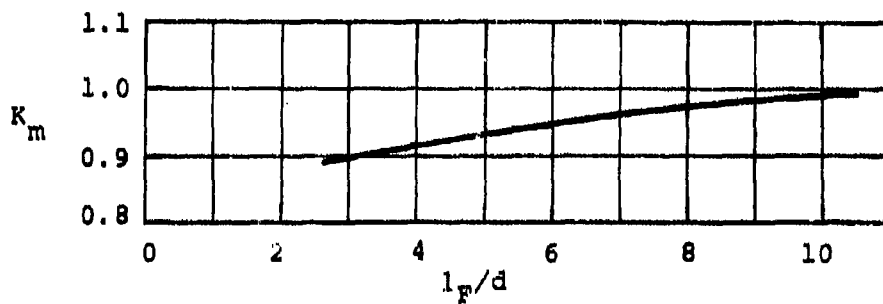


FIGURE 26. EMPIRICAL FACTOR USED IN PITCHING-MOMENT-CURVE SLOPE.

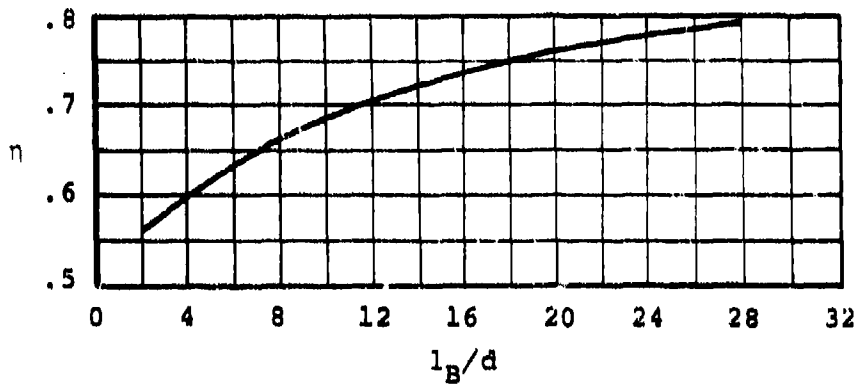


FIGURE 27. RATIO OF CROSSFLOW-DRAG COEFFICIENT FOR A FINITE LENGTH CYLINDER TO THAT FOR AN INFINITE LENGTH CYLINDER (FROM REF. 12).

integration, x_{sc} , is given by the following expression, based on a correlation of experimental data by Mendenhall and Nielsen in reference 8.

$$\frac{x_{sc}}{d} = 1 + \frac{5}{\alpha - 4} \quad (28)$$

where α is in degrees.

Use of Method

The following parameters are required in the application of this method.

Body slenderness ratio, l_B/d

Forebody slenderness ratio, l_F/d

Distribution of cross-sectional area along body, $S(x)$

Position of the moment reference center, x_m

Local crossflow Reynolds number, $Re_n(x)$

Axial distribution of radius, $r(x)$

Length of body, $l_B (= x_B)$

- (1) Determine the apparent mass factor ($K_2 - K_1$), appropriate for the particular configuration, from figure 25.
- (2) Determine K_m from figure 26.
- (3) Find x_{sa} from figure 17.
- (4) Use equation (26) to determine the pitching-moment-curve slope.
- (5) Determine η from figure 27.
- (6) For each angle of attack required, use equation (28) to find the value of x_{sc} .
- (7) Find the local value of C_{dc} for every section from figure 18.
- (8) Use equation (27) to determine the nonlinear pitching moment.

Numerical Example. This example compares the method with data from the present test. The configuration chosen is N2C2B2 at a free stream Reynolds number of 16.2×10^6 , based on body length. The planform of this configuration is given in figure 19. The values of the required parameters are

Body slenderness ratio: $l_B/d = 7$.

Forebody slenderness ratio: $l_F/d = 5$.

Distribution of cross-sectional area along body:

This body can be described analytically. The following equations describe the cross-sectional area.

Nose:
$$s(x) = \frac{\pi}{4} [d^2 - (x - d)^2] \quad 0 \leq x \leq d$$

Center section:
$$s(x) = \frac{\pi d^2}{4} \quad d < x \leq 5d$$

Base:
$$s(x) = \frac{\pi d^2}{4} \left[1 - \frac{(x - 5d)^2}{2d} \right]^2 \quad 5d < x \leq 7d$$

Body diameter: $d = 7$ in.

Position of moment
reference center: $x_m = 30.5$ in.

Axial distribution of radius

Nose:
$$r(x) = \left[\frac{d^2}{4} - \frac{(x - d)^2}{4} \right]^{1/2} \quad 0 \leq x \leq d$$

Center section:
$$r(x) = \frac{d}{2} \quad d < x \leq 5d$$

Base:
$$r(x) = \frac{d}{2} \left[1 - \frac{(x - 5d)^2}{2d} \right] \quad 5d < x \leq 7d$$

Length of body: $x_B = 49$ in.

- (1) From figure 25, $(K_2 - K_1) = 0.898$
- (2) From figure 26, $K_m = 0.940$
- (3) Using figure 17, $x_{ga}/l_b = 0.455$. Since $l_b/d = 2$ for base B2, $x_{ga}/d = 0.910$, measured from the start of the base section. Measured from the nose, $x_{ga}/d = 5.91 + x_{ga} = 3.4475$ ft. This is the upper limit of integration in equation (26).
- (4) Substituting the necessary quantities into equation (26) and carrying out the integration

$$C_{M_\alpha} = 8.043 \text{ rad}^{-1}$$

- (5) From figure 27, $\eta = 0.635$
- (6) Find x_{sc}/d at 7° , 10° , 13° , from equation (28)

α°	x_{sc}/d
7	2.667
10	1.833
13	1.556

- (7) The crossflow-drag coefficient, from figure 18 is 0.290 for all sections.
- (8) The results of the integration of equation (27) are

α°	$C_{M_{n1}}$
7	-0.4367
10	-0.0091
13	+0.0963

Thus, the final result for the pitching moment is shown in figure 28. The agreement is quite good, especially at the lower angles of attack. This indicates that the estimation of the pitching-moment-curve slope is very accurate. The present method does underestimate the nonlinear portion of the pitching moment somewhat, but for initial design purposes the agreement is considered adequate. Possibilities for the

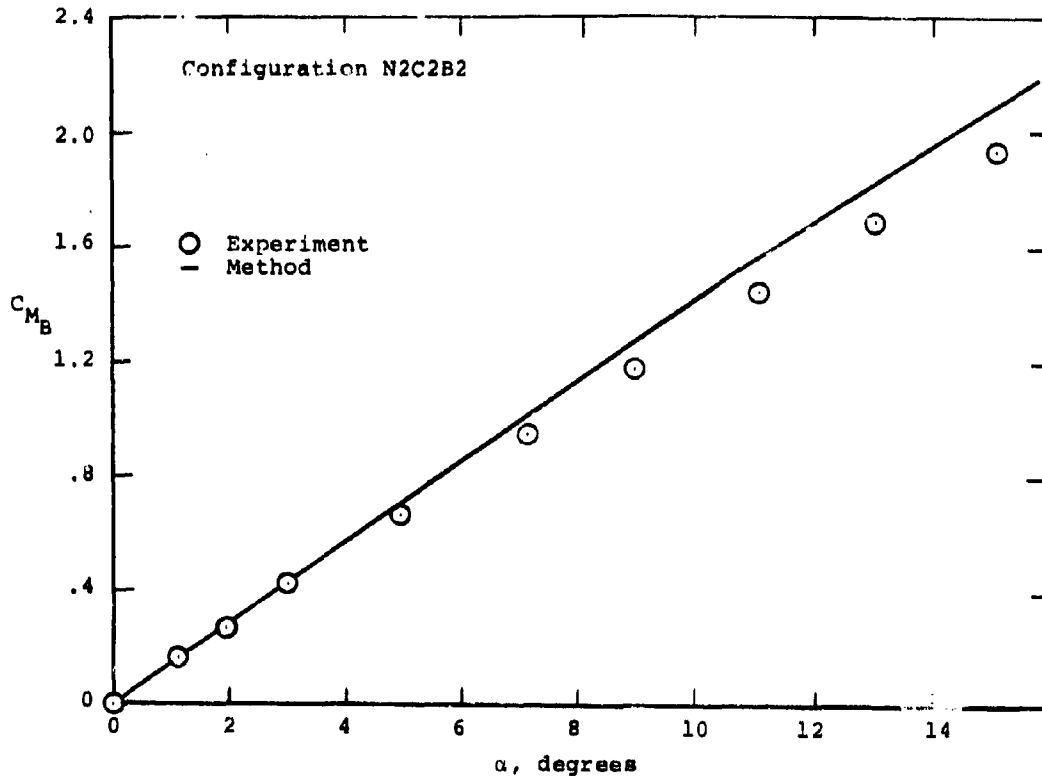


FIGURE 23. COMPARISON BETWEEN PREDICTED AND EXPERIMENTAL BODY-ALONE PITCHING-MOMENT COEFFICIENT.

causes of the discrepancy in $C_{M_{n1}}$ include the position of crossflow separation, x_{sc} , and the form of the viscous-force distribution along the body axis. Additional comparisons are given in figures 29 and 30. Agreement is quite good for both cases.

V.4 BODY-ALONE AXIAL-FORCE COEFFICIENT

This method permits estimation of the body-alone axial-force coefficient on isolated bodies in incompressible flow at angles of attack up to 15° . This procedure consists of first determining the zero angle axial force and then the slope of its curve. Comparison with data from the present test shows very good agreement for all angles.

The axial-force coefficient on isolated bodies of revolution is typified by a finite value at zero angle of attack (zero-angle drag). For bodies used in the present test the behavior as the angle of attack increased from zero was approximately linear with $|\alpha|$. Hence, a representative equation is one of the form

$$C_{A_B} = a_0 + a_1 |\alpha| \quad (29)$$

For incompressible flow, the sources of zero-angle axial force are base drag and skin friction; i.e.,

$$a_0 = C_{o_f} + C_{o_b} \quad (30)$$

It is common practice (e.g., refs. 10 and 13) to treat these two sources independently. Drag due to skin friction is based on the well-documented values for turbulent skin-friction coefficient on a flat plate (e.g., ref. 13), modifying for thickness effects of a body of revolution, and applying it to the actual surface area of the body under test. Based on experimental data, plus the best available information for calculating skin friction (ref. 13), equation (30) was used to identify the base drag in the present test.

Examination of the data revealed a strong dependence of C_{o_b} on base length. In addition, the base drag for a particular configuration displayed a slight dependence on

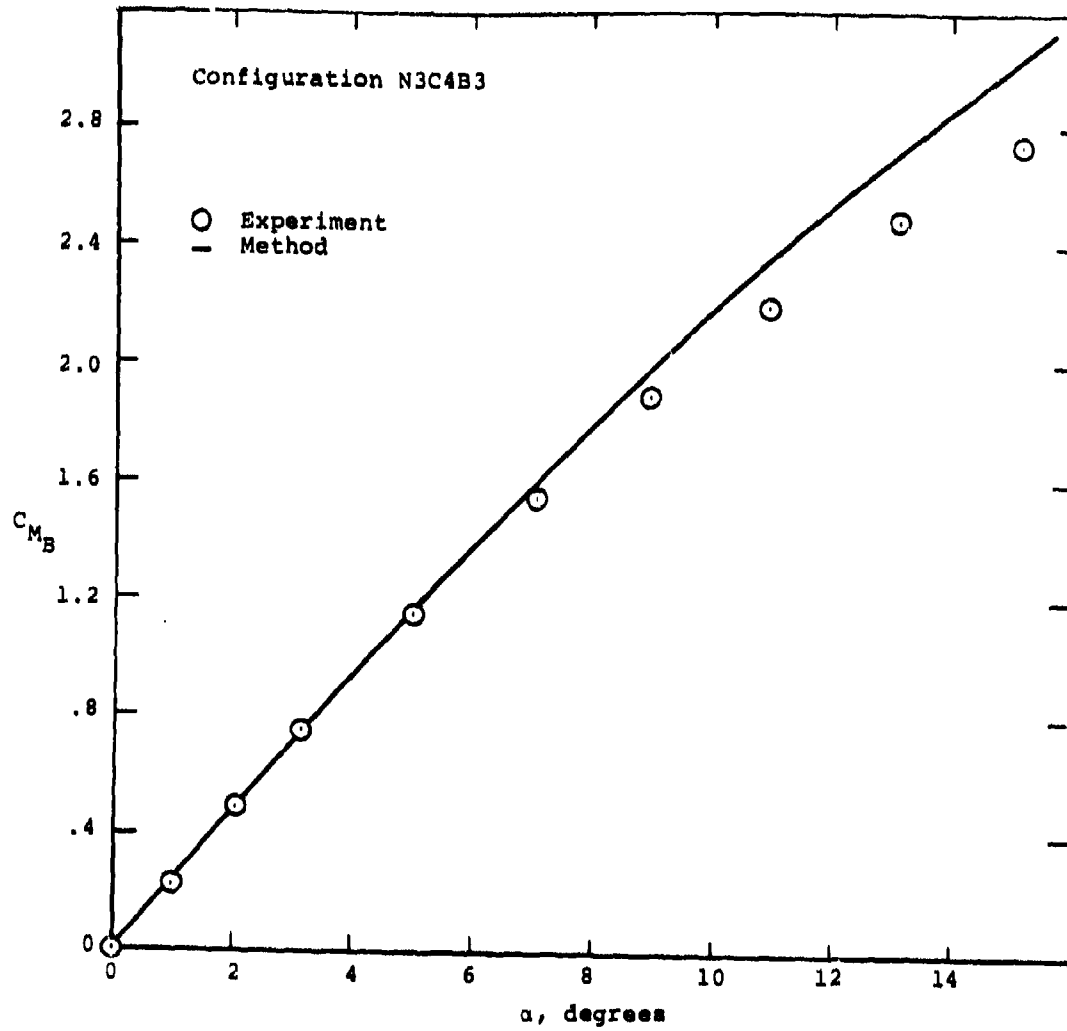


FIGURE 29. COMPARISON BETWEEN PREDICTED AND EXPERIMENTAL BODY-ALONE PITCHING-MOMENT COEFFICIENT.

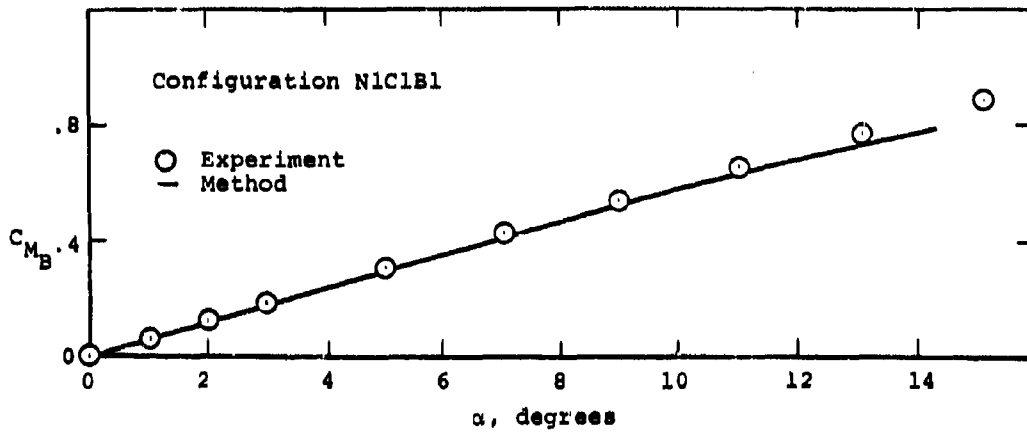


FIGURE 30. COMPARISON BETWEEN PREDICTED AND EXPERIMENTAL BODY-ALONE PITCHING-MOMENT COEFFICIENT.

the free stream Reynolds number, being slightly greater at the larger Reynolds number. There was also a dependence on the length of the body that can be related to skin-friction effects. Finally, negligible effect of nose type was observed.

Description of Method

Zero-Angle Axial Force, $(C_{A_B})_0$. To determine the value of the axial-force coefficient at zero angle of attack the contributions from the base and skin friction are summed. For bodies with conical base sections and sharp center section-base section junctions, the base drag is given in figure 31 as a function of base length. The curves in this figure were determined as described above from equation (30) using zero-angle axial force for three configurations having identical forebodies and differing bases.

Drag due to skin friction on bodies of revolution is well predicted using values for the turbulent skin-friction coefficient on a flat plate. This value is applied to the actual surface area exposed to potential flow (i.e., nose, downstream to x_{sa}), with a term for thickness effects included. Such a relation is expressed by the following equation.

$$C_{O_f} = C_f \left[1 + 1.5 \left(\frac{d}{l_{sa}} \right)^{3/2} \right] \frac{S_w}{S_R} \quad (31)$$

The quantity in brackets is a geometrical term for the effect of thickness (ref. 13). Normally, the length chosen, l_{sa} , is the distance back to x_{sa} , the point of axial flow separation. Similarly, S_w is the surface or wetted area from the nose to x_{sa} . The value of C_f , the skin-friction coefficient based on wetted area, is given by the Schoenherr equation (ref. 13 or 14), equation (32), and plotted in figure 32 for convenience. The equation is based on a similarity rule derived by von Kármán (see ref. 13).

$$\log(Re_{sa} C_f) = \frac{0.242}{\sqrt{C_f}} \quad (32)$$

In this relation, C_f is the turbulent skin-friction coefficient based on exposed surface area and Re_{sa} is the Reynolds number based on plate length. Thus, when determining the value of C_f from figure 32, the value of

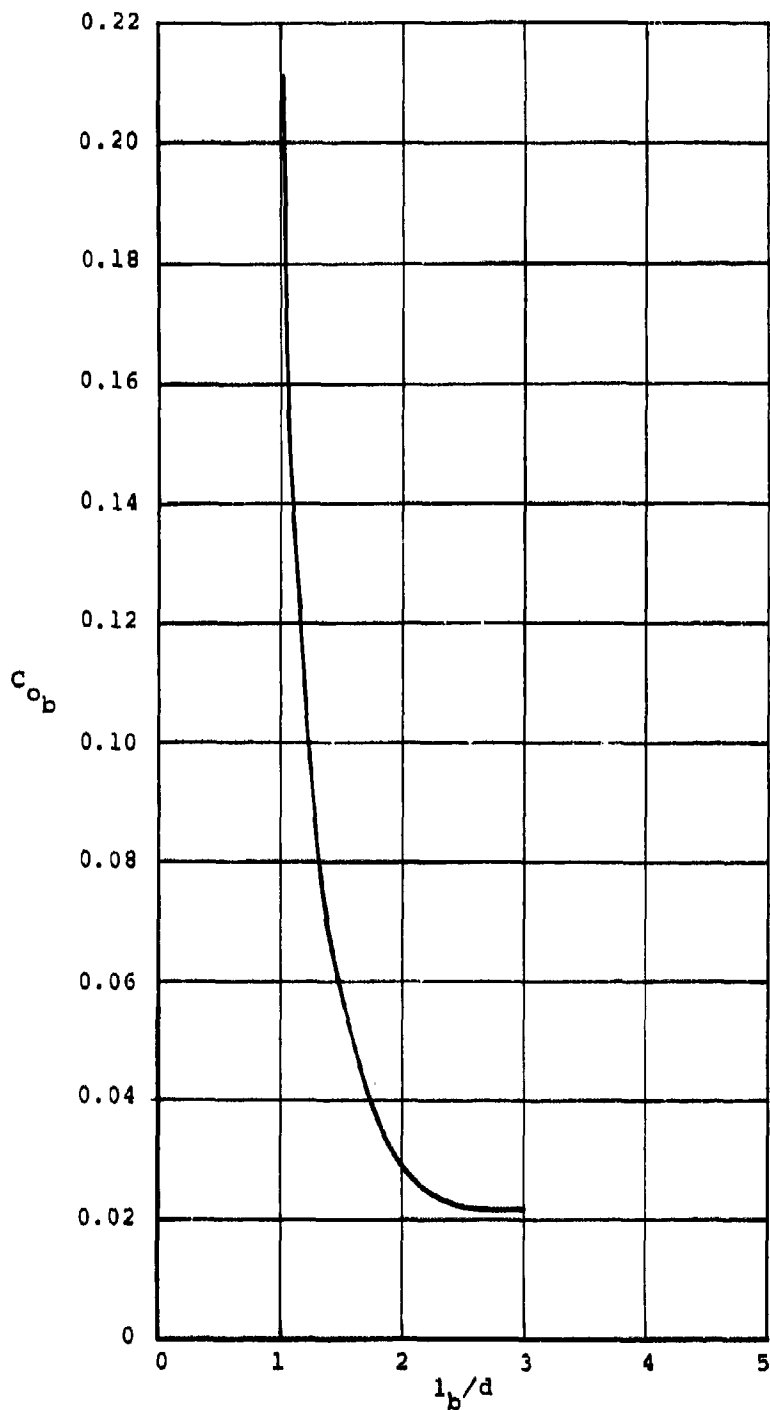


FIGURE 31. ZERO-ANGLE BASE DRAG VS. AFTERBODY FINENESS RATIO.

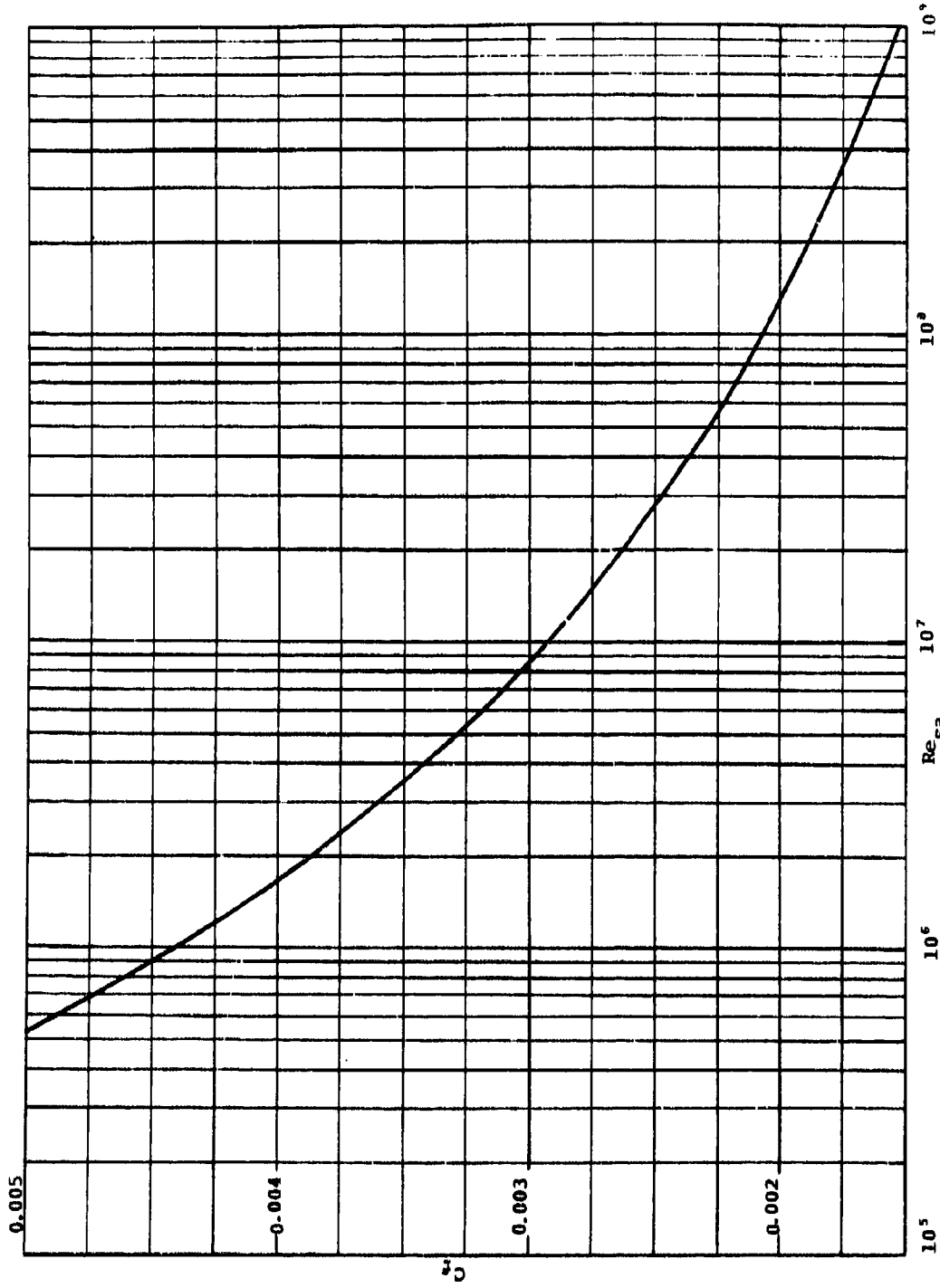


FIGURE 32. SKIN FRICTION DRAG COEFFICIENT ON PLANE SURFACE IN INCOMPRESSIBLE FLOW (REF. 14).

Reynolds number based on the length of the body exposed to potential flow (l_{sa}) should be used.

Variation of C_{AB} with Angle of Attack. Analysis of the data from the present test showed that, to a very close approximation, C_{AB} varied linearly with angle of attack.

The value of the axial-force-curve slope is essentially independent of nose shape and Reynolds number and is basically a function of the length of the center section plus the base section. The variation of the axial-force-curve slope, a_1 , with center section and base section length is shown in figure 33 which is based on the experimental data.

Use of Method

This section demonstrates how the method is to be used and makes comparisons with data. The following parameters are required for the application of this method.

Base length, in calibers, l_b/d

Length of body exposed to potential flow, in calibers, l_{sa}/d

Surface area of portion of body exposed to potential flow, S_w .

Reynolds number based on the length l_{sa} , Re_{sa} .

Center section length, in calibers, l_c/d .

General Description.

1. Determine base drag, C_{O_b} , from figure 31.
2. Find skin-friction coefficient from figure 32 or equation (32).
3. Calculate skin-friction drag, C_{O_f} , from equation (31).
4. Add results from steps (1) and (3) to find zero-angle axial force, $(C_{AB})_0$.
5. Find axial-force-curve slope, a_1 , from figure 33.

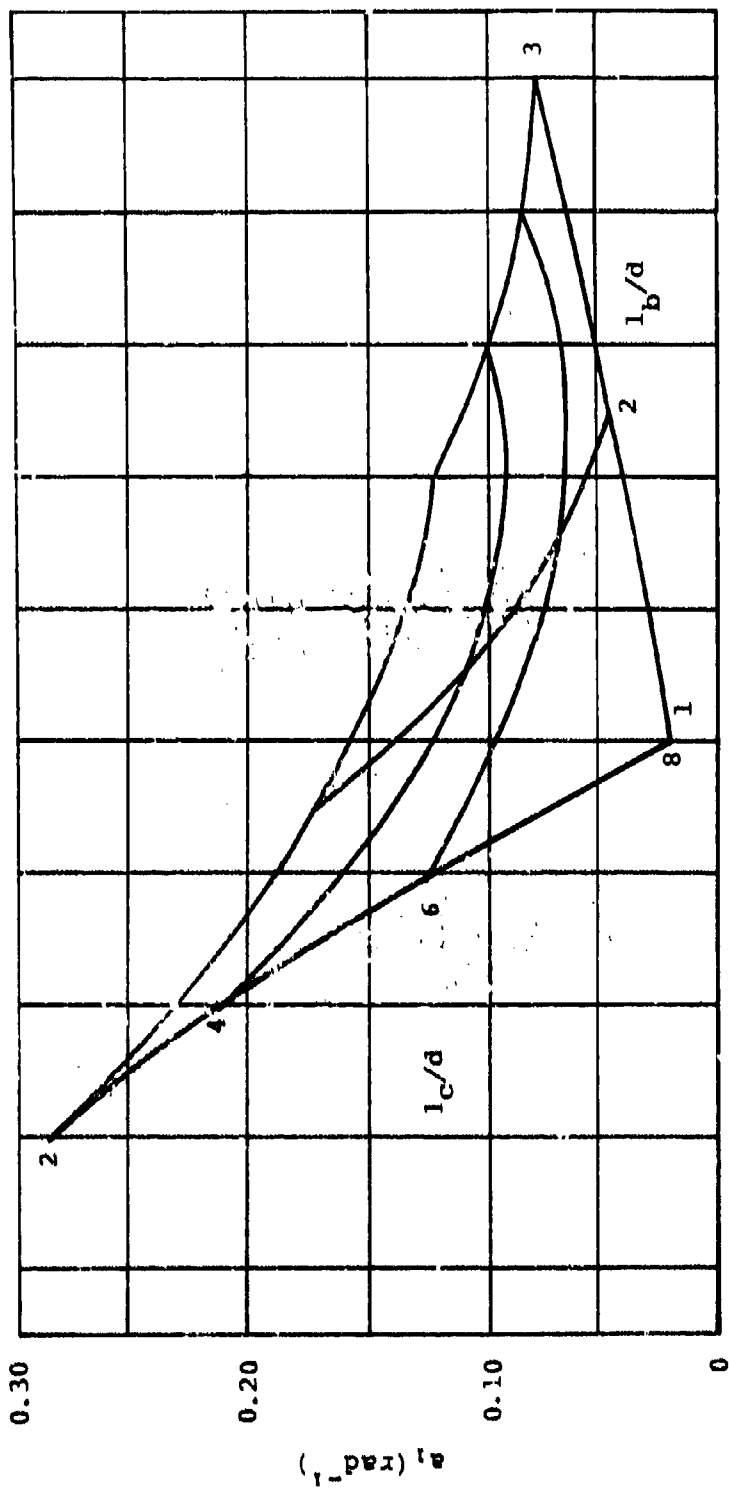


FIGURE 33. FIRST ORDER TERM FOR BODY-ALONE AXIAL FORCE COEFFICIENT.

6. Use equation (29) to find axial-force coefficient as a function of angle of attack.

Numerical Example. This example compares the method to data from the present test. The configuration chosen is N3C2B2, at a free-stream Reynolds number of 40×10^6 based on body length. The values of the required parameters are:

- Base length, $l_b/d = 2.0$.
 - Length of body exposed to potential flow, using figure 17 (Section V.2), $l_{sa}/d = 6.860$.
 - Surface area of body exposed to potential flow, $S_w = 6.743 \text{ ft}^2$.
 - Reynolds number based on l_{sa} , $Re_{sa} = 34.18 \times 10^6$.
 - Center section length, $l_c/d = 6.0$.
1. From figure 31, $C_{o_b} = 0.0282$.
 2. Figure 32 gives $C_f = 0.00242$.
 3. Using equation (31), $C_{o_f} = 0.0661$.
 4. Adding C_{o_b} and C_{o_f} , $(C_{A_B o}) = 0.0943$.
 5. From figure 33, $a_1 = 0.1089$ per radian.
 6. Thus, $C_{A_B} = 0.0943 + 0.1089 \alpha$

This estimate is compared to the experimental values in figure 34. The agreement is excellent throughout the angle of attack range. Further comparisons between the experiment and estimates from the present method are shown in figures 35 and 36. Agreement is excellent in both cases.

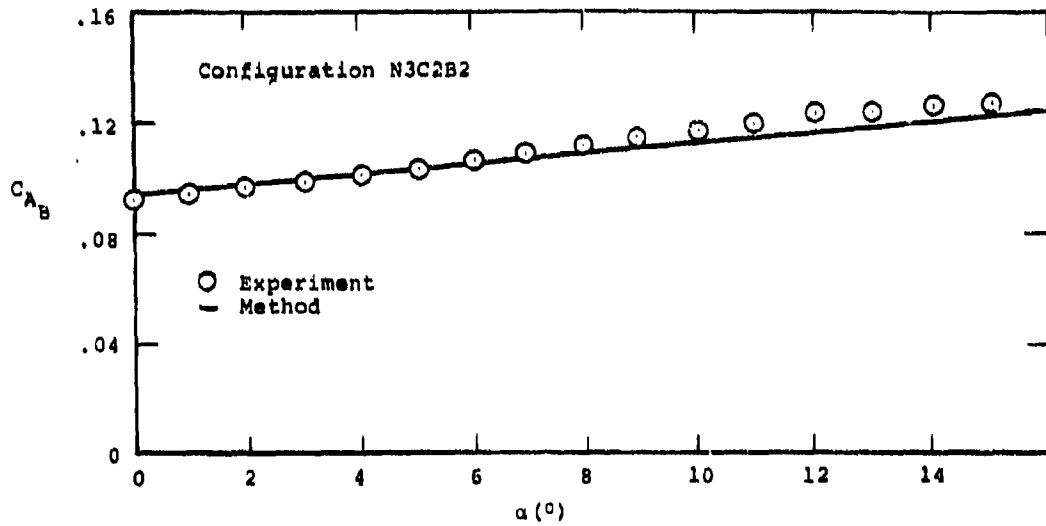


FIGURE 34. COMPARISON BETWEEN PREDICTED AND EXPERIMENTAL BODY-ALONE AXIAL FORCE COEFFICIENT.

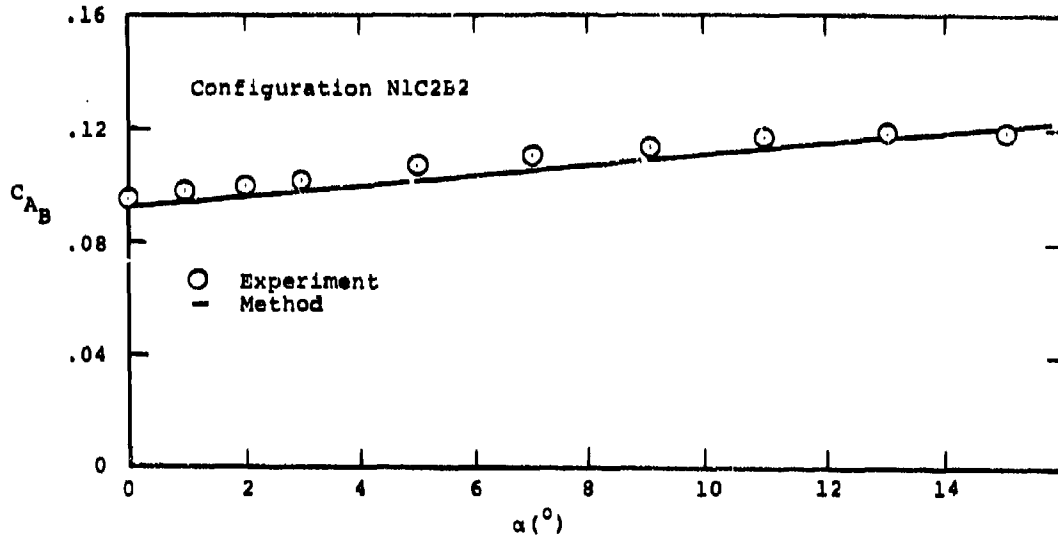


FIGURE 35. COMPARISON BETWEEN PREDICTED AND EXPERIMENTAL BODY-ALONE AXIAL FORCE COEFFICIENT

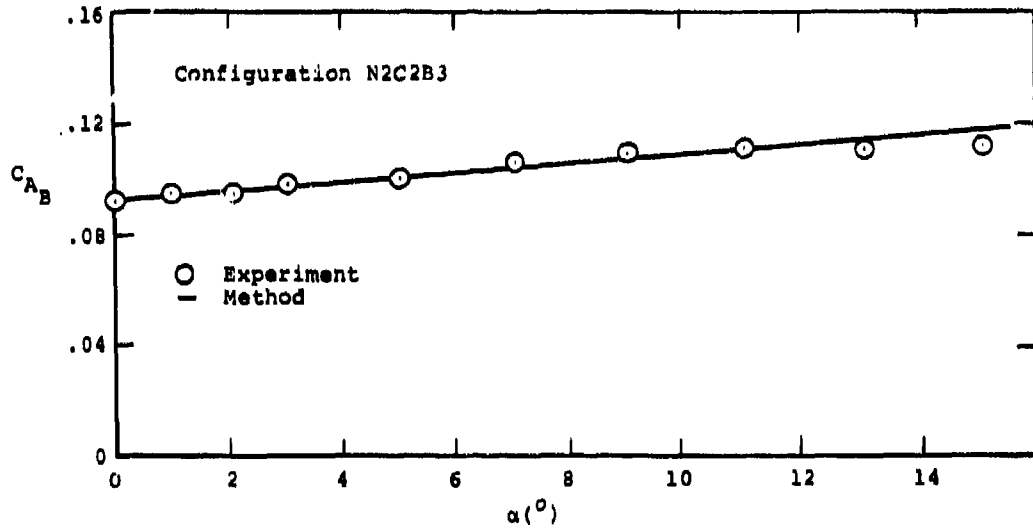


FIGURE 36. COMPARISON BETWEEN PREDICTED AND EXPERIMENTAL BODY-ALONE AXIAL FORCE COEFFICIENT.

(Reverse Page 80 Blank)

VI. ISOLATED TAILS

VI.1 GENERAL CONSIDERATIONS

When a low aspect ratio tail is placed in an airstream, attached and separated flows are induced, in much the same way as on a body alone. At low angles of attack, the flow is attached over the whole tail. At angles greater than about 6 degrees, however, the boundary layers at the leading and side edges separate and roll up into large vortices on the upper surface, Fig. 37. These vortices produce suction which increases the total normal force on the wing. This normal force increases nonlinearly with angle of attack. The magnitude of the nonlinear force has been found (Ref. 1) to be dependent upon several of the wing geometrical parameters. In particular, the force increases as the leading edge becomes sharper. For tails typical of submersible vehicles, the relatively blunt leading edges used mean that additional control power could be obtained by sharpening the leading edge.

VI.2 TAIL-ALONE NORMAL-FORCE COEFFICIENT

This method permits calculation of the normal-force coefficient of low-aspect-ratio isolated tails with rounded leading edges and blunt trailing edges. This method is valid for incompressible flow and for angles of attack up to 30° . The method is divided into two steps. First, the normal-force curve slope at zero angle is determined as a function of aspect-ratio and trailing-edge shape. Second, a nonlinear term is determined as a function of aspect ratio, taper ratio, and Reynolds number to account for viscous effects.

The normal force on a low-aspect-ratio lifting surface (wing or tail) can be thought of as consisting of two contributions. The first is well-approximated by potential-flow theory and is linear. The second is due to the action of viscosity and is highly nonlinear. At angles of attack greater than a few degrees, tail normal force can become dominated by the nonlinear viscous effects. Potential-flow

theory does not take the nonlinear phenomena into account. It would be desirable to be able to calculate both of these effects exactly. However, the current state of nonlinear theory is such that it is not possible to do this, in general, with any accuracy. Fortunately, for preliminary design purposes, an exact calculation is unnecessary. The following semi-empirical method was formulated to combine the two effects in a convenient manner for use in preliminary design.

The method is similar to those based on the crossflow drag analogy such as described by Flax and Lawrence (Ref. 15). In these methods the normal-force coefficient is assumed to be of the form

$$C_{N_T} = a_1 \alpha + a_2 \alpha^2 \quad (33)$$

Taking the derivative of this equation we see that a_1 is equal to the zero angle normal-force curve slope, i.e.,

$$a_1 = \left(\frac{dC_{N_T}}{d\alpha} \right)_0 \quad (34)$$

The constant a_2 is chosen such that the full expression provides the best overall comparison to the experimental data.

Normal-Force Curve Slope

Correlation of the experimental data showed that, for aspect ratios less than or equal to one, the normal-force curve slope is very well predicted by slender wing theory; i.e.,

$$C_{N_\alpha} = \frac{\pi}{2} AR \quad \text{for } AR \leq 1.0 \quad (35)$$

For higher aspect ratios the experimental data fell below the slender body theory prediction. This trend is well known and is documented in reference 15. More refined potential flow theories are available which predict this trend and give much better agreement with experiment at higher aspect ratios for wings with sharp trailing edges. A comparison between data from the current work and from previous tests is shown in figure 38. It may be seen that the normal-force-curve slopes derived from the present data are generally greater than those found in other experiments. This is believed to be an effect of trailing-edge shape as shown by Hoerner

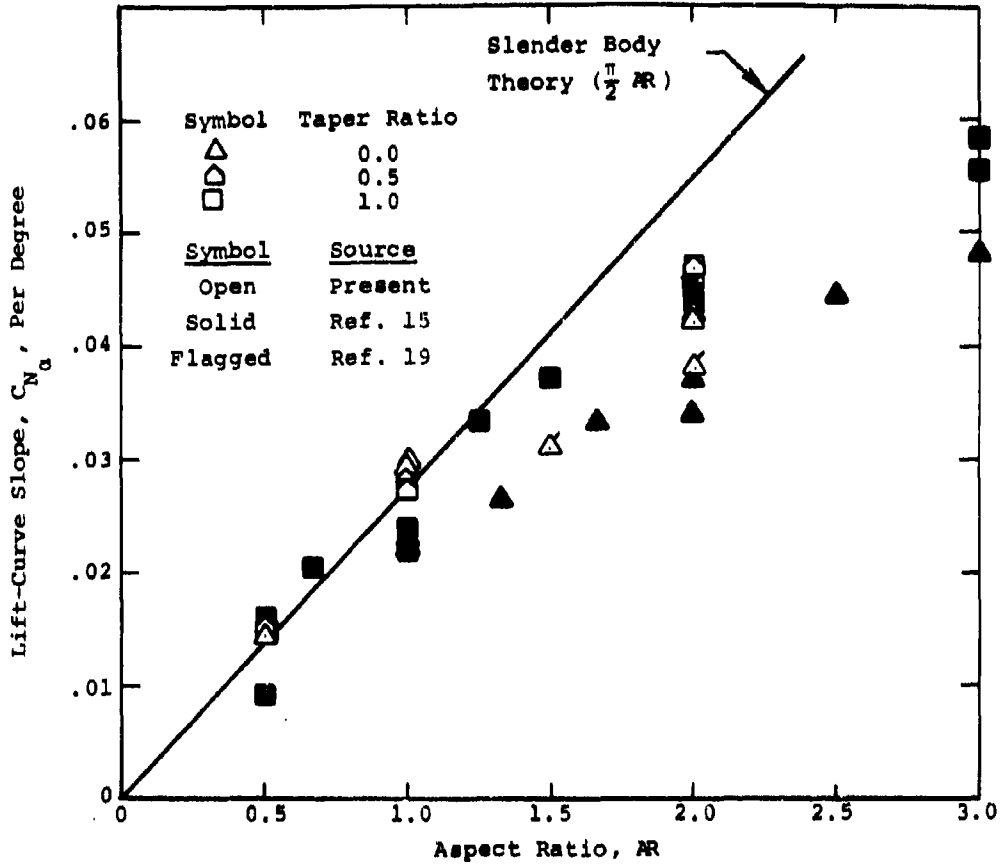


FIGURE 38. MEASURED VALUES OF LIFT-CURVE SLOPE.

(Ref. 16). A wing section with a blunt trailing edge, as in the present experiment, has a greater normal-force-curve slope than the same section with a sharp trailing edge, as seen in figure 39 (Ref. 16). Hence, a suitable prediction method for $C_{N\alpha}$ should include trailing-edge shape as a parameter.

Examination of the data for the effect of taper ratio shows that, for blunt trailing edges (the present data), taper ratio has a negligible effect. For sharp trailing edges however, there is a slight effect, with rectangular wings having slightly higher normal-force-curve slopes than delta wings.

The effect of Reynolds number over the range tested (4×10^6 to 8.5×10^6 per foot) had an insignificant influence on $C_{N\alpha}$. This was confirmed by a study by Jones (Ref. 17) who found only a very small increase in $C_{N\alpha}$ with Reynolds number.

It is clear then, that any method for predicting normal-force-curve slope should include aspect ratio, shape of the trailing edge, and, for wings with a sharp trailing edge, the taper ratio. These effects are summarized in figures 40(a) and (b) which constitute the recommended curves for determination of the normal-force-curve slope. Figure 40(a) is for blunt trailing edges and is a best fit curve to the present data. For aspect ratios less than or equal to one it coincides with the value obtained from slender-wing-theory. The theoretical curves of figure 40(b), recommended for sharp trailing edges, are due to Lawrence (Ref. 18). This theory provides adequate approximations to lifting-surface theory for planforms with straight trailing edges of aspect ratio less than three.

Nonlinear Effects

The understanding and prediction of nonlinear effects on low-aspect ratio wings is not as advanced as the linear portion. Much early work was done trying to develop an expression in terms of a cross-flow-drag coefficient. This theory relates the nonlinear effects to the drag associated with the two-dimensional viscous flow around an infinitely long flat plate in a flow having a velocity equal to the component of the free-stream velocity normal to the wing. This concept, which has been employed here, requires the introduction of a suitable empirical drag coefficient.

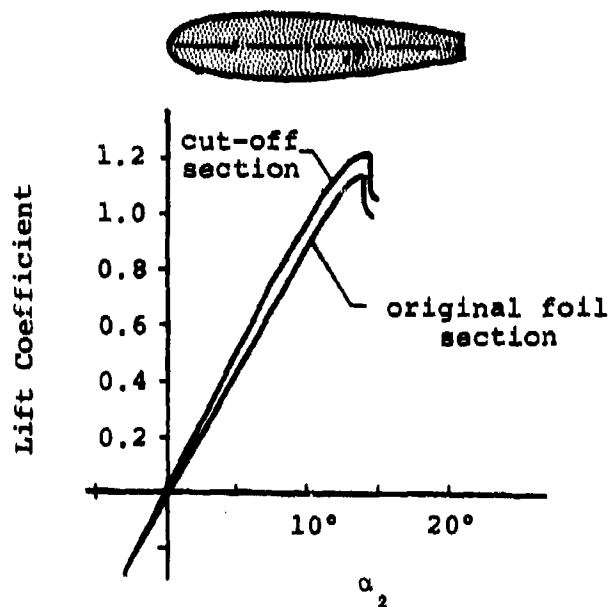


FIGURE 39. EFFECT OF CROPPING TRAILING EDGE ON LIFT CURVE SLOPE (REF. 16).

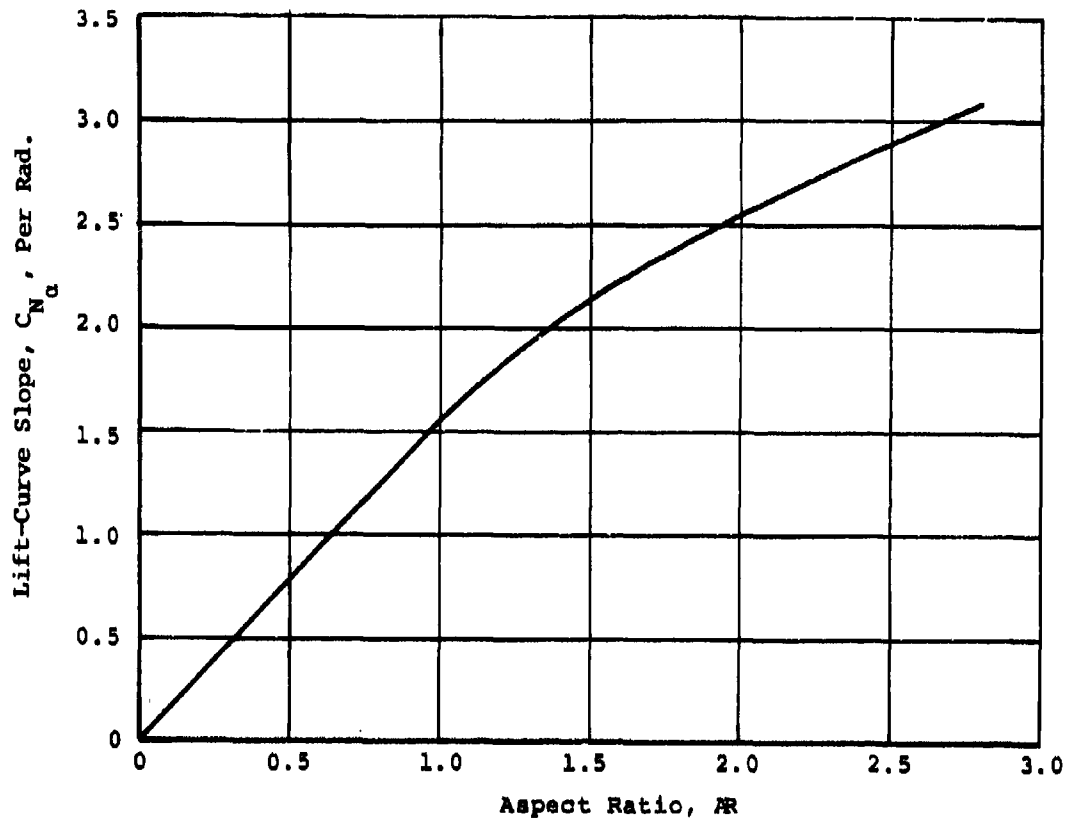


FIGURE 40(a). CURVE FOR LIFT-CURVE SLOPE PREDICTION FOR BLUNT TRAILING EDGES.

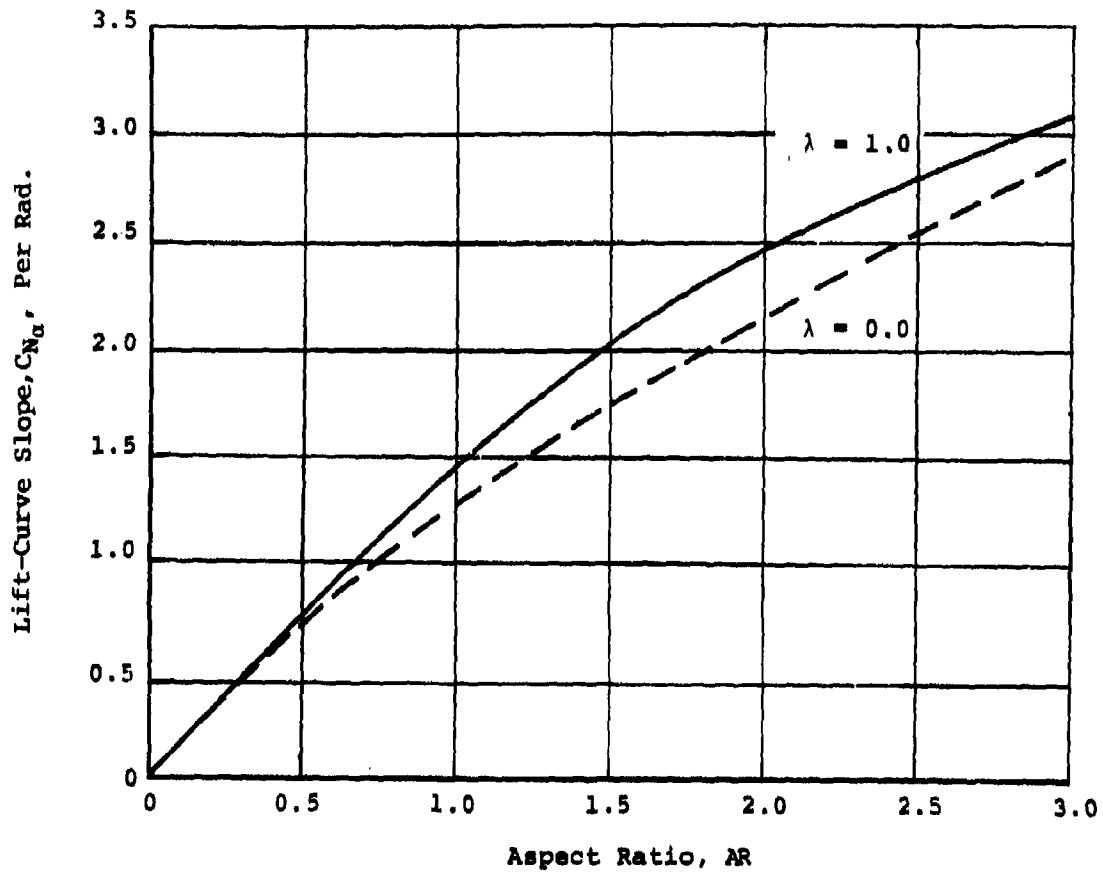


FIGURE 40(b). CURVES FOR LIFT-CURVE SLOPE PREDICTION FOR SHARP TRAILING EDGES.

Values for this coefficient were selected which gave the best overall fit to the experimental data.

Correlation of the present data resulted in the formulation of the curves presented in figures 41(a), (b) and (c) which serve as the recommended values for a_2 in equation (33). The data revealed that a_2 depends strongly on aspect ratio, as well as on the taper ratio and, to a lesser extent, on the Reynolds number. Bartlett and Vidal (Ref. 19) demonstrated further that the value of this coefficient varies with the shape of the leading edge, being greater for sharp leading edges than for rounded leading edges. Since the tails in the present experimental study had rounded leading edges, the curves in figure 41 should be used for wings with similar leading edges.

Use of Method

This section demonstrates the use of the method and makes comparisons with experimental data. The required physical characteristics of the tail are the following:

- Aspect ratio (based on complete, symmetric planform)
- Taper ratio
- Shape of trailing edge
- Reynolds number based on root chord, Re_{CR}

In addition, the leading edge should be rounded and the flow should be incompressible.

General Description.

- (1) Determine the value of C_{N_α} from the appropriate curve of figure 40.
- (2) Determine the appropriate value of a_2 from figure 41.
- (3) Using these two quantities in equation (33), find C_{N_T} as a function of angle of attack (α in radians).

Numerical Example I. This example compares the method with one of the cases in the present experimental study. The case selected is tail T10.

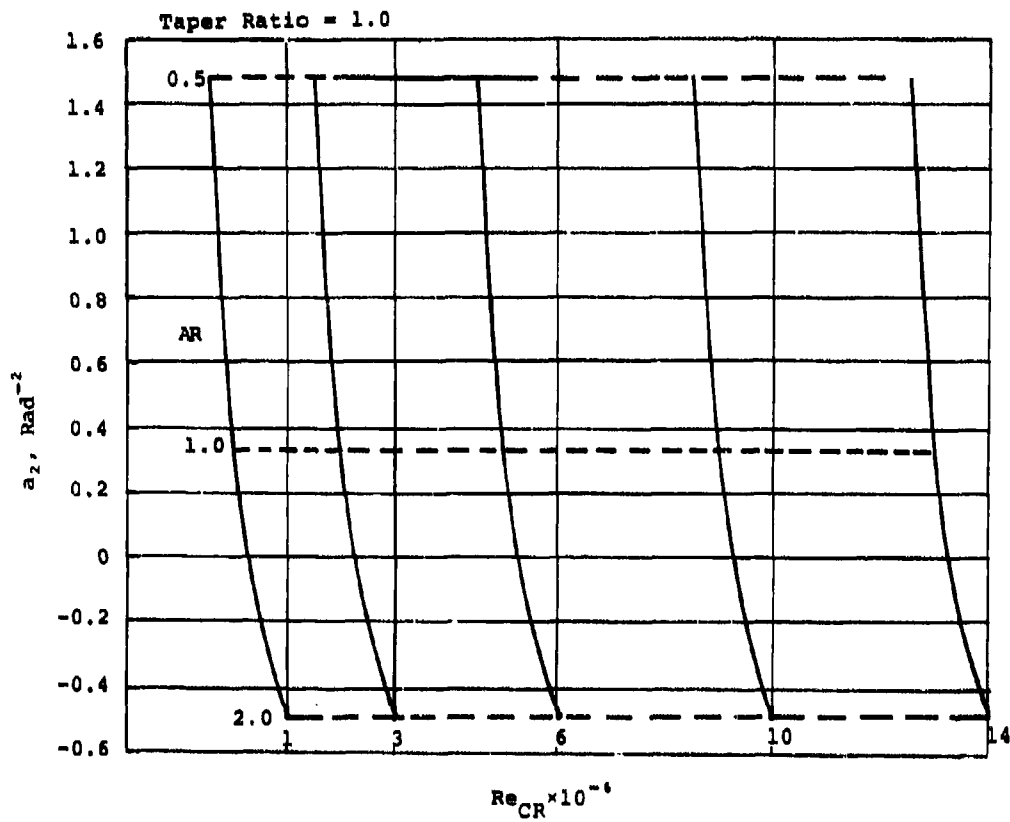


FIGURE 41(a). RECOMMENDED CURVES FOR PREDICTION OF a_2 , COEFFICIENT OF NONLINEAR TERM OF TAIL-ALONE NORMAL FORCE COEFFICIENT; $\lambda = 1.0$.

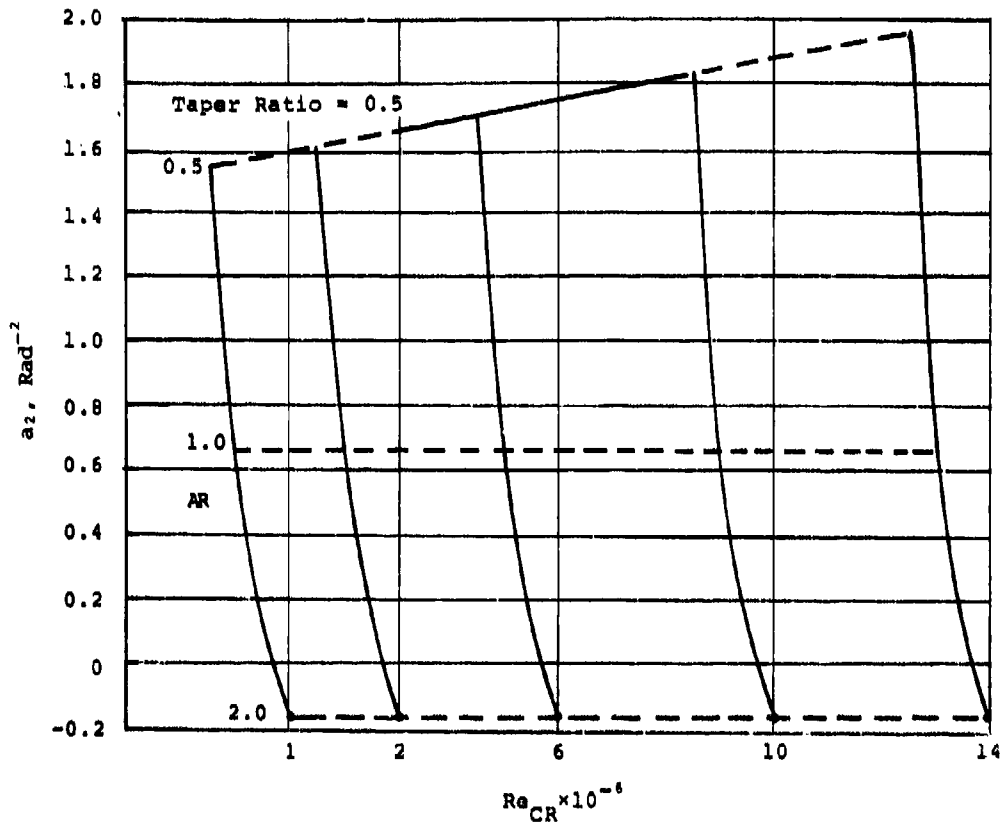


FIGURE 41(b). RECOMMENDED CURVES FOR PREDICTION OF a_2 , COEFFICIENT OF NONLINEAR TERM OF TAIL-ALONE NORMAL FORCE COEFFICIENT; $\lambda = 0.5$.

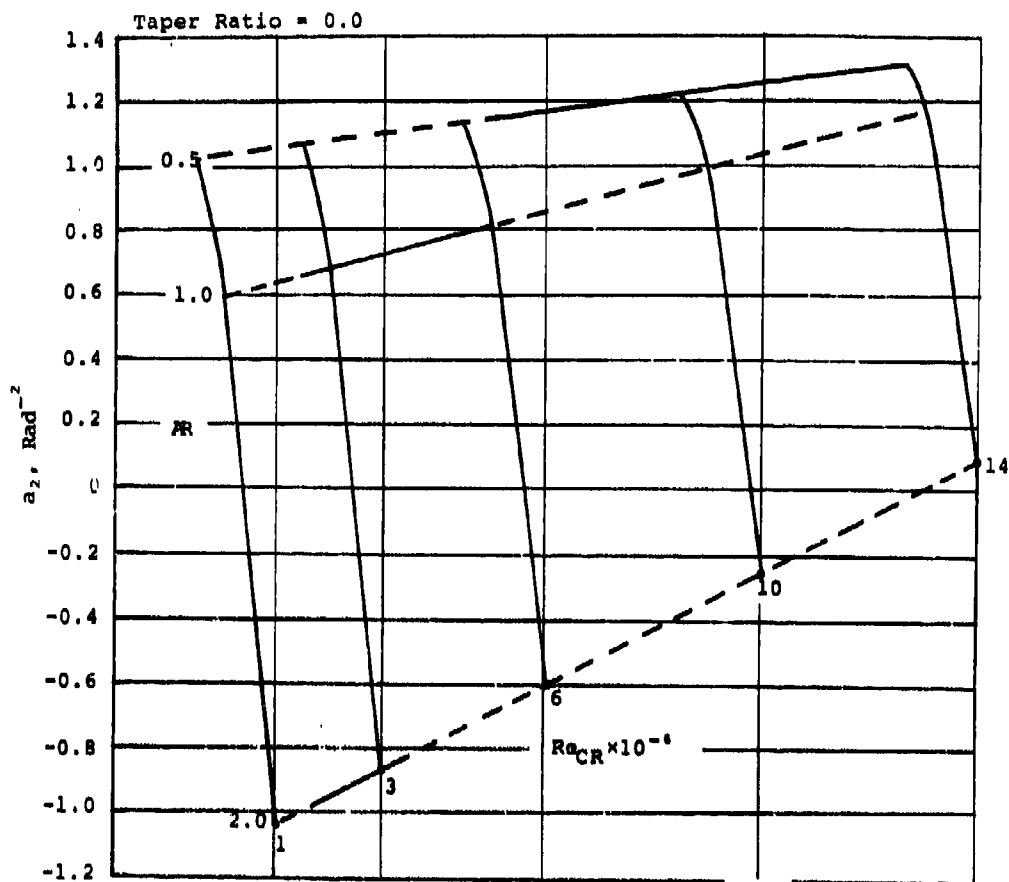


FIGURE 41(c). RECOMMENDED CURVES FOR PREDICTION OF a_2 ,
 COEFFICIENT OF NONLINEAR TERM OF TAIL-ALONE
 NORMAL FORCE COEFFICIENT; $\lambda = 0.0$.

Aspect ratio = 0.5

Taper ratio = 0.5

Shape of trailing edge: Blunt

Reynolds number = 4.35×10^6 , based on the root chord.

- (1) From figure 40(a), for $AR = 0.5$, $C_{N_{\alpha}} = 0.7854 \text{ rad}^{-2}$
- (2) From figure 41(b), for $AR = 0.5$, and $\lambda = 0.5$,
 $a_2 = 1.641 \text{ rad}^{-2}$
- (3) Applying equation (33) we calculate the following values.

α°	C_{N_T}
4	0.0628
8	0.1416
12	0.2364
16	0.3472
20	0.4740
24	0.6168
28	0.7756

The comparison between prediction and data are presented in figure 42. As can be seen, agreement is excellent. This might have been expected since the data themselves formed the basis for the method. The comparison is, however, a necessary step in checking the self-consistency of the method.

Numerical Example II. This example compares the present method with data of Bartlett and Vidal (Ref. 19) on round edge delta wings.

Aspect ratio = 1.5

Taper ratio = 0.0

Shape of trailing edge: Sharp

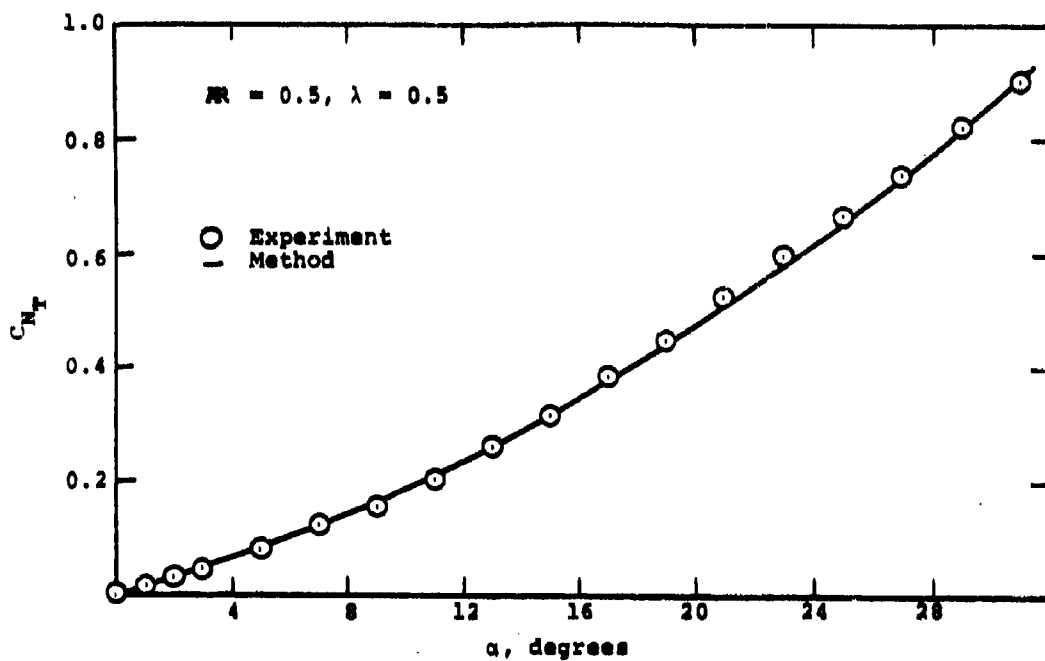


FIGURE 42. COMPARISON BETWEEN PREDICTED AND EXPERIMENTAL TAIL-ALONE NORMAL FORCE COEFFICIENT.

Reynolds number = 3×10^6 , based on root chord

- (1) From figure 40(b), for $AR = 1.5$ and $\lambda = 0.0$,
 $C_{N_\alpha} = 1.74 \text{ rad}^{-1}$
- (2) From figure 41(c), for $AR = 1.5$ and $\lambda = 0.0$,
 $a_2 = -0.094 \text{ rad}^{-2}$
- (3) Applying equation (33) we calculate the following values.

α°	C_{N_T}
4	0.1207
8	0.2406
12	0.3595
16	0.4774
20	0.5945
24	0.7106
28	0.8259

This table is plotted in figure 43 along with the experimental data. The prediction is in reasonably good overall agreement with the data. Below 20° it is very good. In particular, the prediction of C_{N_α} is excellent.

Figures 44 and 45 present similar comparisons of normal-force coefficients for delta wings of aspect ratio 2.0 and 1.33, respectively, the data being taken from references 19 and 20.

VI.3 TAIL-ALONE CHORDWISE CENTER OF PRESSURE

This method permits estimation of the chordwise location of center of pressure for low-aspect-ratio isolated tails with rounded leading edges. The method is valid for angles of attack up to 30° and for incompressible flow. It is derived through correlation of the data from the present test.

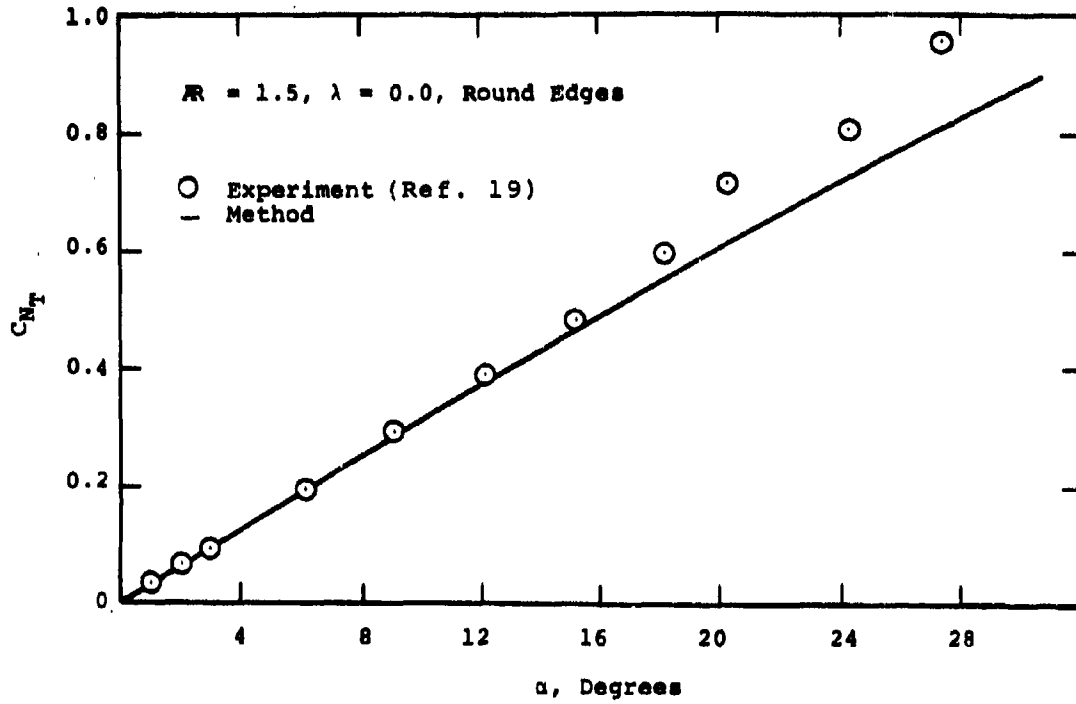


FIGURE 43. COMPARISON BETWEEN PREDICTED AND EXPERIMENTAL TAIL-ALONE NORMAL FORCE COEFFICIENT.

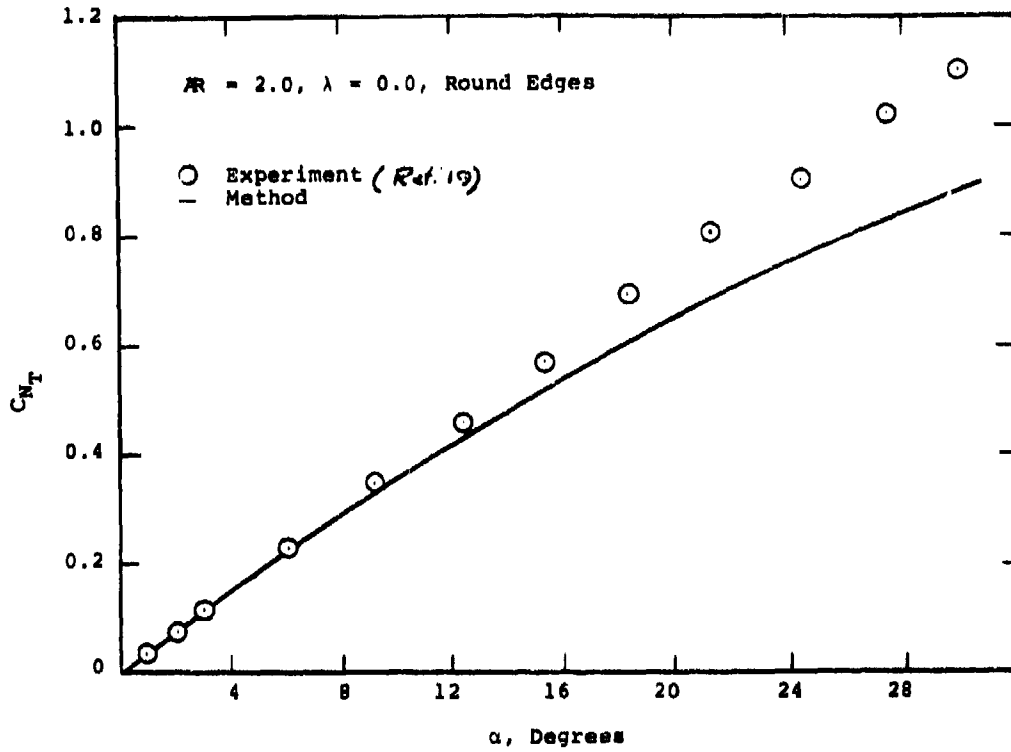


FIGURE 44. COMPARISON BETWEEN PREDICTED AND EXPERIMENTAL TAIL-ALONE NORMAL FORCE COEFFICIENT.

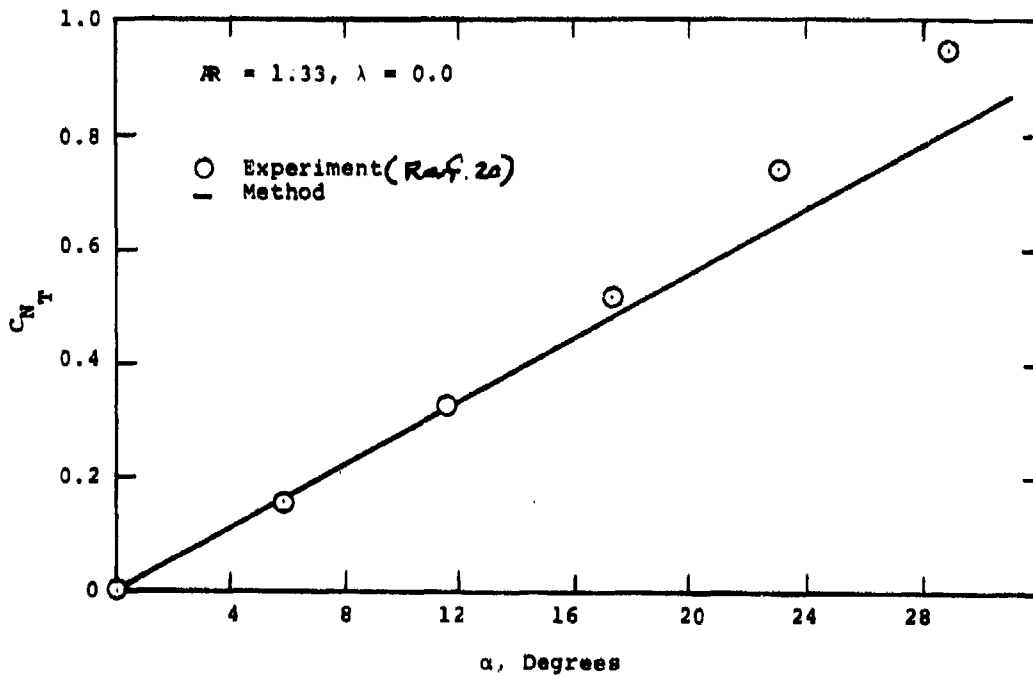


FIGURE 45. COMPARISON BETWEEN PREDICTED AND EXPERIMENTAL TAIL-ALONE NORMAL FORCE COEFFICIENT.

Chordwise center of pressure locations, \bar{X}_T , were calculated from the normal-force and hinge-moment data. The locations are presented in terms of distance from the root chord leading edge and are nondimensionalized by the root chord C_R . For angles of attack greater than a few degrees the data varied smoothly to the maximum angle of attack tested. Estimates of \bar{X}_T at zero degrees angle of attack (\bar{X}_T)₀ were made by determining the slopes of the normal-force and hinge-moment coefficient curves at zero degrees. These curves formed the basis for the method.

The zero-angle centers of pressure are compared to various linear theories and other data in figure 46. Centers of pressure from the present investigation are seen to be slightly downstream of both theoretical values and measured values from other experiments. This is believed caused by the blunt trailing edge on the fins used in the present investigation. As discussed in the previous section, a wing with a blunt trailing edge has a greater value of the normal-force curve slope than the same wing profile with a sharp trailing edge. This implies additional loading over the aft portion of the wing. Hence, a center of pressure that is further downstream than a wing with a sharp trailing edge is consistent with the present data.

For the case of incompressible flow we would expect the location of the chordwise center of pressure to be, in general, a function of taper ratio, aspect ratio, angle of attack, and Reynolds number; i.e.,

$$\bar{X}_T = \bar{X}_T(\lambda, AR, \alpha, Re_{CR}) \quad (36)$$

Close examination of the data revealed that \bar{X}_T depended strongly on taper ratio and angle of attack, varied slightly with aspect ratio, and was essentially independent of the Reynolds number. These findings can be expressed as

$$\bar{X}_T = F_1(\lambda, \alpha) F_2(AR). \quad (37)$$

Curves of $F_1(\lambda, \alpha)$ are shown in figures 47(a), (b) and (c) for the three aspect ratios tested. The differences between the curves at the same taper ratio shows the dependence on aspect ratio.

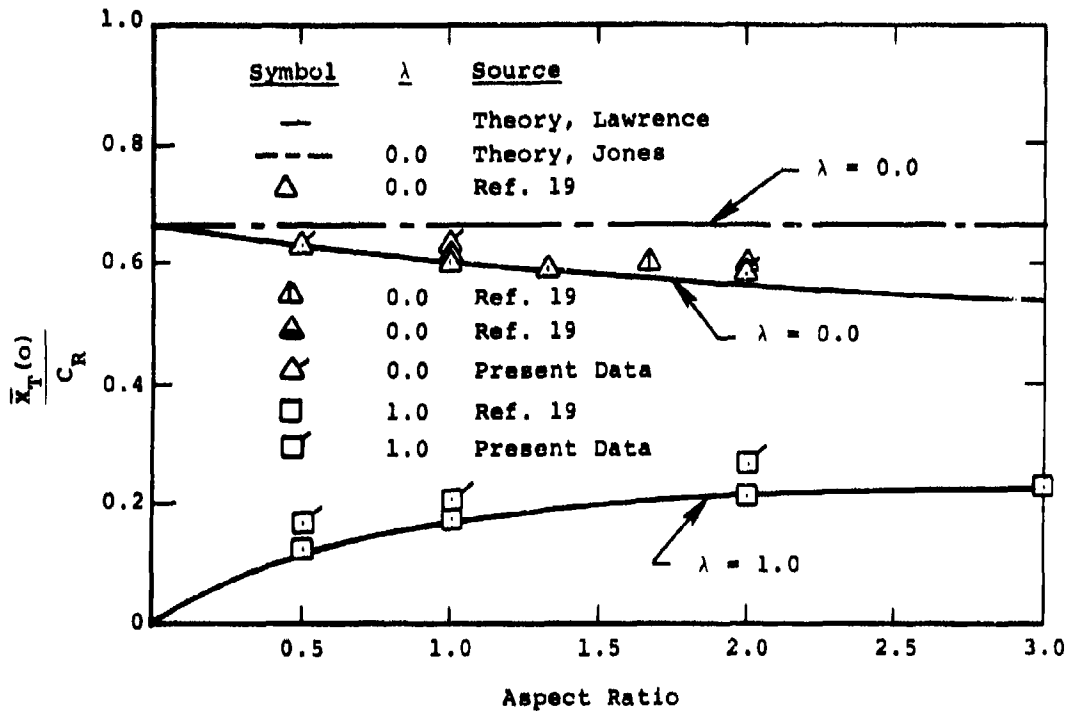


FIGURE 46. TAIL-ALONE CHORDWISE CENTER OF PRESSURE AT ZERO ANGLE.

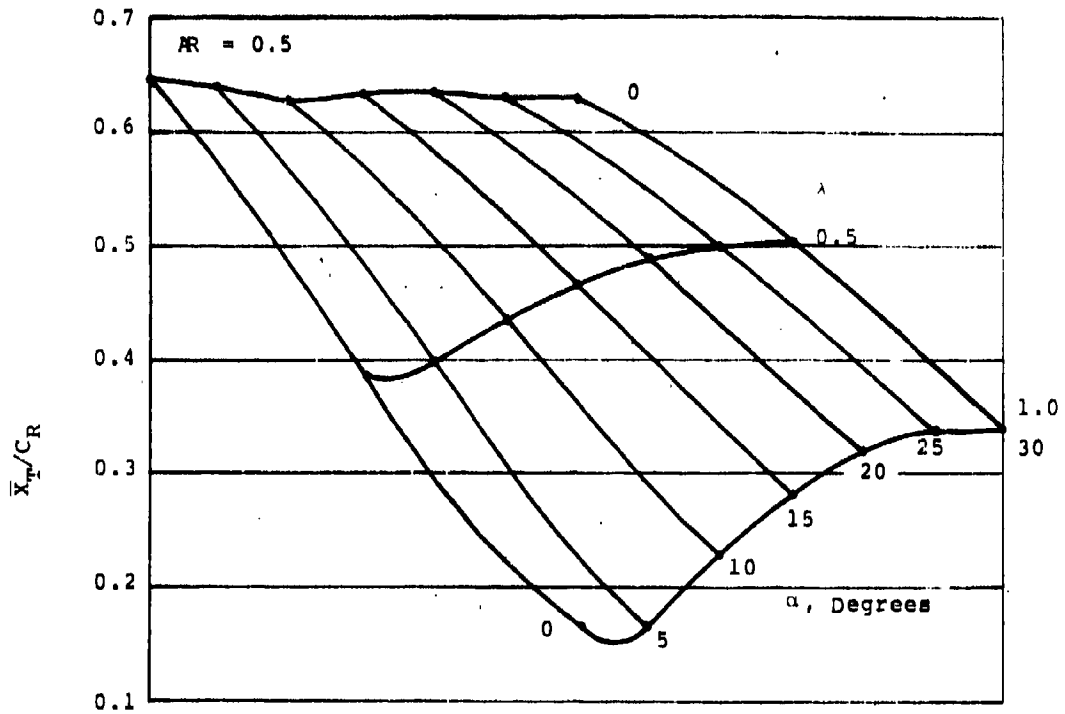


FIGURE 47(a). TAIL-ALONE CHORDWISE CENTER OF PRESSURE PREDICTION CURVE, $AR = 0.5$.

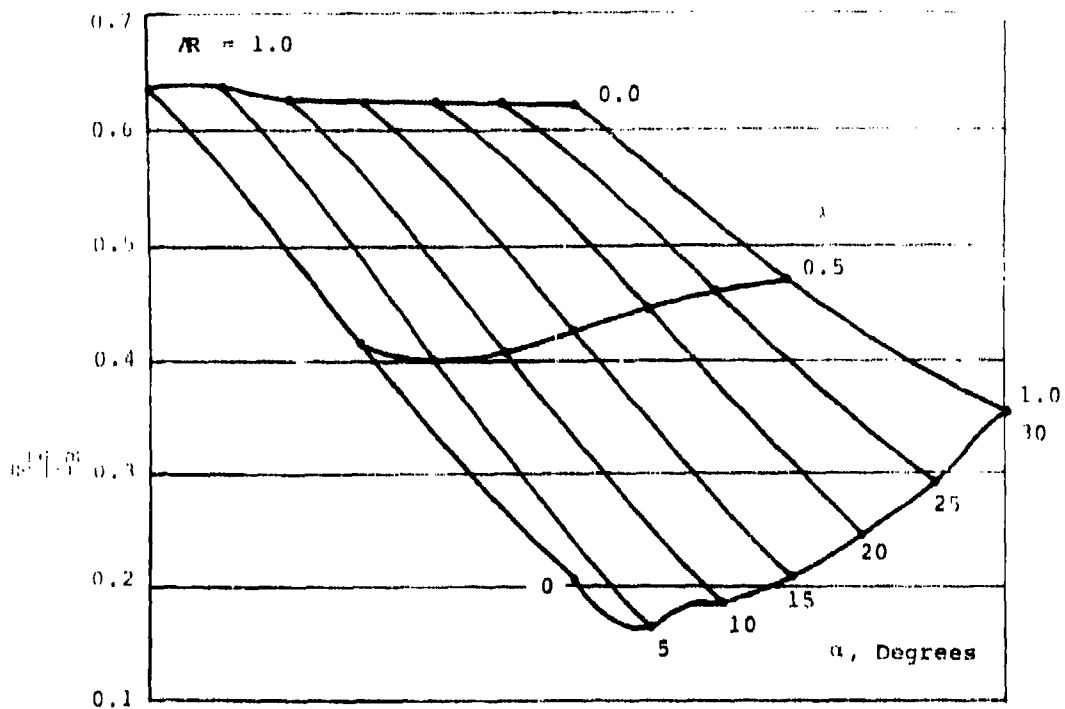


FIGURE 47(b). TAIL-ALONE CHORDWISE CENTER OF PRESSURE PREDICTION CURVE; $AR = 1.0$.

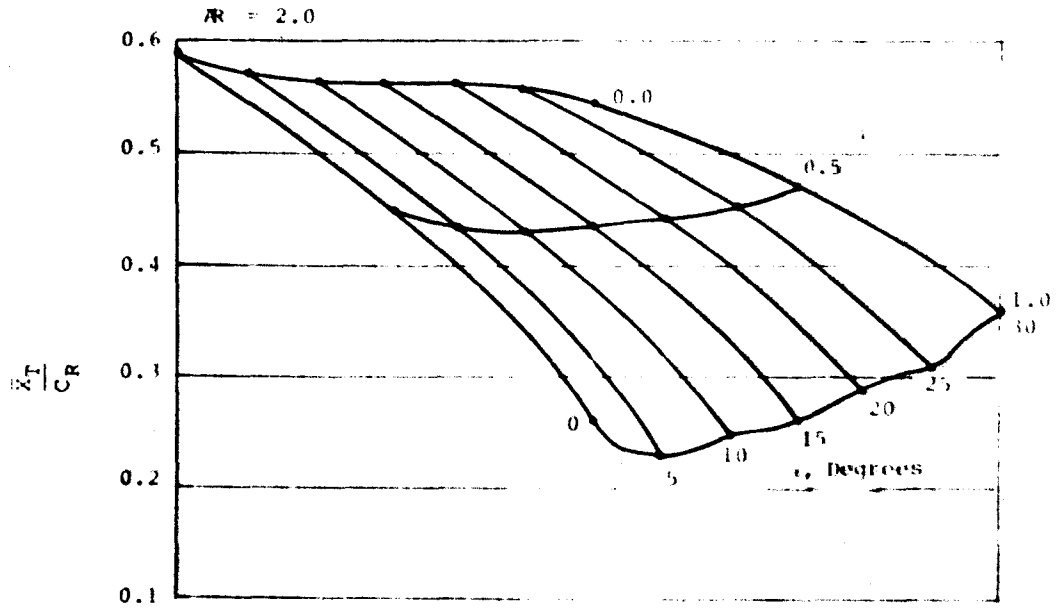


FIGURE 47(c). TAIL-ALONE CHORDWISE CENTER OF PRESSURE PREDICTION CURVE; $AR = 2.0$.

Description of Method

Linear theory predicts no variation in the center of pressure location with angle of attack. Fidler and Bateman (ref. 3) found a more satisfactory method for isolated tails at higher Mach numbers to be one based on the correlation of actual data. This type of method also was found to be more satisfactory for the incompressible flow case. Thus, the method consists of using the data correlation curves of figure 47 discussed earlier.

Use of Method

This section demonstrates the use of the method and makes comparisons with experimental data. The required physical characteristics of the tail are the following:

- Taper ratio
- Aspect ratio (based on complete symmetric planform)

In addition, it is assumed that the leading edge is rounded and the flow is incompressible.

General Description. For the particular combination of taper ratio and aspect ratio determine the variation of \bar{X}_T with angle of attack from the appropriate curve of figure 47. Use linear interpolation for aspect ratio effects.

Numerical Example I. This example compares the method with one of the cases in the present experimental study. This is done in order to show the self-consistency of the method. The case selected is tail T10.

$$\lambda = 0.5$$

$$AR = 0.5$$

From figure 47(a) (aspect ratio 0.5) determine \bar{X}_T as a function of angle of attack from the taper ratio 0.5 curve. This gives the following values.

α°	\bar{X}_T/C_R
0	0.3875
5	0.3975
10	0.4350

α°	\bar{X}_T/C_R
15	0.4650
20	0.4875
25	0.5000
30	0.5050

The comparison between prediction and data is shown in figure 48. As can be seen, agreement is excellent.

Numerical Example II. This example compares the method to data of Bartlett and Vidal (ref. 19) on round edge delta wings. Also, it demonstrates the procedure to be applied to determine the effect of aspect ratio.

$$\lambda = 0.0$$

$$AR = 1.5$$

Determine \bar{X}_T as a function of angle of attack from both figure 47(b), (AR = 1.0), and figure 47(c), (AR = 2.0). Then find $\bar{X}_T(\alpha)$ for an aspect ratio of 1.5 by interpolating between these values.

α°	\bar{X}_T/C_R (AR = 1.0)	\bar{X}_T/C_R (AR = 2.0)	\bar{X}_T/C_R (AR = 1.5)
0	0.6375	0.5875	0.6125
5	0.6375	0.5700	0.6038
10	0.6275	0.5650	0.5963
15	0.6250	0.5600	0.5925
20	0.6225	0.5600	0.5913
25	0.6225	0.5550	0.5888
30	0.6225	0.5425	0.5825

The predicted values are plotted in figure 49 with the experimental values. Agreement between prediction and experiment is seen to be excellent with center of pressure location predicted within 2 percent of the root chord throughout the angle of attack range.

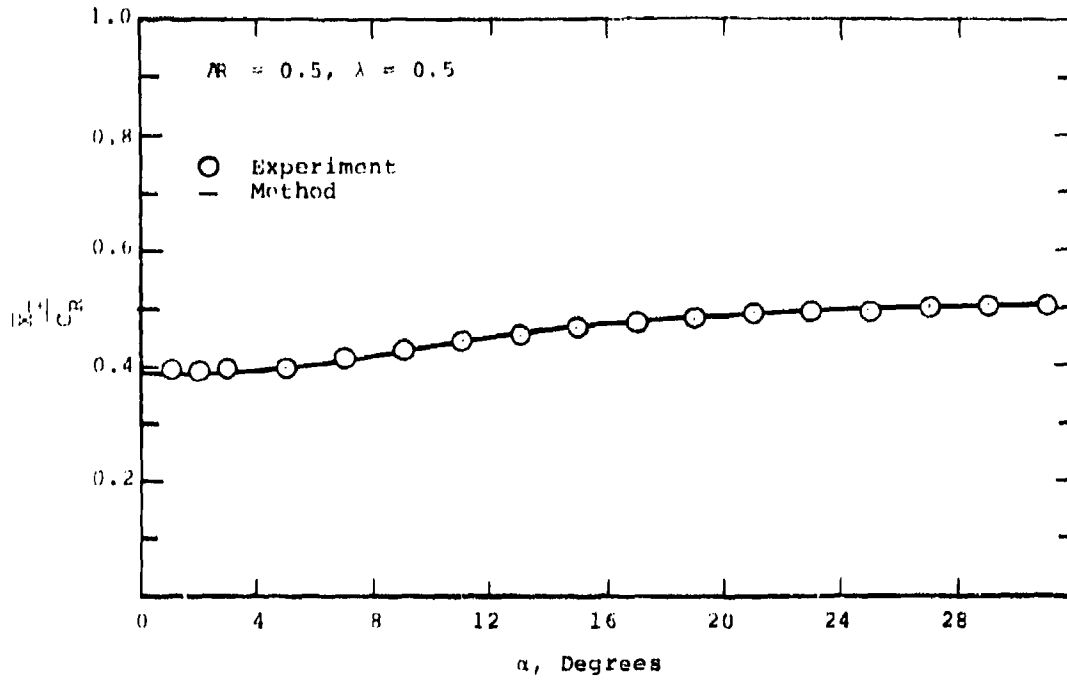


FIGURE 48. COMPARISON BETWEEN PREDICTED AND EXPERIMENTAL TAIL-ALONE CHORDWISE CENTER OF PRESSURE.

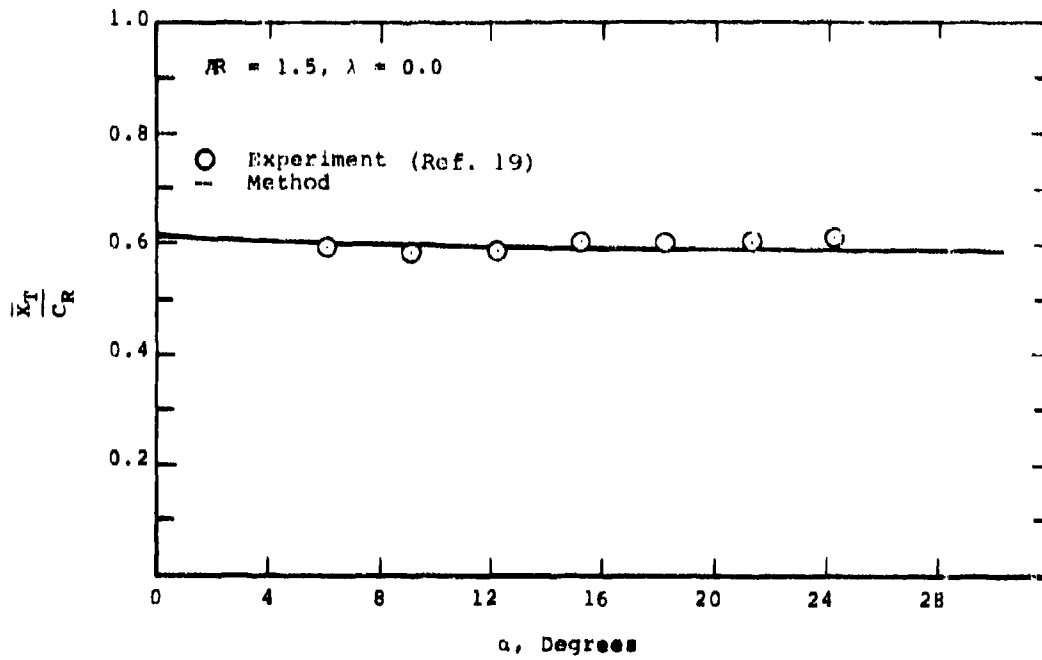


FIGURE 49. COMPARISON BETWEEN PREDICTED AND EXPERIMENTAL TAIL-ALONE CHORDWISE CENTER OF PRESSURE.

Figure 50 shows the results of an additional comparison for a delta wing of aspect ratio 2.0 and the data from several different experiments (refs. 19, 20 and 21). The predicted center of pressure is slightly upstream of the experimental values but still is within 2-1/2 percent of the root chord of the average experimental value.

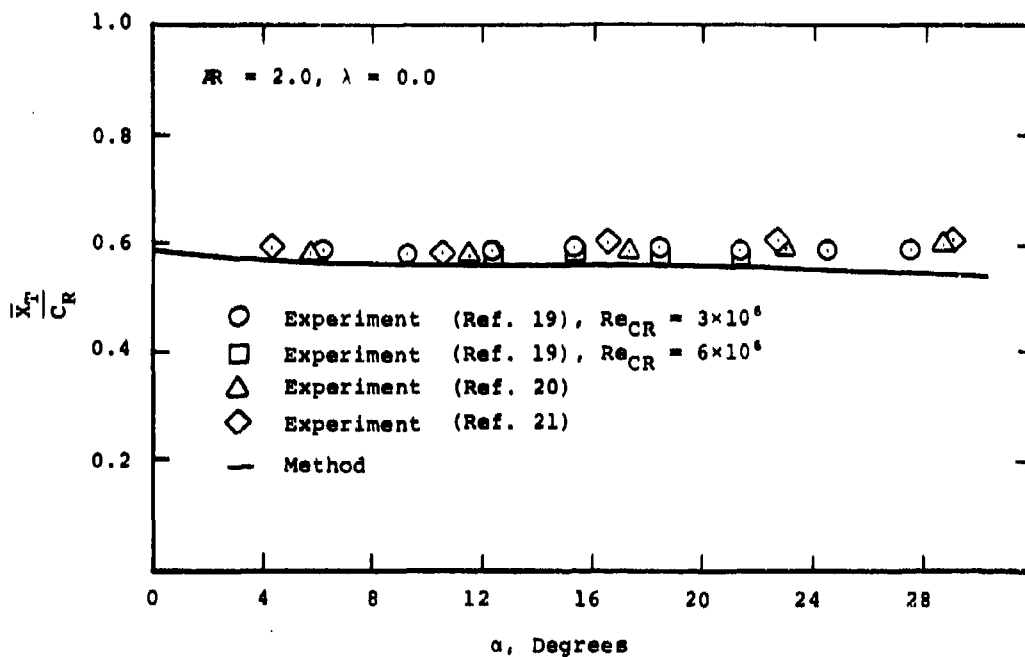


FIGURE 50. COMPARISON BETWEEN PREDICTED AND EXPERIMENTAL TAIL-ALONE CHORDWISE CENTER OF PRESSURE.

(Reverse Page 110 Blank)

VII. COMPLETE CONFIGURATIONS

VII.1 GENERAL CONSIDERATIONS

The flow field about a wing-body combination in a fluid stream is characterized by strong interactions between the body and the wings. Although the gross features of the flows around the separate components are largely the same as described in Sections V.1 and VI.1, significant distortions are introduced by mutual interferences. These discussions of complete configuration behavior should be read after those dealing with isolated bodies and tails. Separate discussions will be presented for the cases of low and high angles of attack respectively, beginning with the former.

At low angles of attack, the body base usually exhibits a thickened or separated axial boundary layer. A tail fixed to the base will be at least partially immersed in this highly-viscous, low energy flow. As a result, regions near the tail root will be subjected to reduced loading. It would be expected then that, relative to the isolated tail case, tail normal force would be reduced, while the spanwise center of pressure would move outboard. Since boundary layer thickness increases towards the rear of the tail, this region would be less highly loaded than the forward portion and the chordwise center of pressure would move upstream. All of these effects are found in the data to some extent.

The other major class of effects at low angles is usually taken to be due to the influence of "potential" flow upwash around the body. This often results in an effectively increased angle of attack on the tails, with correspondingly increased loading and an inward shift of the spanwise center of pressure. Although these effects are probably present in the low-angle data, the dominant influence seems to be that of the boundary layer, as discussed above.

At higher angles, separated crossflow boundary layer effects become important. Not only are there interactions

NCSC TM-238-78

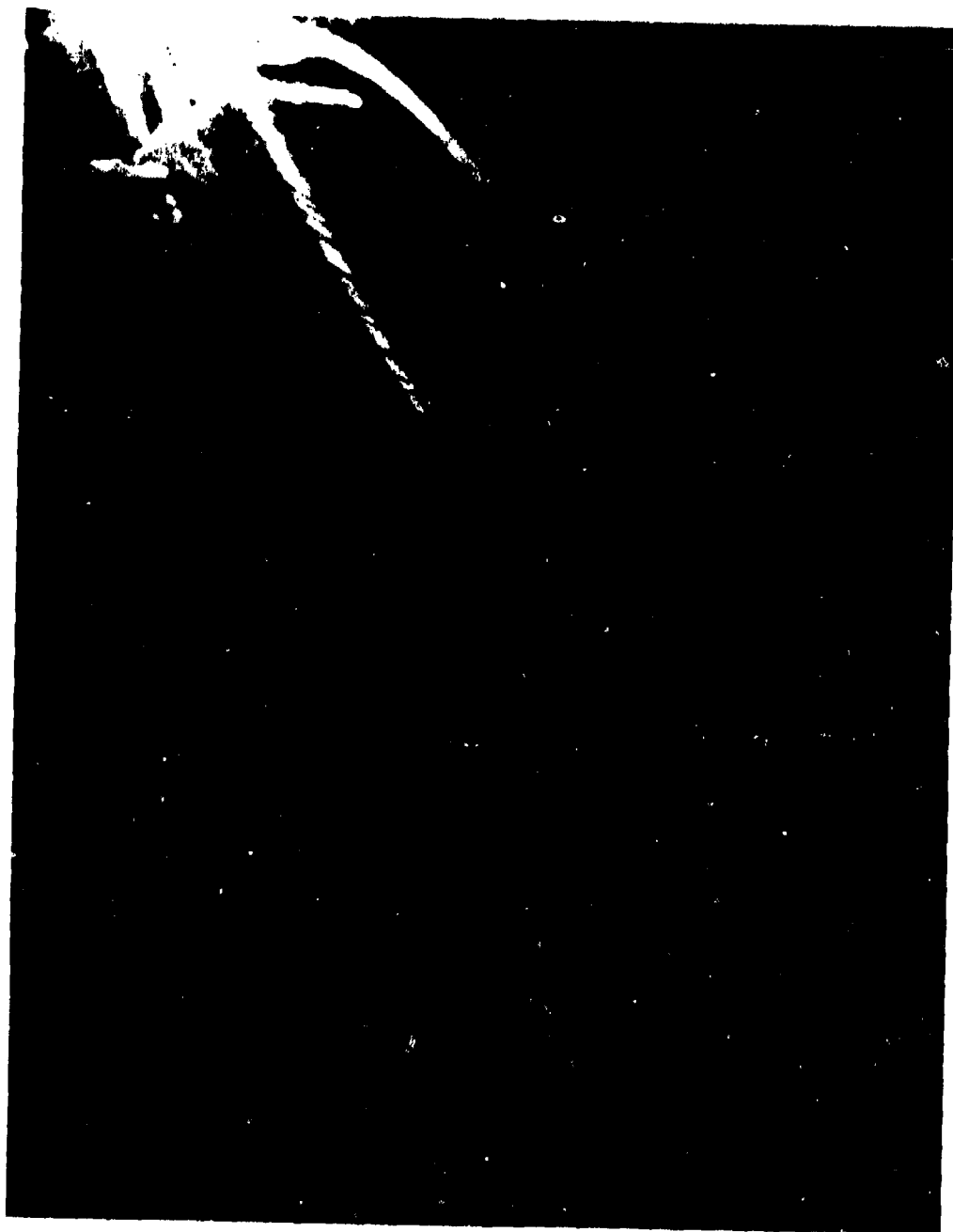


FIGURE 51. OIL FLOW PHOTOGRAPH OF TAIL/BODY JUNCTION.

between the lee-side vortices from the tails and the body: the presence of the tails "blanks off" a portion of the body crossflow, leading to further complicated interactive effects. The amplification of tail normal force becomes reduced by downwash due to the body vortices and complex flows are induced near the tail-body junction by separating and reattaching boundary layers. Figure 51 shows an oil-flow picture of the tail region on the lee-side of the configuration at 15° angle of attack. The complexity of the flow field is clearly shown. Note the downward direction of the streamlines on the body, caused by the lee-side vortex flow. The tail lee-side vortices can also be seen as can the complex interactive region near the tail root. This picture shows clearly the difficulties in attempting a theoretical treatment of such flows and the need for a semi-empirical approach.

VII.2 BODY CARRYOVER NORMAL-FORCE COEFFICIENT

This method permits calculation of the carryover loading on a body due to the presence of the lifting tails. The method is valid for angles of attack up to 15° , and is restricted to body-tail combinations at 0° sideslip. Application consists of first determining the carryover loading of a reference configuration and then correcting this value for effects of fin span, taper ratio and fin position.

When a body has tail panels fixed on either side, the lift on these panels induces a certain amount of lift on the body region lying between them. This lift, which is usually termed "carryover loading", can be estimated by linear theory (ref. 22). However, since the tail panels of the present configurations are located on a region of the body that is strongly influenced by viscous effects, linear theory was found to be inadequate for prediction of carryover loading.

The carryover lift usually acts in the same direction as that on the tails. A feature of the present data was the existence of carryover loading acting in both the same and opposite direction to the tail lift for the one caliber base. In the absence of a detailed examination of the nature of the carryover loading, which is beyond the scope of the present investigation, it is difficult to describe accurately the causes of the negative loading. The results of the flow visualization investigation did reveal the presence of large vortices on the one caliber base (which

showed negative loading) that were not evident on the two or three caliber bases. This could have led to the effect. In addition, the tail panels could have effectively blanked off a portion of the crossflow around the body, thus causing a viscous load reduction which would then appear as a negative carryover loading.

The carryover loading on the two and three caliber bases was essentially linear with angle of attack over the entire α range (0° to 15°). This is consistent with the solution from linear theory. However, because of the flow characteristics over the conical bases, the amount of carryover loading was found to vary with the location of the fin on the base, the fin taper ratio, and the fin span. Therefore, it was decided to base the method on a correlation of actual data to describe a function of the form

$$C_{N_B(T)} = C_{N_B(T)}(\alpha, r/s, \lambda, l_{LE}/d) \quad (38)$$

Description of Method

It is assumed that the effects of the various parameters in equation (38) are separable. This allows the equation to be rewritten as

$$C_{N_B(T)} = \left[C_{N_B(T)} \right]_0 \cdot f_1(r_0/s) \cdot f_2(\lambda) \cdot f_3(l_{LE}/d) \quad (39)$$

where $\left[C_{N_B(T)} \right]_0$ is the carryover-normal-force-curve for a reference configuration. The values of the parameters for the reference condition are

$$r_0/s = 0.583$$

$$\lambda = 0.5$$

$$l_{LE}/d = 0.00$$

where r_0 is the maximum radius of the body. The value of $\left[C_{N_B(T)} \right]_0$ is given in Figure 52 for each of the three bases tested.

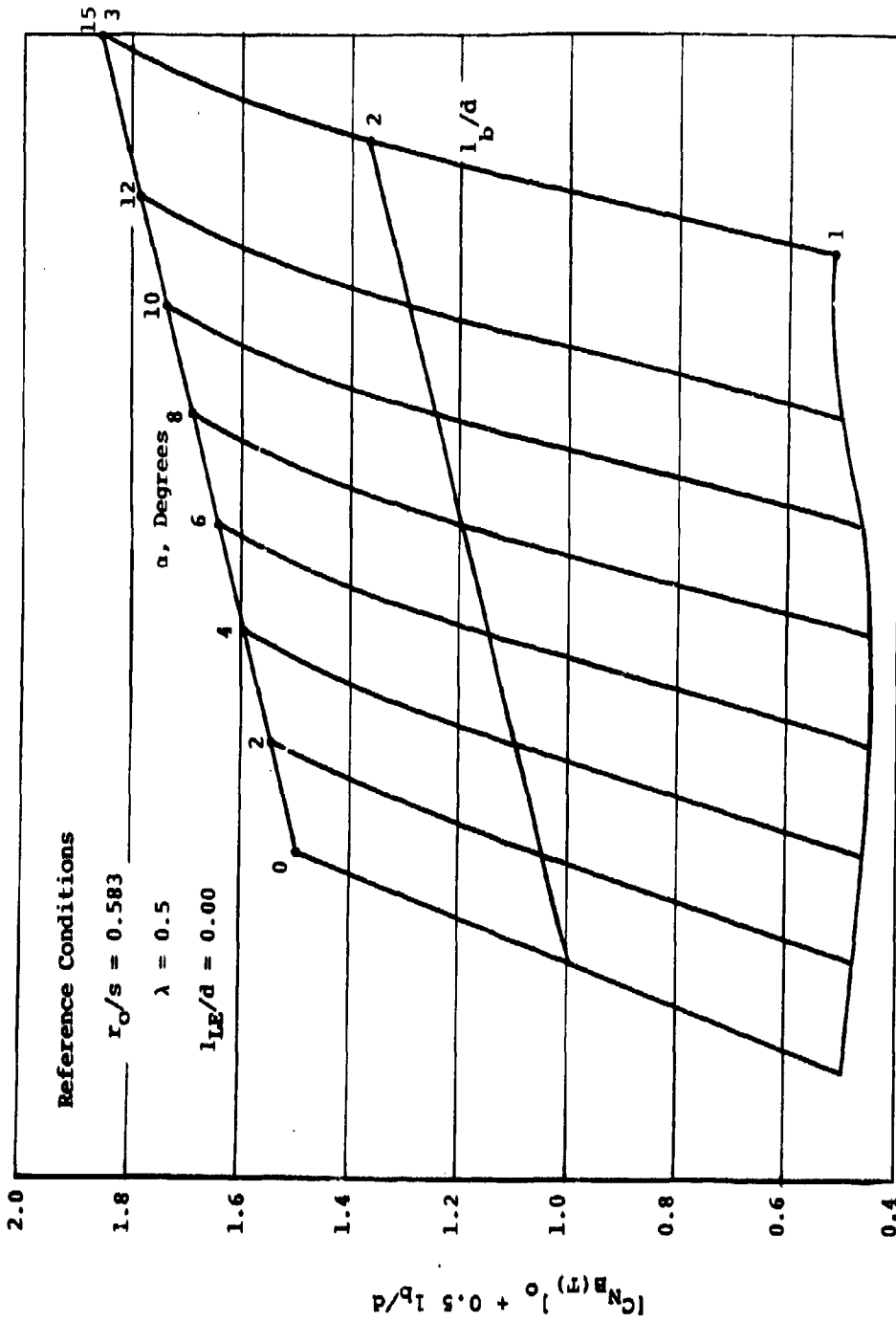


FIGURE 52. BASIC TERM FOR $C_{NB}(T)$.

To determine values for conditions other than the reference conditions above, $C_{N_B(T)}$ obtained from Figure 52 should be multiplied by the multiplicative correction factors for (1) effect of fin span from Figure 53, (2) effect of tail fin taper ratio from Figure 54, and (3) effect of fin position from Figure 55. In determining the ratio of body radius to fin semispan, r_0/s , the maximum body radius should be used.

Use of Method

To apply this method, the following values are required:

Fins

Exposed semispan, $b/2$

Taper ratio, λ

Body

Maximum body radius, r_0

Base length, l_b/d

Fin-Body

Axial distance of fin leading edge from start of base section, l_{LE}/d

The procedure to be followed is:

- 1) Given the base length, l_b/d , determine the basic term $\left[C_{N_B(T)} \right]_0$ from the appropriate curve of Figure 52.
- 2) Determine $r_0/s = r_0/(r_0 + b/2)$ and then find the multiplicative correction factor for fin span from Figure 53.
- 3) Find the correction factor for fin taper ratio from Figure 54.
- 4) Given l_{LE}/d , determine the correction factor for the effect of fin position.
- 5) Determine $C_{N_B(T)}$ from equation (39).

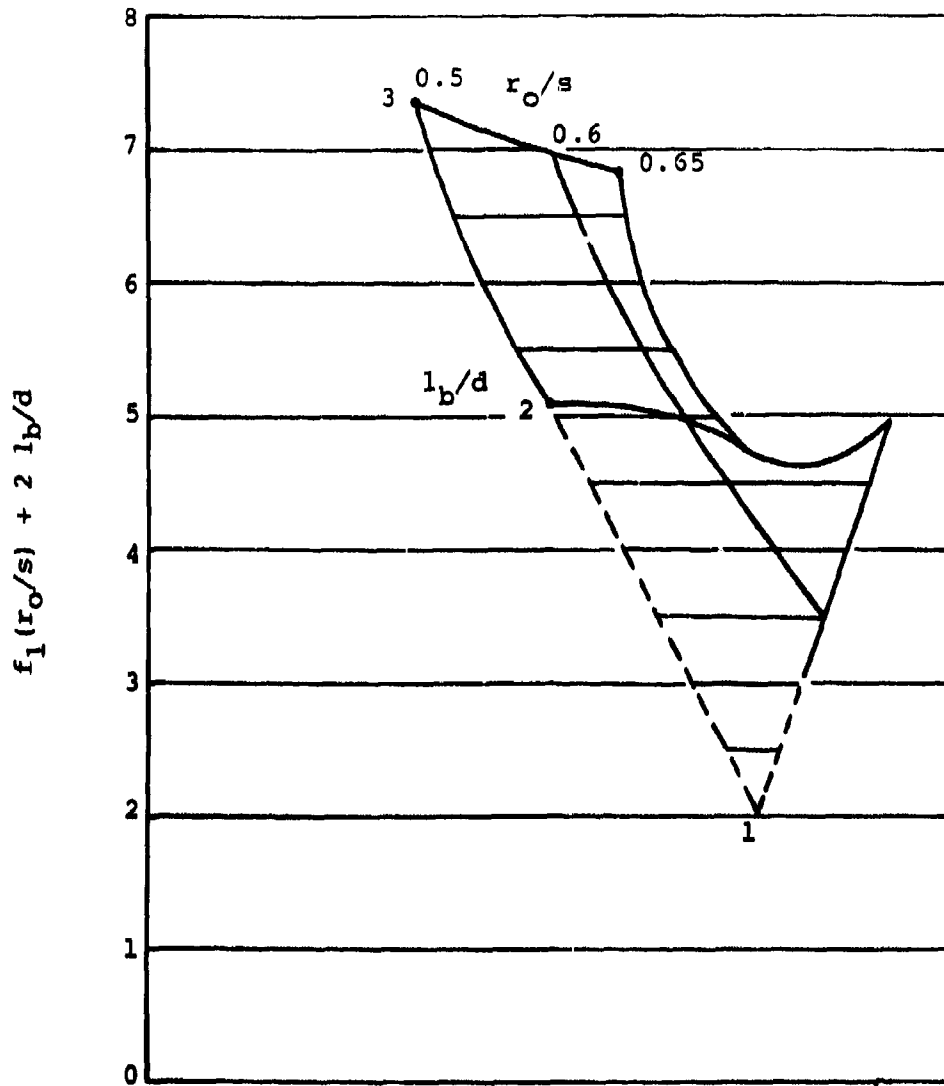


FIGURE 53. CORRECTION FOR EFFECT OF r/s .

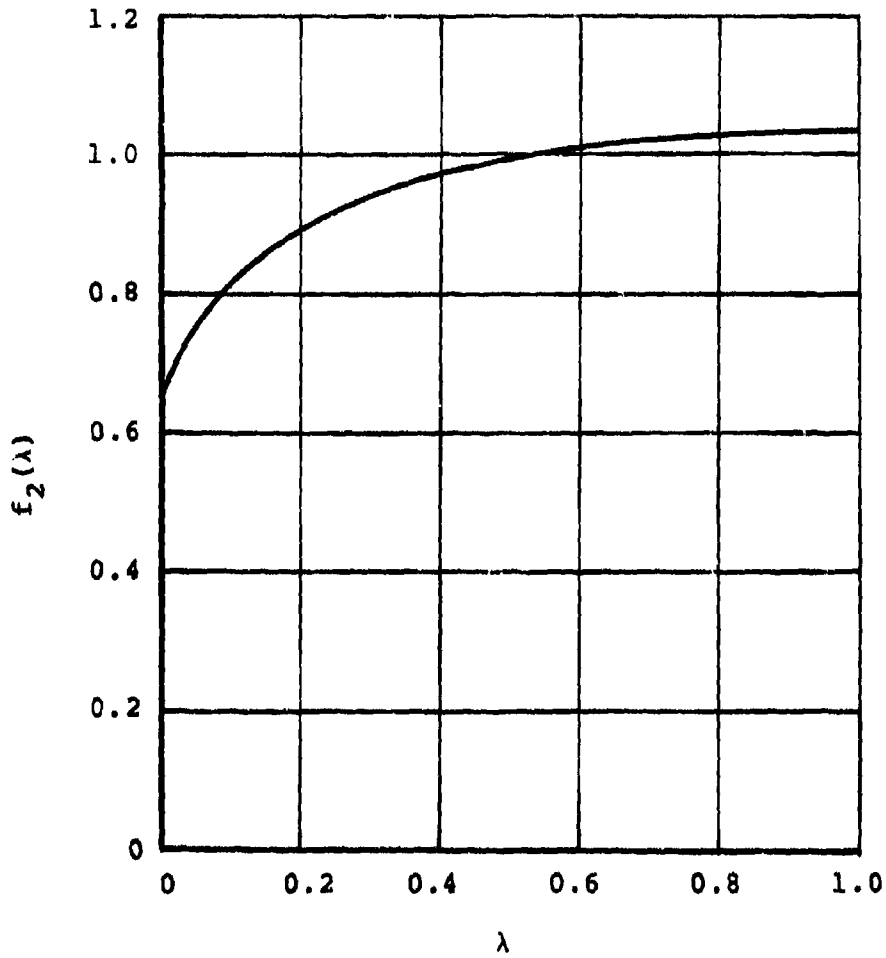


FIGURE 54. CORRECTION FOR EFFECT OF TAPER RATIO.

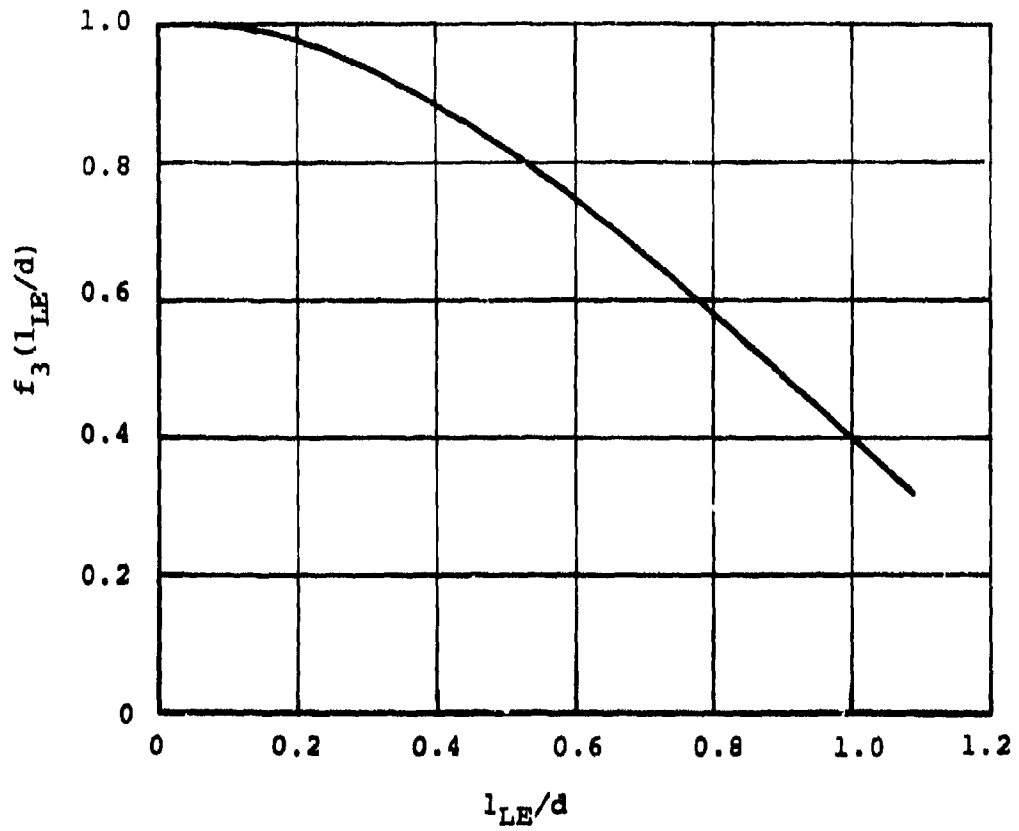


FIGURE 55. CORRECTION FOR EFFECT OF FIN POSITION.

No numerical example will be given at this stage. This will be postponed until a complete configuration is considered in Section VII.7.

VII.3 BODY CARRYOVER LOAD CENTER OF PRESSURE

The following method is used to estimate the center of pressure of the body carryover normal-force coefficient. This method is valid for models of the present type at angles of attack up to fifteen degrees. Examination of the data showed that, to a sufficient degree of accuracy, the centroid of the body planform area between the fins provided a suitable estimation of the center of pressure of $C_{NB(T)}$.

As discussed in Section VII.2, the lift on the tail panels induces a lift on the body region lying between these panels. This interference lift is termed "carryover loading". The center of pressure of this load then lies somewhere between the tail panels, i.e. in the shaded region of the body in Figure 56.

Experimentally, the center of pressure of $C_{NB(T)}$ is found by subtracting the moments due to the body-alone and the tail panels from the total moment and dividing by the carryover normal force, as in equation (40) below.

$$\frac{\bar{X}_N}{d} = \frac{1}{C_{NB(T)}} \left\{ C_{M_{BT}} - C_{M_B} - \left(C_{N_{T(B)2}} \frac{\bar{X}_{T(B)2}}{d} + C_{N_{T(B)4}} \frac{\bar{X}_{T(B)4}}{d} \right) \frac{S_T}{S_R} \right\} \quad (40)$$

Because of the method required to obtain \bar{X}_N , there can be quite a lot of scatter in the data. Thus, it was not possible to make a detailed examination of the effects of various parameters, such as fin taper ratio, etc., on \bar{X}_N .

Using a lifting-line potential flow model, Pitts, et al. (ref. 2) show that \bar{X}_N varied with aspect ratio, taper ratio, and the ratio of body radius to fin semispan. Due to data scatter it was not possible to check the application of that model to the present configurations. However, a convenient engineering method was derived that does provide

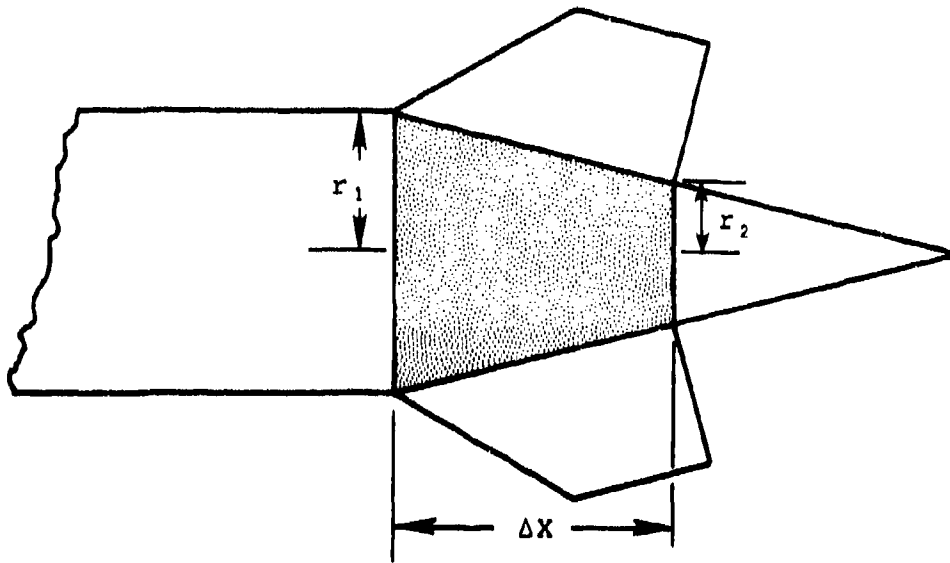


FIGURE 56. REGION OF CARRYOVER LOADING.

a suitably accurate estimate of \bar{X}_N for preliminary design purposes. This method is based on the assumption that the carryover loading on the body is uniformly distributed over the planform area of the body region lying between the tail panels. The center of pressure of the carryover loading is then simply the centroid of that planform area.

Description of Method

For a conical base, the planform area of the region of carryover loading is a trapezoid, as shown in Figure 56. The centroid of this region is given by

$$l_c = \frac{\Delta X}{3} \frac{2r_2 + r_1}{r_2 + r_1} \quad (41)$$

where ΔX is the axial length of the region, and l_c is measured from the upstream end of the region.

Use of Method

To apply this method, the body radii at the fin root-chord leading and trailing edges, and the axial extent of the root chord are required. These are then substituted into equation (41) to determine l_c , and hence \bar{X}_N . A numerical example will be postponed until a complete configuration is considered in Section VII.7.

VII.4 TAIL NORMAL-FORCE AMPLIFICATION FACTOR

This method permits calculation of the amplification of tail normal force when in the presence of the body. The method is valid for body-tail combinations of the present type in incompressible flow and for angles of attack up to 15° . From zero to 5° the amplification is constant. Beyond 5° it increases linearly.

The normal force on a horizontal fin fixed to a body is usually greater than that on an isolated fin at the same angle of attack due to the upwash around the body. Hence, the tail normal-force amplification, $R_{T(B)}$, expressed as

$$R_{T(B)} = \frac{C_{N_{T(B)}}}{C_{N_T}} \quad (42)$$

is expected to be greater than unity. For fins mounted on a body section of constant diameter, potential flow theory (see ref. 2) shows that the amplification is a function of the ratio of fin span to body radius and varies between one and two.

However, this concept assumes that the flow over the body has not separated. When this occurs, the value of $R_{T(B)}$ will depend upon how much of the fin is in separated flow. As shown earlier, the flow over the bodies in the present test did separate on the base section. The result was that the experimental tail normal-force amplification varied between values greater than one all the way down to zero.

In the latter case the fins are in what is essentially a completely separated flow and experience little or no force. This condition was often found for base B1 below an angle of attack of 5° . In general, $R_{T(B)}$ is constant from zero to 5° and then increases linearly. Thus, the amplification is of the form

$$R_{T(B)} = \begin{cases} R_0 & 0 \leq \alpha < 5^\circ \\ R_0 + R_1(\alpha) & 5^\circ < \alpha < 15^\circ \end{cases} \quad (43)$$

When compared to potential theory, the present values were always less due to a portion of the fins being in separated flow as described above. As a measure of comparison, the potential-flow relation (ref. 2) for fins mounted on a body of constant cross section can be used to determine the radius of such a body that would give the same amplification as in the present test. Since this relation gives a minimum amplification of 1.0, the equivalent slender body radius can be found only for experimental values of $R_{T(B)}$ greater than one. For these values, the equivalent radius was found to be 10-20 percent of the radius at the root-chord leading edge of the fins, and was approximately half the radius at the fin centroid. Thus, the tail normal-force amplification, for body-tail configurations used in the present test, is much less than predicted by linear flow theory due to flow separation.

The parameters affecting $R_{T(B)}$ include fin span/body diameter ratio, aspect ratio, taper ratio, Reynolds number based on maximum body diameter, base length, and the axial location of the fin on the base, in addition to the previously discussed dependence on the position of separation and the angle of attack. The effect of axial fin location of separation with respect to the fin and the effect of a change in body radius. Thus, the functional relationship for $R_{T(B)}$ is written

$$R_{T(B)} = R_{T(B)} \left(\frac{d}{b}, AR, \lambda, Re, \frac{l_b}{d}, \frac{LE}{d}, \alpha \right) \quad (44)$$

The method described in the next section was based on the data from the present test.

Description of Method

Based on evaluation of the data, the value of $R_{T(B)}$ is separated into two terms. The first is a constant and is the value of $R_{T(B)}$ from zero to 5° . This relationship is expressed quantitatively in equation (43). Each of the two terms, R_0 and R_1 , are determined by adding the incremental effects of aspect ratio, taper ratio, Reynolds number, and fin position, all for the particular base under study, to the value at a given span at given reference conditions. Thus, for instance, R_0 can be written as

$$R_0 = (R_0)_{d/b} + \Delta_{AR} R_0 + \Delta_{\lambda} R_0 + \Delta_{Re} R_0 + \Delta_{l_b} R_0 \quad (45)$$

The specified reference conditions, at which the first term was obtained, are

$$AR = 1.0$$

$$\lambda = 0.5$$

$$Re_d = 2.3 \times 10^6$$

$$\frac{l_{LE}}{d} = 0.0$$

The first term is determined from figure 57, for the particular values of fin span and base length. To this are added the effects of the other parameters, determined from figures 58 through 61. In figure 58, the small vertical mark at the end of each curve of constant l_b/d indicates

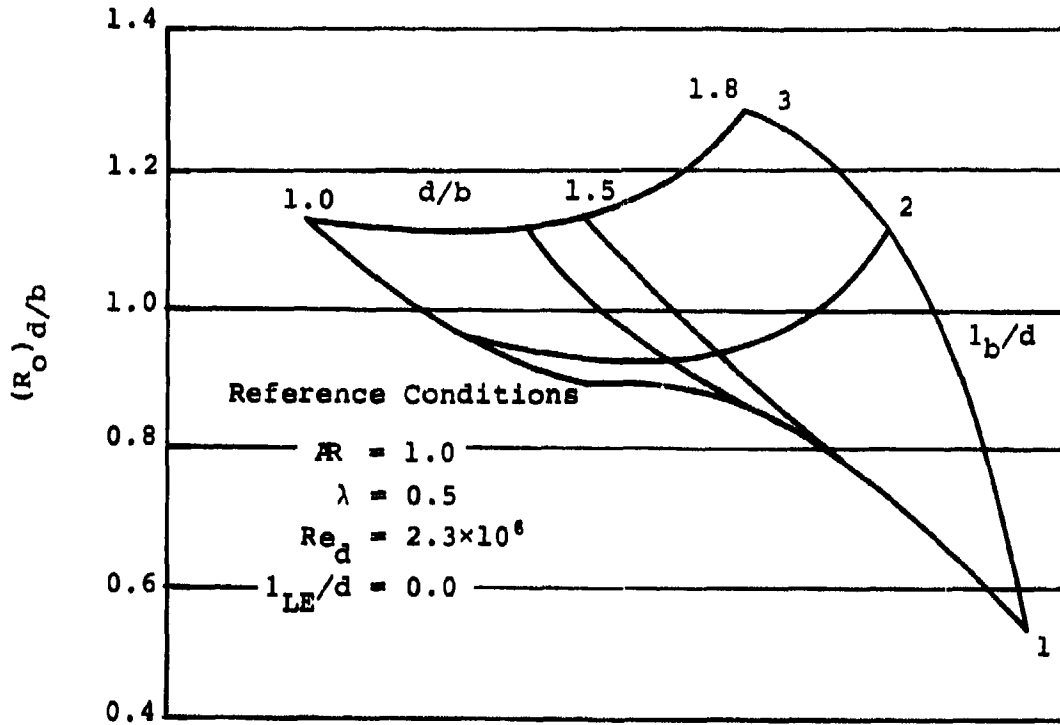


FIGURE 57. EFFECT OF FIN SPAN ON R_o .

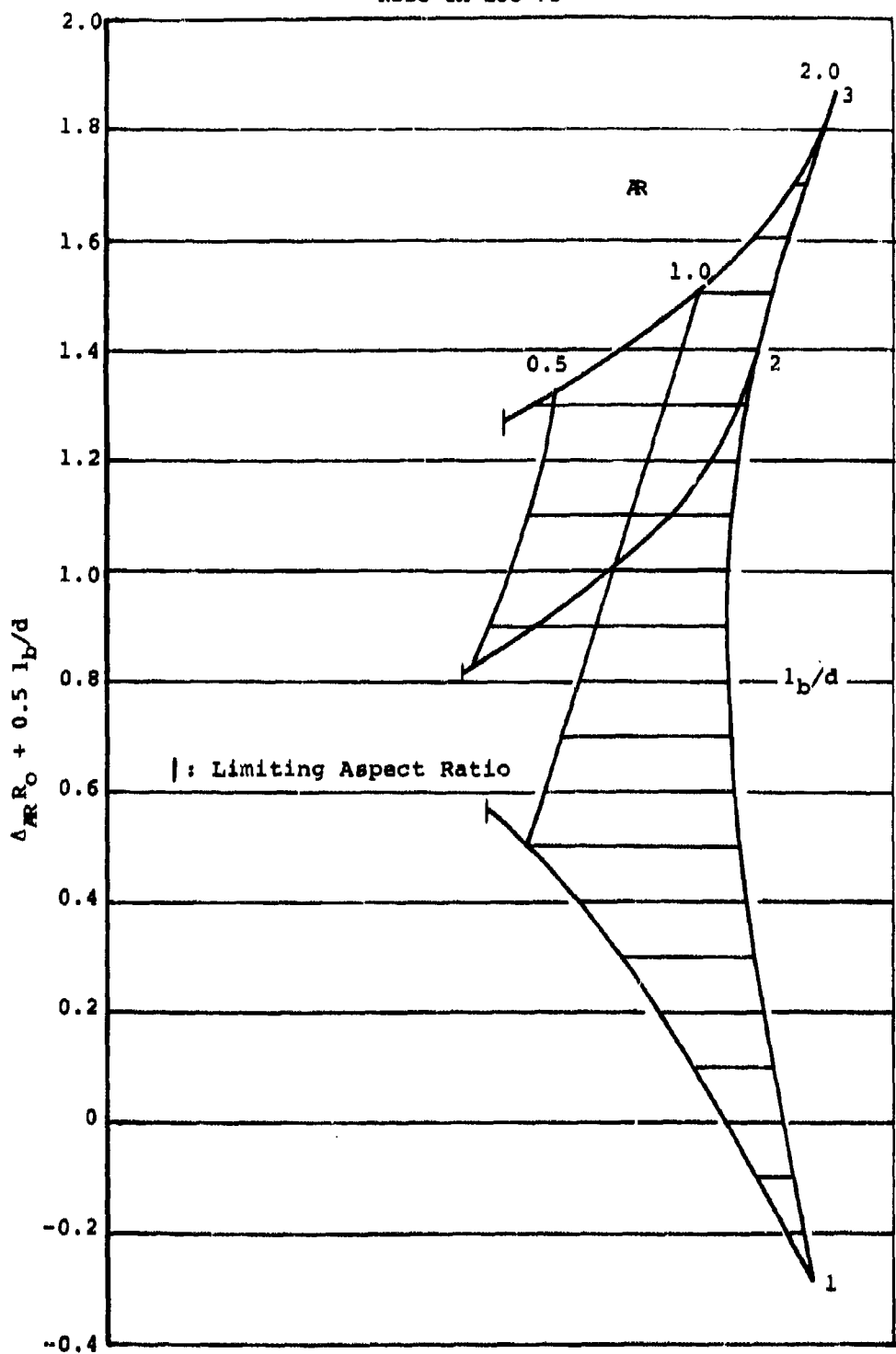


FIGURE 58. EFFECT OF ASPECT RATIO ON R_0 .

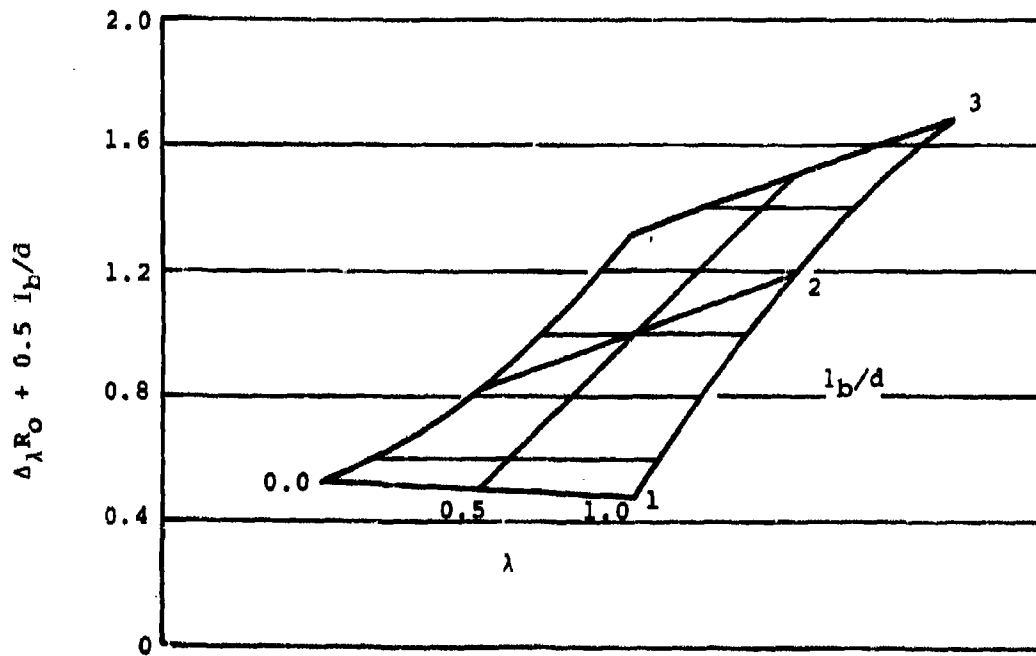


FIGURE 59. EFFECT OF TAPER RATIO ON R_o .

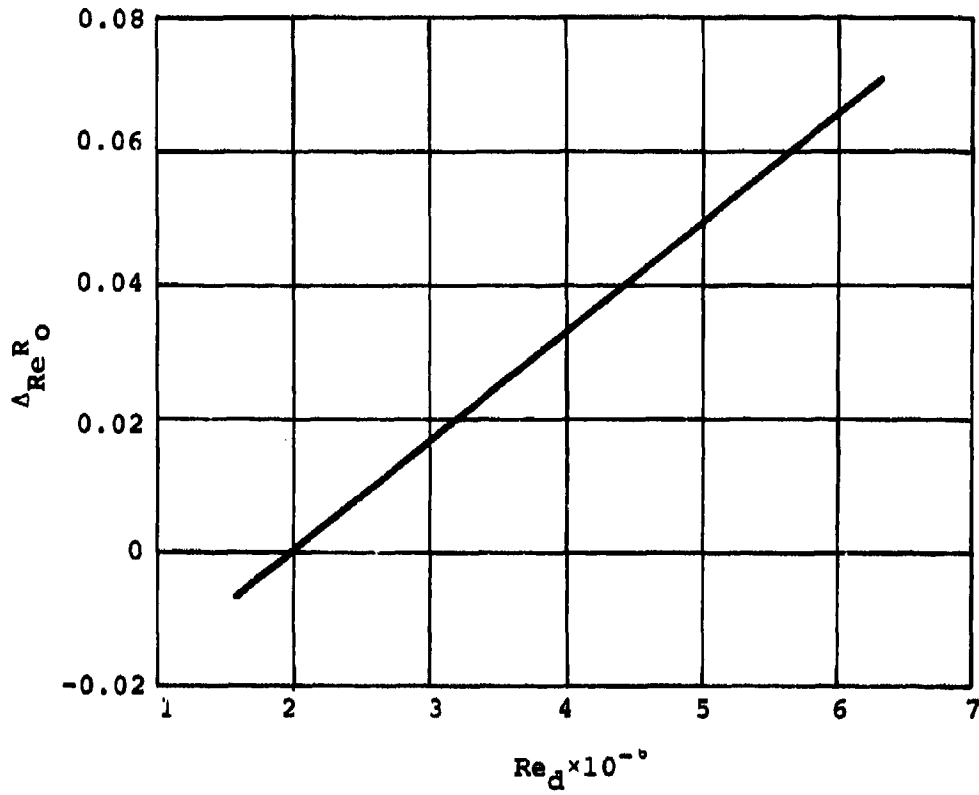


FIGURE 60. INCREMENTAL EFFECT OF REYNOLDS NUMBER ON R_o .

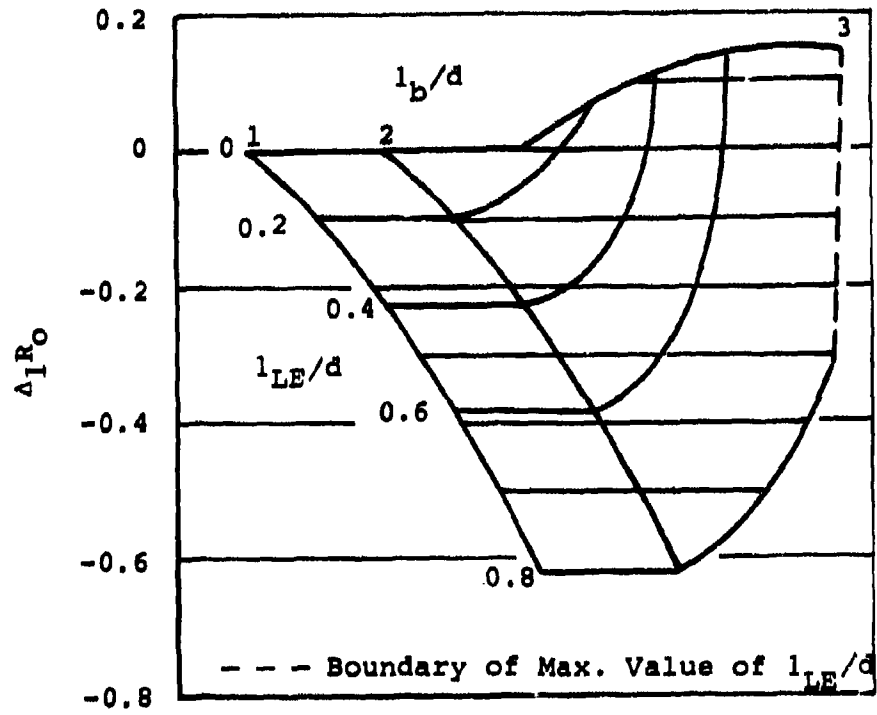


FIGURE 61. EFFECT OF FIN POSITION ON R_o .

the limiting aspect ratio for the reference conditions. Also, in figure 61, for the effect of fin position, the dashed line indicates that, for the given reference conditions, there is a maximum value of l_{LE}/d , beyond which the fin is no longer on the base.

The value of R_1 is determined in exactly the manner, starting with the initial term for the effect of fin span given in figure 62. The additional effects are determined from figures 63 through 66.

Use of Method

This section demonstrates the use of the method and makes comparisons with experimental data. The required physical characteristics of the body-tail combination are the following:

Fins

Aspect ratio, AR

Taper ratio, λ

Span, b

Body

Base length, l_b

Maximum body diameter, d

Reynolds number based on maximum body diameter, Re_d

Fin-Body

Position of fin root-chord leading edge from start of base section, l_{LE}

The procedure to be followed is:

- (1) Given the fin span and base length, determine $(R_0)_d/b$ from the appropriate curve of figure 57.
- (2) Determine the incremental effects of aspect ratio, taper ratio, Reynolds number, and fin position from figures 58, 59, 60 and 61, respectively.
- (3) Use equation (42) to determine R_0 .

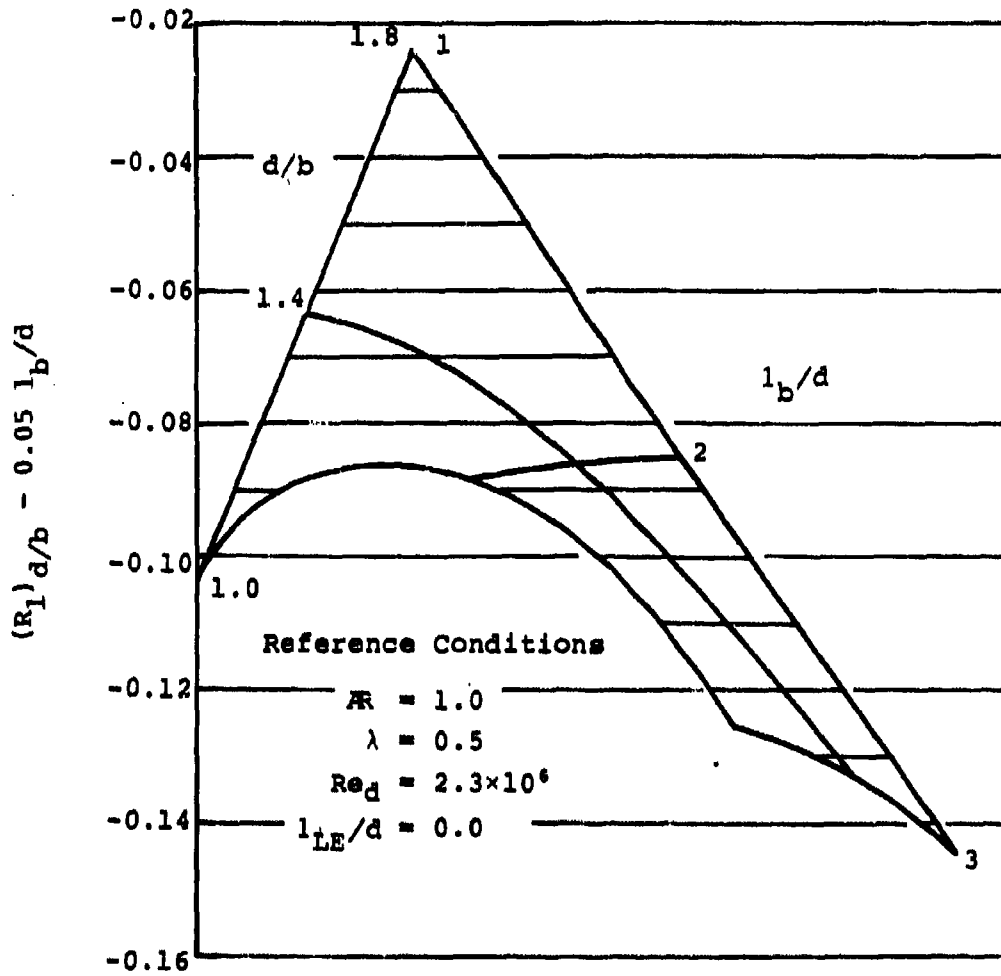


FIGURE 62. EFFECT OF FIN SPAN ON $R_T(B)$ SLOPE.

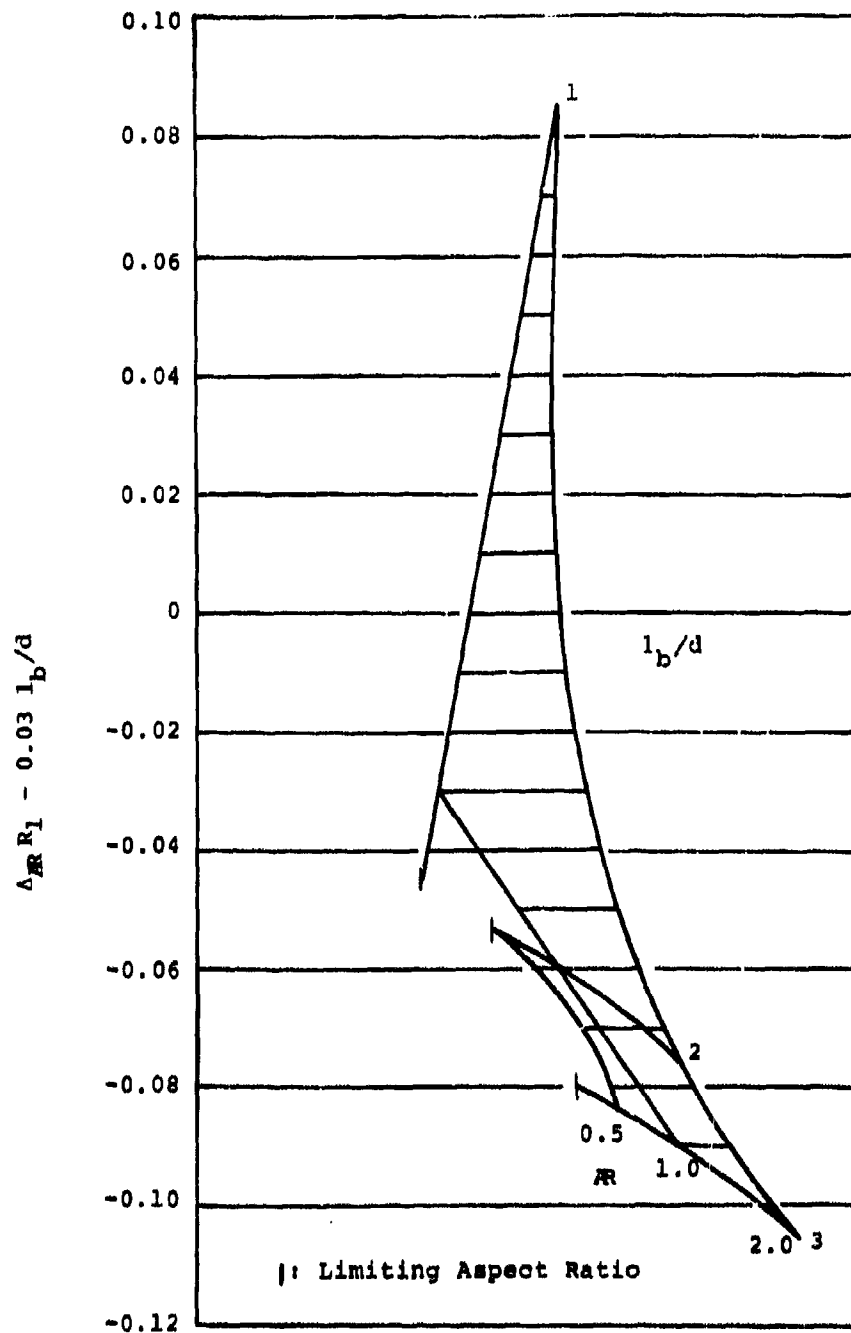


FIGURE 63. EFFECT OF ASPECT RATIO ON R_1 .

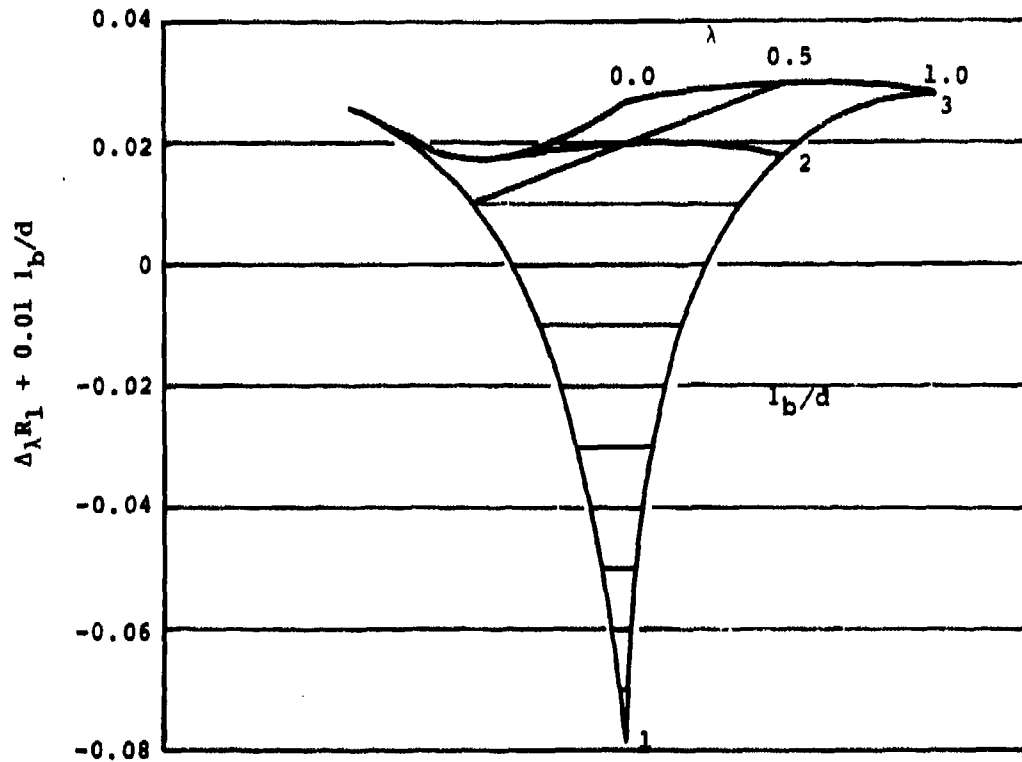


FIGURE 64. EFFECT OF TAPER RATIO ON R_1 .

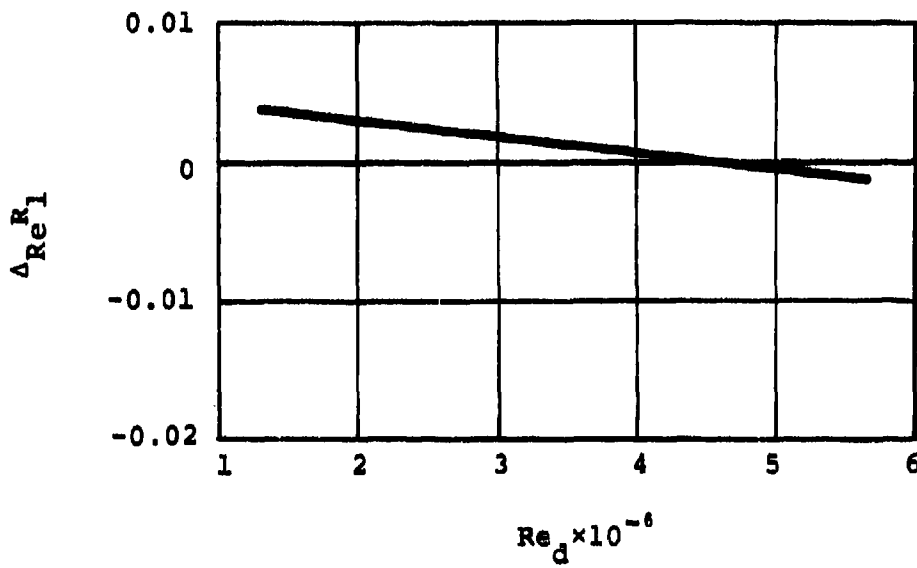


FIGURE 65. INCREMENTAL EFFECT OF REYNOLDS NUMBER ON R_1 .

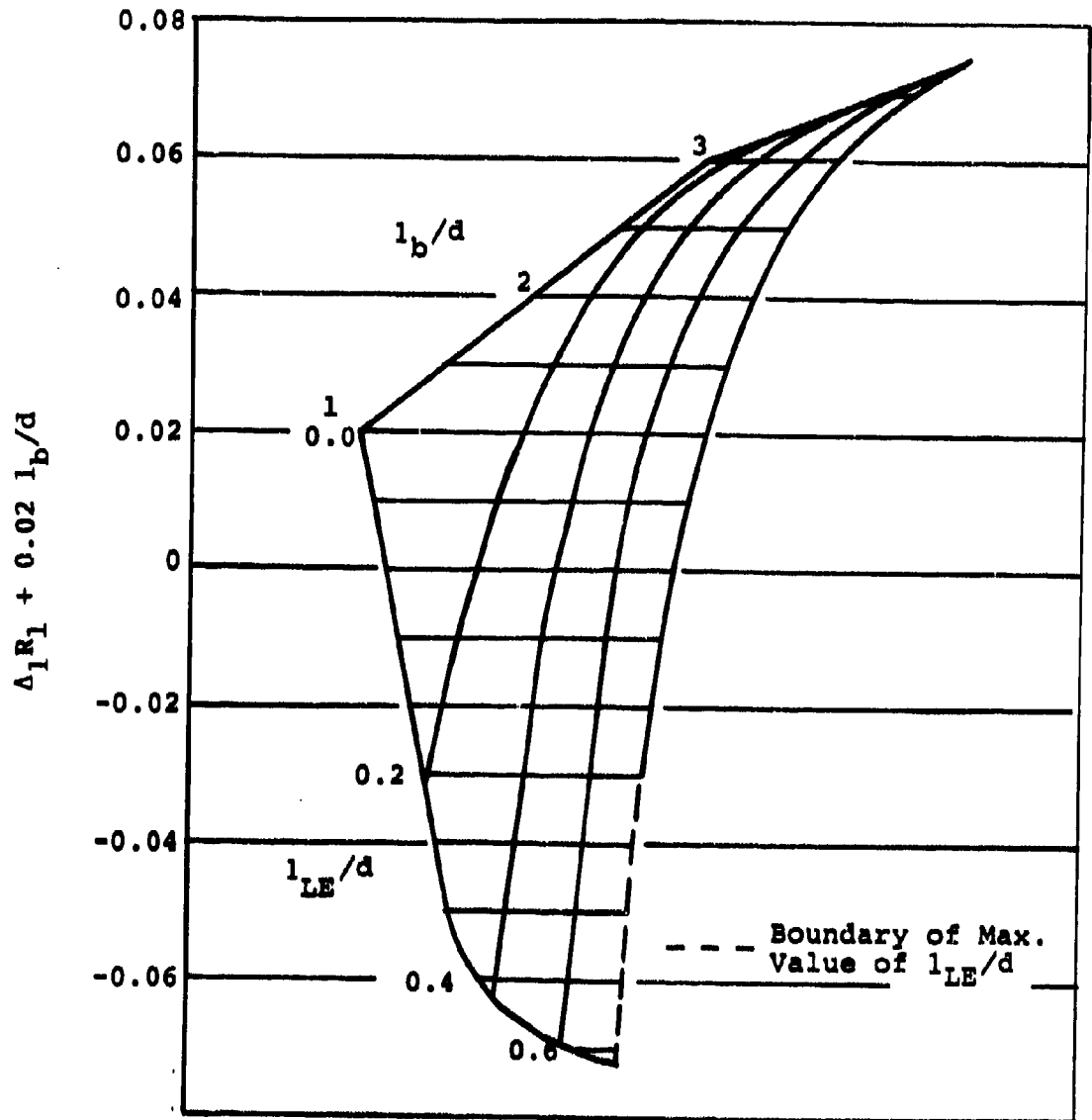


FIGURE 66. EFFECT OF FIN POSITION ON R_1 .

- (4) For the given values of fin span and base length, find the value of $(R_1)_{d/b}$ from the appropriate curve of figure 62.
- (5) As in step 2, find the incremental effects of aspect ratio, taper ratio, Reynolds number, and fin position from figures 63, 64, 65, and 66, respectively.
- (6) The slope, R_1 , is determined from the equation

$$R_1 = (R_1)_{d/b} + \Delta_{AR} R_1 + \Delta_{\lambda} R_1 + \Delta_{Re} R_1 + \Delta_1 R_1 \quad (46)$$

- (7) The value of $R_{T(B)}$ is given by equation (43), repeated here.

$$R_{T(B)} = \begin{cases} R_0 & , 0 \leq \alpha \leq 5^\circ \\ R_0 + R_1(\alpha) & , 5^\circ < \alpha \leq 15^\circ \end{cases}$$

Numerical Example. This example compares the method to data from the present test. The configuration chosen is N2C2B2T9_M at a free-stream Reynolds number of 2.3×10^6 , based on the maximum body diameter. The values of the required parameters are:

Fins

Aspect ratio: $AR = 2.0$
 Taper ratio: $\lambda = 0.0$
 Span: $b = 5.0$ in.

Body

Base length: $l_b = 14.0$ in.
 Maximum body diameter: $d = 7.0$ in.
 Reynolds number based on maximum body diameter:
 $Re_d = 2.3 \times 10^6$

Fin Body

Position of fin root-chord leading edge from start of base section: $l_{LE} = 0.0$ inch. A sketch of this configuration is given in figure 67.

(1) From figure 57, $(R_0)_{d/b} = 0.927$.

(2) From figures 58-61 the following values are obtained:

$$\Delta_{RR} R_0 = 0.37 \quad \text{from figure 58}$$

$$\Delta_{\lambda} R_0 = -0.18 \quad \text{from figure 59}$$

$$\Delta_{Re} R_0 = 0.00 \quad \text{from figure 60}$$

$$\Delta_1 R_0 = 0.00 \quad \text{from figure 61}$$

(3) Using equation (43), $R_0 = 1.1170$

(4) From figure 62, $(R_1)_{d/b} = 0.0135$

(5) Using figures 63-66, the following values are determined

$$\Delta_{RR} R_1 = -0.016 \quad \text{from figure 63}$$

$$\Delta_{\lambda} R_1 = 0.017 \quad \text{from figure 64}$$

$$\Delta_{Re} R_1 = 0.00 \quad \text{from figure 65}$$

$$\Delta_1 R_1 = 0.00 \quad \text{from figure 66}$$

(6) Using equation (46), R_1 has the value 0.0136 deg^{-1} . Thus, the value of $R_{T(B)}$ is

$$R_{T(B)} = \begin{cases} 1.117 & 0^\circ \leq \alpha \leq 5^\circ \\ 1.117 + 0.0136 |\alpha| & 5^\circ < \alpha \leq 15^\circ \end{cases} \quad (47)$$

This is compared to experimental data in figure 68. The value of R_0 is somewhat less than the experimental value and the value of R_1 is somewhat greater, but the overall agreement is quite good.

NCSC TM-238-78

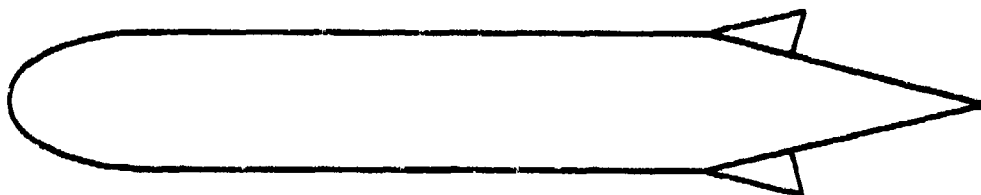


FIGURE 67. BODY-TAIL CONFIGURATION N2C2B2T9_M.

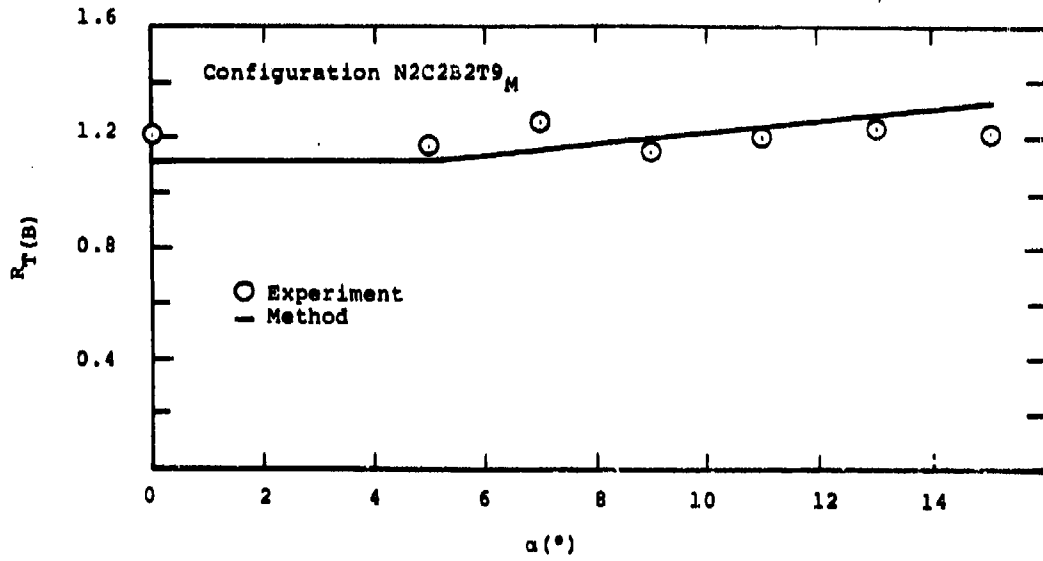


FIGURE 68. TAIL NORMAL-FORCE AMPLIFICATION COMPARISON.

VII.5 TAIL-ON-BODY CHORDWISE CENTER OF PRESSURE

This method permits estimation of the chordwise location of center of pressure on tail panels when mounted horizontally on bodies with conical bases. The method is valid for low-aspect-ratio panels with rounded leading edges and blunt trailing edges at body angles of attack up to 15° in incompressible flow. It is developed as a simple correction to the chordwise center of pressure on an isolated tail panel section VI.3. It is recommended that the method be used only for tails on conical bases of slenderness ratios greater than 1 caliber. A separate discussion is presented concerning the utility of tail panels mounted on a one caliber base.

As discussed in Section VI.3, a correlation of actual data for the center of pressure on isolated tails is a more satisfactory method than the various linear theories. This is found to be the case also for tails in the presence of the body. Results from linear theory, as described in reference 2, indicate very little difference in the location of the chordwise center of pressure for the isolated tail and the tail in the presence of the body. However, the data from the present test shows that $\bar{X}_{CP(B)}$ is slightly forward of \bar{X}_{CP} , the difference decreasing with increasing angle of attack. In previous sections the possibility and consequences of the existence of a thick boundary layer or a region of separated flow over the aft portion of the base near zero angle of attack has been discussed. If this type of flow was present, then the aft portion of the tail panels would be embedded in this separated flow. Then, the rear portion of the tail panels would generate reduced lift and the center of pressure would move forward, consistent with the present data.

Examination of the data revealed a consistent forward shift of $\bar{X}_{CP(B)}$ from the isolated tail data. This shift was a function of the angle of attack but was almost independent of model configuration. Hence, an accurate estimate of $\bar{X}_{CP(B)}$ could be determined by applying a simple correction to the estimate of \bar{X}_{CP} for the same tail. However, this is limited to tails mounted on the two and three caliber bases only.

Chordwise Center of Pressure of Tails Mounted on the One Caliber Base

The data for tail panels mounted on the one caliber base showed a tremendous amount of scatter, as can be seen

in figure 69. This prevented any correlation of the one caliber base data. Referring to the oil flow photograph in Section V.1, it is possible to understand the cause of this catter. The large vortices on the base greatly affected the loads, both on the base and on the tail panels. As was shown in Section VII.2, the result could be the almost total elimination of the tail normal force, indicating that the tail panels were completely embedded in separated flow. This does not provide a very desirable situation for vehicle control. Therefore, it is recommended that the one caliber base not be used unless specifically required. If its use is mandated then data from this test (not given here) should be used to estimate $\bar{X}_{T(B)}$.

Description of Method

The method involves applying a simple correction to the estimate for the tail-alone chordwise center of pressure, \bar{X}_T , for the same tail panel. Thus,

$$\bar{X}_{T(B)} = \bar{X}_T - \Delta\bar{X} \quad (48)$$

The variation of $\Delta\bar{X}$ with angle of attack is given in Figure 70. The proper value of \bar{X}_T should be determined by the method described in Section VI.3.

Use of Method

This section demonstrates the use of the method and makes comparisons with experimental data. The required physical parameters are the following:

Taper Ratio

Aspect Ratio (based on complete symmetric planform)

- (1) Determine the variation of \bar{X}_T with angle of attack from Section VI.3.
- (2) Apply the correction given in Figure 70 to determine $\bar{X}_{T(B)}$, using equation (48).

Numerical Example. This example compares the method to data from the present test. The configuration chosen is N2C2B2T12_M at a free-stream Reynolds number of 16.1×10^6 . The values of the required parameters are

Taper Ratio: $\lambda = 0.5$
Aspect Ratio: $AR = 2.0$

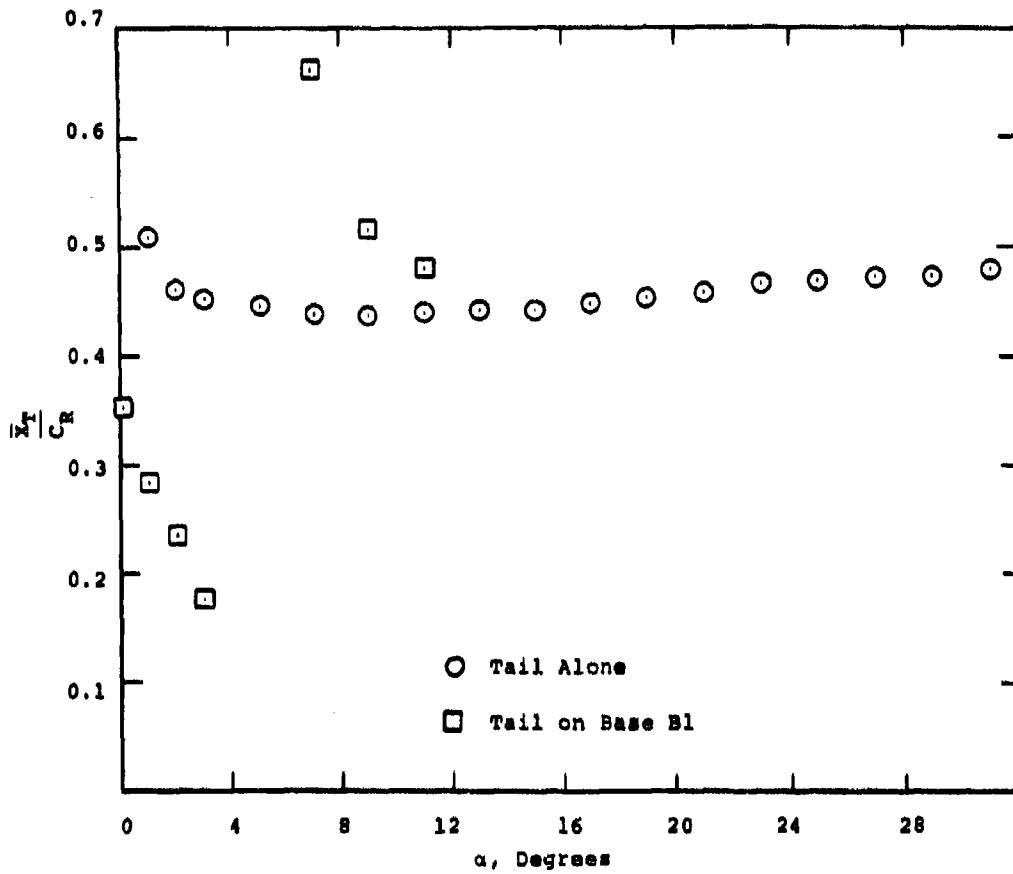


FIGURE 69. TAIL-ALONE CHORDWISE CENTER OF PRESSURE, BASE B1.

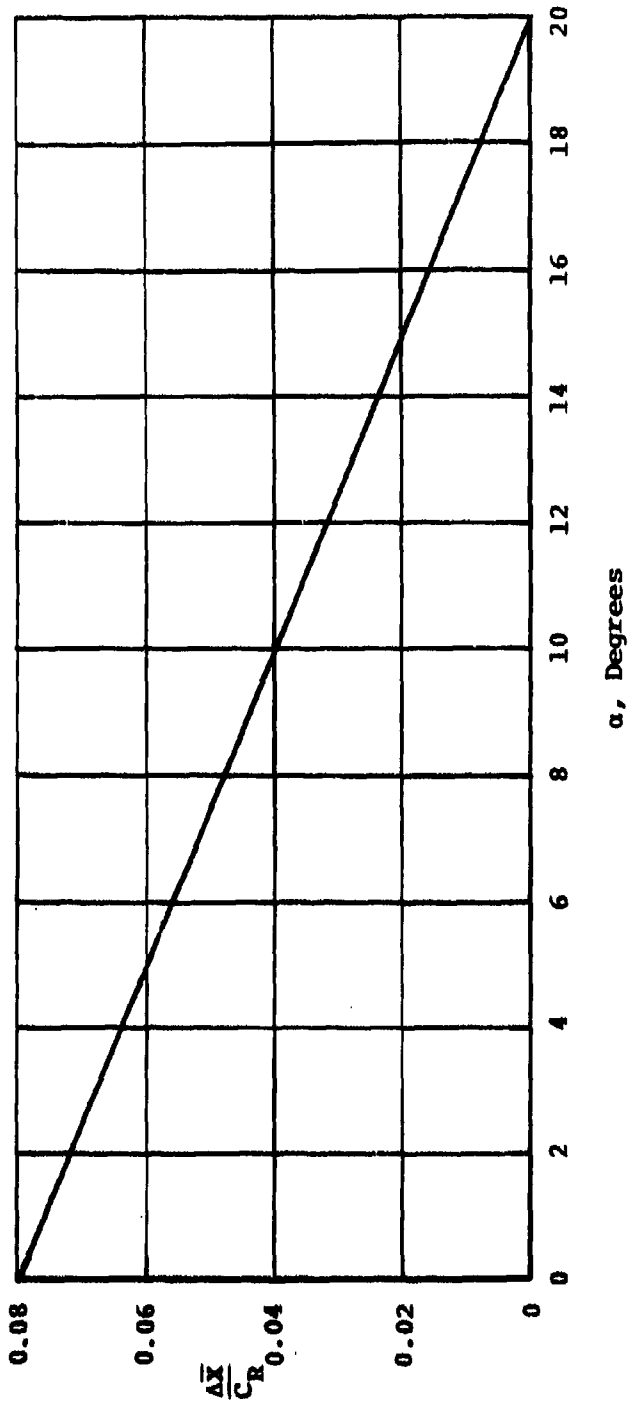


FIGURE 70. CORRECTION TO \bar{X}_T FOR DETERMINING $\bar{X}_{T(B)}$.

Using Figure 47(c) of Section VI.3 and Figure 70 of the present section the following values are obtained.

α°	\bar{x}_T/C_R	$\Delta\bar{x}/C_R$	$\bar{x}_{T(B)}/C_R$
0	.453	.08	.373
5	.435	.06	.375
10	.430	.04	.390
15	.435	.02	.415

These values are compared with experiment in Figure 71. The agreement is seen to be quite satisfactory.

VII.6 TAIL-ON-BODY SPANWISE CENTER OF PRESSURE

This method permits estimation of the spanwise location of center of pressure on tail panels mounted horizontally on bodies with conical bases. The method is based on strip theory and assumes a constant value of the section normal-force-curve slope along the span. It is found to be valid throughout the range of experimental values tested.

In contrast to the chordwise location of center of pressure (Section VII.5), the spanwise location is expected to be different for a tail panel in the presence of the body than for an isolated tail. The inner portions of the panels are in the accelerated flow around the body whereas the outer portions are in a flow that approaches free-stream conditions. Hence, the flow speed normal to the panel is not uniform along the span, being greater near the root chord. This results in an effectively greater angle of attack, and therefore, a correspondingly greater load, on the inner portion of the panel. The final result is that the spanwise location of center of pressure is inboard on a wing-body combination compared to an isolated wing. As the size of the body increases with respect to the tail semispan (increasing r/s), then, eventually, the entire panel becomes subjected to an essentially constant flow field and the spanwise center of pressure moves outboard again.

This concept has been expressed quantitatively in reference 23. Using strip theory, ignoring thickness effects, and assuming a constant section normal-force-

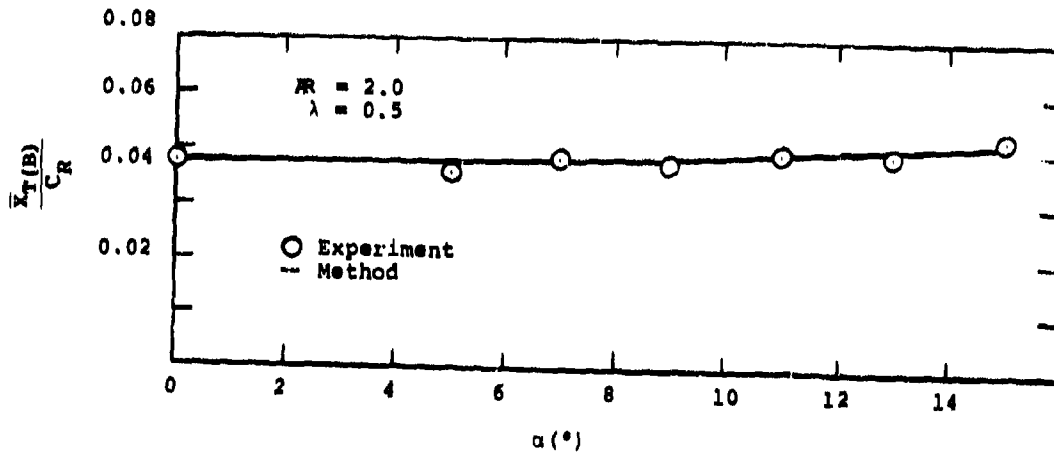


FIGURE 71. COMPARISON BETWEEN PREDICTED AND EXPERIMENTAL CHORDWISE CENTER OF PRESSURE OF TAIL.

curve slope, C_{n_α} , equal to that of a two-dimensional wing whose sweep is the same as that of the elemental strip, the total normal force on the lifting surface was found to be

$$NF = q C_{n_\alpha} \int_r^s \alpha_u Cy dy \quad (49)$$

where q is the dynamic pressure, α_u is the upwash angle, Cy is the chord length, and r is the body radius. The expression for α_u is

$$\alpha_u = (1 + r^2/y^2)\alpha \quad (50)$$

for an unrolled body, where α is the angle of attack of the body. Similarly, the rolling moment can be expressed as

$$RM = q C_{n_\alpha} \int_r^s \alpha_u Cy(y - r)dy \quad (51)$$

Carrying through the integrations and dividing the rolling moment by the normal force, the following expression is obtained for the spanwise center of pressure, measured from the root chord.

$$\begin{aligned} \frac{\bar{y}_{T(B)}}{b/2} = & \left\{ \frac{\lambda}{2} (1 - r/s) + \frac{1 - \lambda}{1 - r/s} \frac{1 - 2r/s - 11(r/s)^2}{6} \right. \\ & + \left[\left(\frac{1 + r/s}{1 - r/s} \right) (r/s)^2 \ln \frac{s}{r} \right] \\ & + \lambda (r/s)^2 \left[\frac{1}{1 - r/s} \ln \frac{s}{r} - 1 \right] \left. \right\} \\ & + \left\{ \lambda \left[1 - (r/s)^2 \right] + (1 - \lambda) \right. \\ & \left. \left[\frac{1 + r/s}{2} - \frac{(r/s)^2}{1 - r/s} \ln \frac{s}{r} \right] \right\} \quad (52) \end{aligned}$$

where λ is the fin taper ratio and $b/2$ is the semispan of the exposed fin. This relation is shown graphically in Figure 72, taken from reference 23, for three values of λ .

Description of Method

When equation (52) was compared with data from the present test the agreement was found to be quite satisfactory. In reference 23 agreement with data in transonic flow was also seen to be very satisfactory. Thus, this theory seems to apply over a wide range of flow conditions.

In the case of tails mounted on conical bases, the appropriate value of body radius must be determined. A brief study of various radii (such as at the mid point of the root chord) was conducted. However, Figure 72 shows that $\bar{Y}_T(B)$ is relatively insensitive to the body radius. This means that when applied to bodies of the present type, the most convenient radius can be used. The radius at the leading edge of the root chord is very convenient to determine and yields quite good results. Thus, this radius is recommended in the use of this method.

Use of Method

This section demonstrates the use of the method and makes comparison with experimental data. The required physical parameters are the following:

Body radius at root-chord leading edge of fin, r_{LE}

Semispan of fin, s

Fin taper ratio, λ

- (1) Determine ratio of body radius at root-chord leading edge of fin to fin semispan, r/s .
- (2) Find $\bar{Y}_T(B)$ as a fraction of exposed semispan from the appropriate curve of Figure 72.

Numerical Example. This example compares the method to data from the present test. The configuration chosen is N2C2B2T8_A at a free-stream Reynolds number of 16.1×10^6 . The values of the required parameters are:

Body radius at root-chord leading edge of fin:

$$r_{LE} = 3.5 \text{ in.}$$

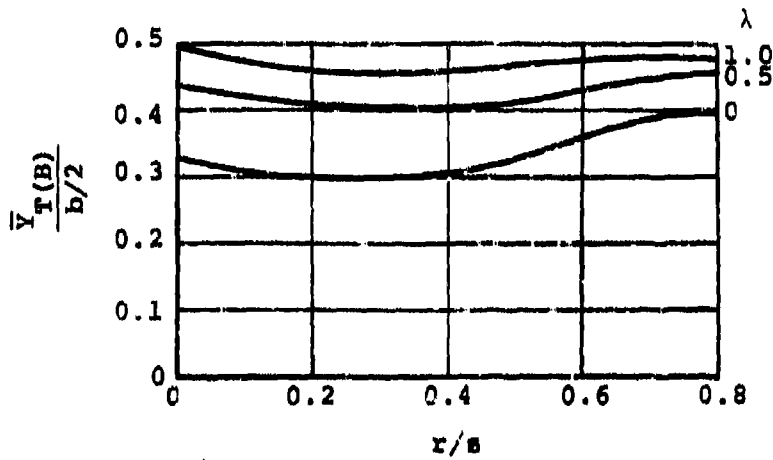


FIGURE 72. SPANWISE CENTER OF PRESSURE (REF. 23).

Semispan of fin: $s = 6.0$ in.

Taper ratio: $\lambda = 0.0$

- (1) The body radius to fin semispan ratio is

$$r_{LE}/s = 0.583$$

- (2) From the lower curve of Figure 72 ($\lambda = 0$), the value of $\bar{Y}_{T(B)}/b/2$ is 0.35.

This value is compared with the experimental values in Figure 73. Agreement is quite good. Additional comparisons are given in Figure 74 for the configuration N2C2B2T12 with fins mounted in the forward (Figure 74a), mid (74b), and aft (74c) positions. The agreement is seen to be very good in all cases.

VII.7 USE OF METHODS TO PREDICT COMPLETE CONFIGURATION CHARACTERISTICS

In this section the previously developed methods are combined to determine the total body-tail normal-force coefficient and pitching-moment coefficient for several complete configurations. The individual methods are worked out in detail for one configuration which then serves as an overall example for analysis of others.

Detailed Numerical Example

The configuration chosen for detailed analysis is N2C2B2T11_M at a free-stream Reynolds number of 16.38×10^6 . The components of this configuration are, in a sense, a geometric average of all the components tested.

Although only the total normal force coefficient and pitching moment coefficient will be compared with data in this section, all forces and moments for which a method exists, will be computed in detail. This then serves as a complete example of applying all the methods developed in the previous sections.

Values of Required Parameters

Fin

$$AR = 1.0$$

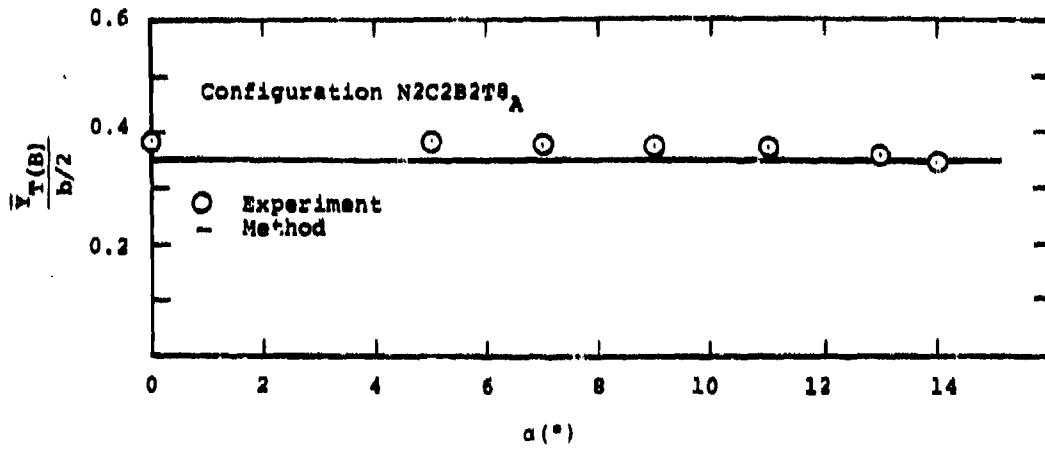


FIGURE 73. COMPARISON BETWEEN PREDICTED AND EXPERIMENTAL SPANWISE CENTER OF PRESSURE OF TAIL.

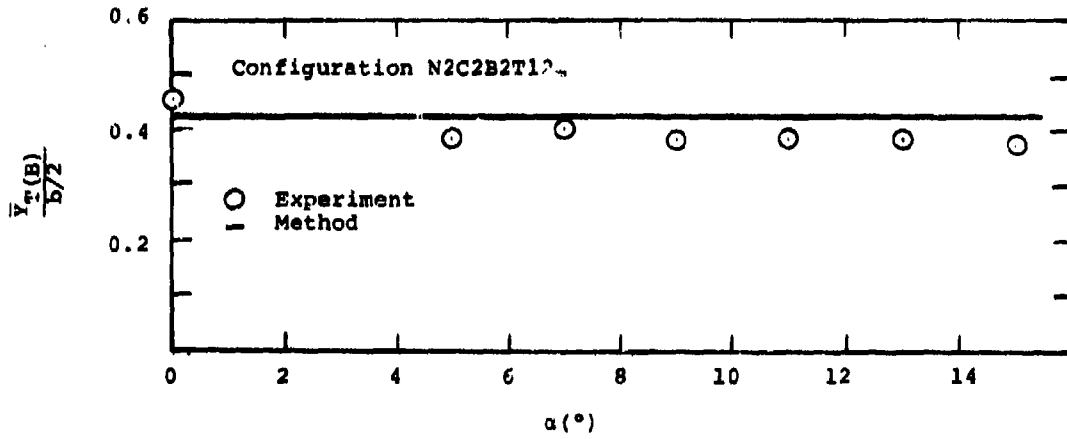


FIGURE 74(a). COMPARISON BETWEEN PREDICTED AND EXPERIMENTAL SPANWISE CENTER OF PRESSURE OF TAIL.

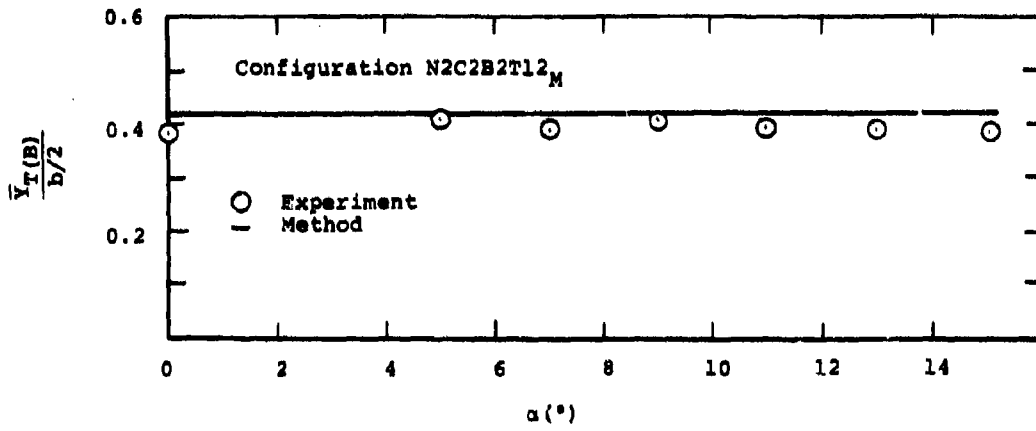


FIGURE 74(b). COMPARISON BETWEEN PREDICTED AND EXPERIMENTAL SPANWISE CENTER OF PRESSURE OF TAIL.

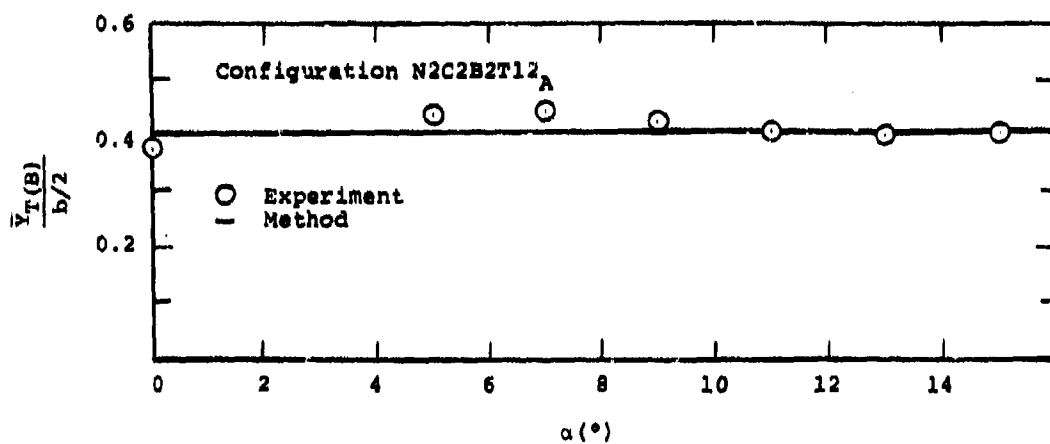


FIGURE 74(a). COMPARISON BETWEEN PREDICTED AND EXPERIMENTAL SPANWISE CENTER OF PRESSURE OF TAIL.

$$\lambda = 0.5$$

Shape of trailing edge: Blunt

$$Re_{CR} = 2.23 \times 10^6$$

$$b/2 = 2.5 \text{ in.}$$

$$C_R = 6.664 \text{ in.}$$

Body

$$l_P/d = 5.0$$

$r(x)$:

Nose	$r(x) = \left\{ \frac{d^2}{4} - \frac{(x-d)^2}{4} \right\}^{1/2}$	$0 \leq x \leq d$
Center	$r(x) = d/2$	$d < x \leq 5d$
Base	$r(x) = \frac{d}{2} \left[1 - \frac{(x-5d)}{2d} \right]$	$5d < x \leq 7d$
Max. body diameter	$d = 7 \text{ in.}$	

$S(x)$:

Nose	$S(x) = \frac{\pi}{4} [d^2 - (x-d)^2]$	$0 \leq x \leq d$
Center	$S(x) = \pi d^2/4$	$d < x \leq 5d$
Base	$S(x) = \frac{\pi d^2}{4} \left[1 - \frac{(x-5d)}{2d} \right]^2$	$5d < x \leq 7d$

Position of moment

reference center: $X_M = 30.5 \text{ in.}$

Length of body $X_B = 49.0 \text{ in.}$

$$l_P/d = 2.0$$

$$l_{sa}/d = l_P/d + \frac{x_{sa}}{d} = 5.910$$

$$S_w = 5.9643 \text{ ft}^2$$

$$Re_{sa} = 13.83 \times 10^6$$

$$l_c/d = 4$$

$$S_R = 0.2673 \text{ ft}^2$$

Fin-Body

$$l_{LE}/d = 0.00$$

Application of Methods

C_{N_T} (Section VI.2)

From figure 40 $C_{N_\alpha} = 1.570 \text{ rad}^{-1}$

From figure 41 $a_2 = 0.657 \text{ rad}^{-2}$

The tail-alone normal-force coefficient is now determined from equation (33), given below.

$$C_{N_T} = C_{N_\alpha} \cdot \alpha + a_2 \cdot \alpha^2$$

The results are tabulated in Table II.

\bar{X}_T (Section VI.3)

The tail-alone chordwise center of pressure is determined from figure 47(b) and the results are tabulated in Table II.

C_{N_B} (Section V.2)

(1) From figure 17, $x_{sa}/l_b = 0.455$.

(2) The equation for the diameter of a cone two calibers in length is

$$d_x = d \left(1 - \frac{x}{d}\right)$$

where d is the diameter of the base of the cone.
Thus $d_b = 3.815 \text{ in.}$ and $d_b/d = 0.545$.

(3) From equation (13), $C_{N_\alpha} = 0.594 \text{ per radian.}$

(4) Use $C_{N_{pot}} = C_{N_\alpha} \alpha$ to find potential force as a function of angle of attack.

(5) Determine x_{sc} from equation (14) for the angles of attack listed in Table II.

(6) Calculate the planform area from each x_{sc} in step (5) to the end of the body.

TABLE II

PREDICTED COMPLETE CONFIGURATION CHARACTERISTICS

Configuration NXC2B2T11_M Re = 16.38 × 10⁵

α	C_{M_T}	$\frac{\bar{X}_T}{C_R}$	C_{A_B}	C_{N_B}	C_{N_B}	$C_{N_B(T)}$	\bar{X}_M/d	$R_{T(B)}$	$\frac{\bar{X}_{T(B)}}{d}$ *	$\frac{\bar{Y}_{T(B)}}{b/2}$	$C_{N_{BT}}$	$C_{M_{BT}}$
0	.0000	.4125	-.0943	.0000	.0000	.0000	-1.0584	0.9270	-.9864	.420	.0000	.0000
5	.1420	.4000	-.1038	.0571	.7020	.1240	-1.0584	0.9270	-.9933	.420	.2666	.4858
7	.2016	.4030	-.1076	.0920	.9779	.1736	-1.0584	1.0215	-1.0035	.420	.3994	.6599
9	.2628	.4060	-.1114	.1321	1.2556	.2232	-1.0584	1.0485	-1.0136	.420	.5343	.8379
11	.3256	.4110	-.1152	.1764	1.5444	.2728	-1.0584	1.0755	-1.0256	.420	.6767	1.0224
13	.3900	.4180	-.1190	.2255	1.8202	.3224	-1.0584	1.1025	-1.0395	.420	.8272	1.1886
15	.4560	.4250	-.1228	.2795	2.1126	.3720	-1.0584	1.1295	-1.0533	.420	.9861	1.3665

* measured from moment reference center

NCSG 17-238-78

- (7) Find the appropriate value of C_{d_c} for each local section at each crossflow Reynolds number from figure 18. In this example $C_{d_c} = 0.290$ throughout.
- (8) Use equation (15) to find $C_{N_{n1}}$.
- (9) Add result from step (4) to result from step (8) to find C_{N_B} .

Since this configuration is the one used as the detailed numerical example in Section V.2, only the final values of C_{N_B} are listed in Table II.

C_{M_B} (Section V.3)

- (1) From figure 25, $(K_2 - K_1) = 0.898$
- (2) From figure 26, $K_m = 0.940$
- (3) Using figure 17 of Section V.2, $x_{sa}/l_b = 0.455$. Since $l_b/d = 2$ for base B2, $x_{sa}/d = 0.910$, measured from the start of the base section. Measured from the nose, $x_{sa}/d = 5.91 \rightarrow x_{sa} = 3.4475$ ft. This is the upper limit of integration in equation (26).
- (4) Substituting the necessary quantities into equation (26) and carrying out the integration

$$C_{M_\alpha} = 8.043 \text{ rad}^{-1}$$

- (5) From figure 27, $\eta = 0.635$
- (6) Find x_{sc}/d at 7° , 10° , 13° , from equation (28)

α°	x_{sc}/d
7	2.667
10	1.833
13	1.556

- (7) The crossflow-drag coefficient, from figure 18 of Section V.2 is 0.290 for all sections
- (8) The results of the integration of equation (27) are

α°	$C_{M_{n1}}$
7	-0.4367
10	-0.0091
13	+0.0963

The values in Table II were determined by linearly interpolating out to 13° and assuming a constant value of $C_{M_{n1}}$ beyond 13° .

C_{A_B} (Section V.4)

- (1) From figure 31, $C_{O_b} = 0.0258$
- (2) Using figure 32, $C_f = .00278$
- (3) From equation (31), $C_{O_f} = 0.0685$
- (4) Combining the results of steps (1) and (3),

$$(C_{A_B})_o = C_{O_b} + C_{O_f} = .0943$$

- (5) From figure 33, $a_1 = .109 \text{ rad}^{-1}$. Thus,

$$C_{A_B} = 0.0943 + .109 \alpha$$

The results are listed in Table II.

$C_{N_B(T)}$ (Section VII.2)

- (1) From figure 52, $[C_{N_B(T)}]_o$ is linear with a slope of 1.4209 rad^{-1}
- (2) $r_o/s = 3.5/(3.5 + 2.5) = 0.583$
 From figure 53, $f_1(r_o/s) = 1.00$

- (3) The correction factor for fin taper ratio from figure 54 is $f_2(\lambda) = 1.00$
- (4) From figure 55, $f_3(1_{LE}/d) = 1.00$
- (5) Using equation (39),

$$C_{NB(T)} = 1.4209 \alpha$$

The values of the carryover loading are tabulated in Table II.

$R_{T(B)}$ (Section VII.4)

- (1) From figure 57, $(R_0)_{d/b} = 0.927$
- (2) From figure 58, $\Delta_{AR} R_0 = 0.000$
- (3) From figure 59, $\Delta_{\lambda} R_0 = 0.000$
- (4) From figure 60, $\Delta_{Re} R_0 = 0.000$
- (5) From figure 61, $\Delta_1 R_0 = 0.000$

Thus $R_0 = 0.927$

- (6) From figure 62, $(R_1)_{d/b} = 0.0135$
- (7) From figure 63, $\Delta_{AR} R_1 = 0.000$
- (8) From figure 64, $\Delta_{\lambda} R_1 = 0.000$
- (9) From figure 65, $\Delta_{Re} R_1 = 0.000$
- (10) From figure 66, $\Delta_1 R_1 = 0.000$

Thus $R_1 = 0.0135 \text{ deg}^{-1}$

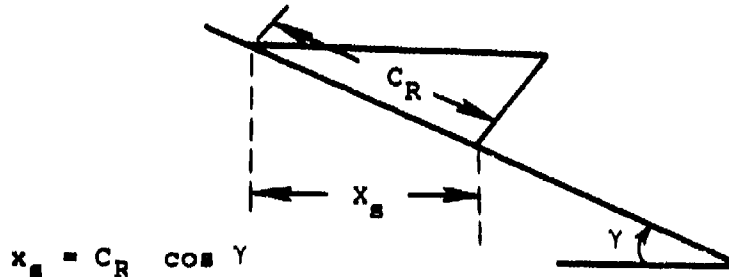
Combining these results,

$$R_{T(B)} = \begin{cases} 0.927 & \alpha \leq 5^\circ \\ 0.927 + 0.0135 \alpha & \alpha > 5^\circ \end{cases}$$

These results are listed in Table II.

\bar{x}_N (Section VII.3)

The body radius at the root chord leading edge is 3.5 in. To determine the body radius at the root chord trailing edge, first determine the axial length of the root chord. Referring to the sketch below



where γ is the half angle of the vortex of the cone planform.

For a two caliber base, $\gamma = 14.04^\circ$. Thus

$$\begin{aligned} x_s &= 6.665 \cos (14.04) \\ &= 6.465 \text{ in.} \end{aligned}$$

The equation for the base radial distribution is

$$r(x) = \frac{d}{2} \left(1 - \frac{x}{2d} \right)$$

starting at the beginning of the base section. Therefore, the body radius at the root-chord trailing edge is 1.884 in. The equation for the centroid of a trapezoid is

$$l_c = \frac{\Delta x}{3} \frac{2r_2 + r_1}{r_2 + r_1}$$

where

$$\begin{aligned} r_1 &= 3.5 \text{ in.} \\ r_2 &= 1.884 \text{ in.} \\ \Delta x &= 6.465 \text{ in.} \end{aligned}$$

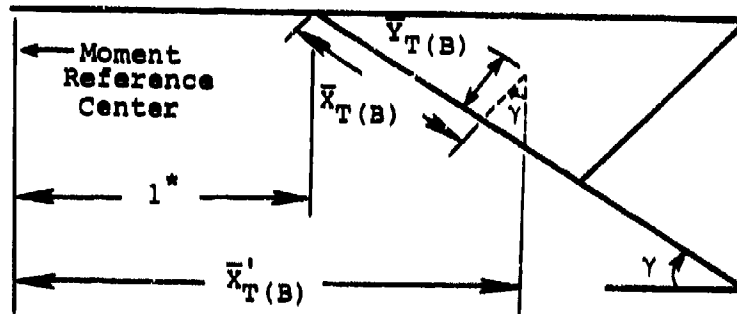
Substituting these values into the last equation, the axial distance of the centroid from x_{LE} is $l_c = 2.909$ in.

The axial distance between the moment reference center ($x_m = 30.5$ in.) and the root chord leading edge (start of base section) is 4.5 in. Hence, \bar{x}_N/d , the distance between the moment reference and the centroid is

$$\bar{x}_N/d = \frac{4.5 + 2.909}{7} = 1.0584$$

$\bar{x}_{T(B)}$ (Section VII.5)

There are two steps to the determination of $\bar{x}_{T(B)}$. The first is the application of the correction given in figure 70 to \bar{x}_T . The second is the conversion of this result to axial distances from the moment reference center. The procedure for the first part is outlined in Section VII.5. To determine the axial distance from the moment reference center, refer to the following sketch.



The equation for $\bar{x}_{T(B)}/d$, measured from the moment reference center, then is

$$\frac{\bar{x}'_{T(B)}}{d} = \frac{\cos \gamma}{d} \left\{ \frac{\bar{x}_{T(B)}}{C_R} C_R + \tan \gamma \frac{y_{T(B)}}{b/2} b/2 \right\} + \frac{l^*}{d}$$

The value of $y_{T(B)}/b/2$ is given below. Applying this equation to the values of $\bar{x}_{T(B)}$ the results given in Table II are obtained.

$\bar{y}_{T(B)}$ (Section VII.6)

(1) $r/s = 0.583$

(2) From figure 70, $\frac{\bar{y}_{T(B)}}{b/2} = 0.420$, independent of angle of attack.

The value of $\bar{Y}_{T(B)}$ is required to determine the axial distance from the moment reference to $\bar{X}_{T(B)}$ and is given in Table II.

Total Body-Tail Normal-Force Coefficient

The total body-tail normal-force coefficient, $C_{N_{BT}}$, is given by the following relation for undeflected fins.

$$C_{N_{BT}} = C_{N_B} + \sum_{i=1}^2 \left[C_{N_T} R_{T(B)i} \right] \frac{S_T}{S_R} + C_{N_{B(T)}} \quad (53)$$

In making comparisons to the present test, due to flow and model symmetry it can be assumed that

$$R_{T(B)1} = R_{T(B)2} = R_{T(B)} \quad (54)$$

Hence

$$C_{N_{BT}} = C_{N_B} + 2C_{N_T} R_{T(B)} \frac{S_T}{S_R} + C_{N_{B(T)}} \quad (55)$$

Combining the relevant values in Table II, the variation of $C_{N_{BT}}$ with angle of attack is obtained. This variation

is tabulated in Table II and is compared with experimental results in figure 75. Agreement between method and experiment is very good except at the medium values of angle of attack where the method over-predicts $C_{N_{BT}}$. A detailed

examination of the individual loads contributing to $C_{N_{BT}}$ revealed that most of the error was from C_{N_B} . It is

possible that the body-alone normal-force coefficient may require an angle of attack term of higher order than the present α^2 . Additional comparisons are given in figures 76, 77 and 78. These configurations were chosen to show the effects of fin position (figures 75 and 76), base (figures 75 and 77), and fin span (figures 77 and 78). The agreement in figures 76 and 77 is excellent but the effect of fin span, shown in figure 78, is somewhat over-predicted.

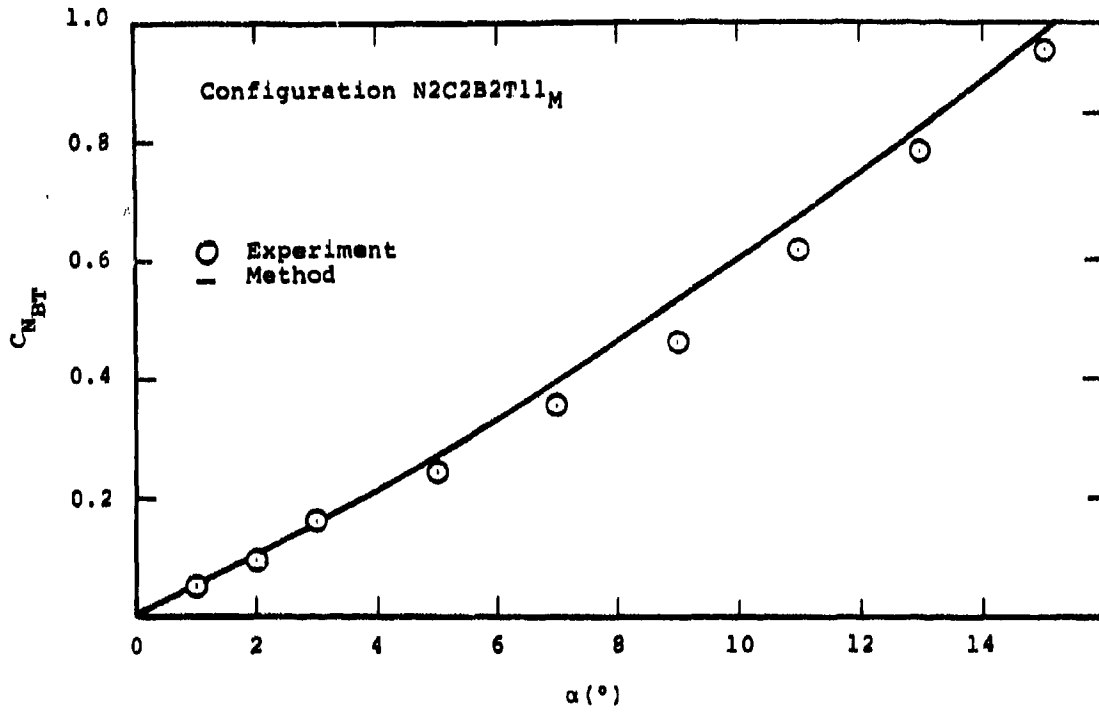


FIGURE 75. COMPARISON BETWEEN PREDICTED AND EXPERIMENTAL TOTAL BODY-TAIL NORMAL FORCE COEFFICIENT.

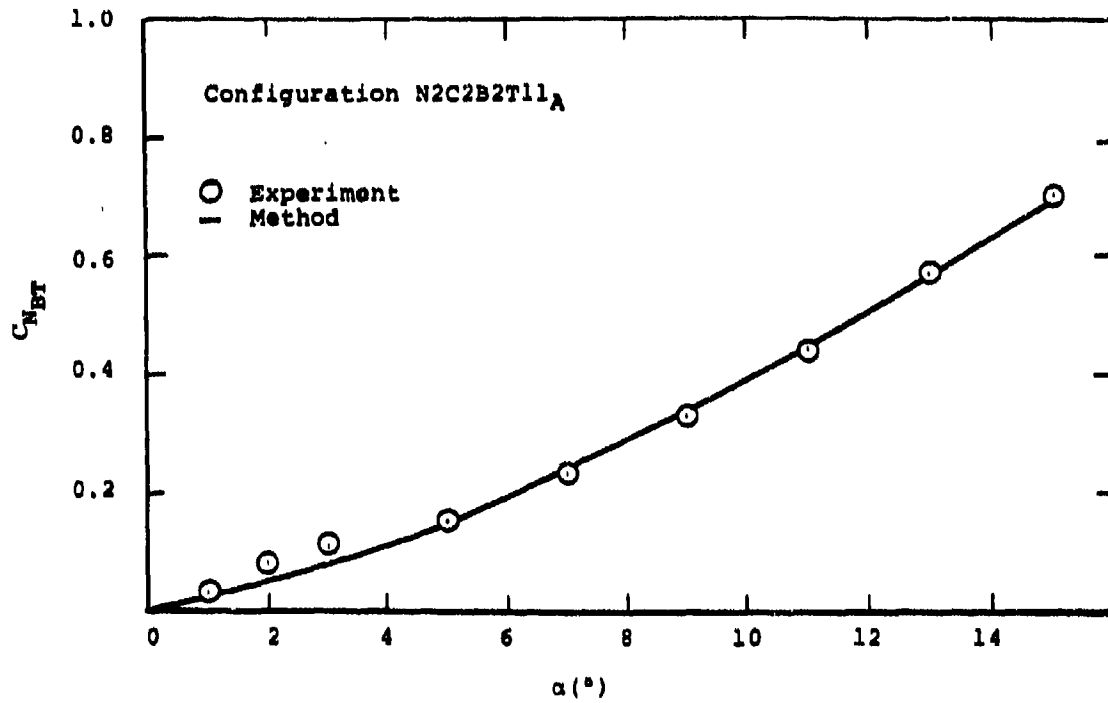


FIGURE 76. COMPARISON BETWEEN PREDICTED AND EXPERIMENTAL TOTAL BODY-TAIL NORMAL FORCE COEFFICIENT.

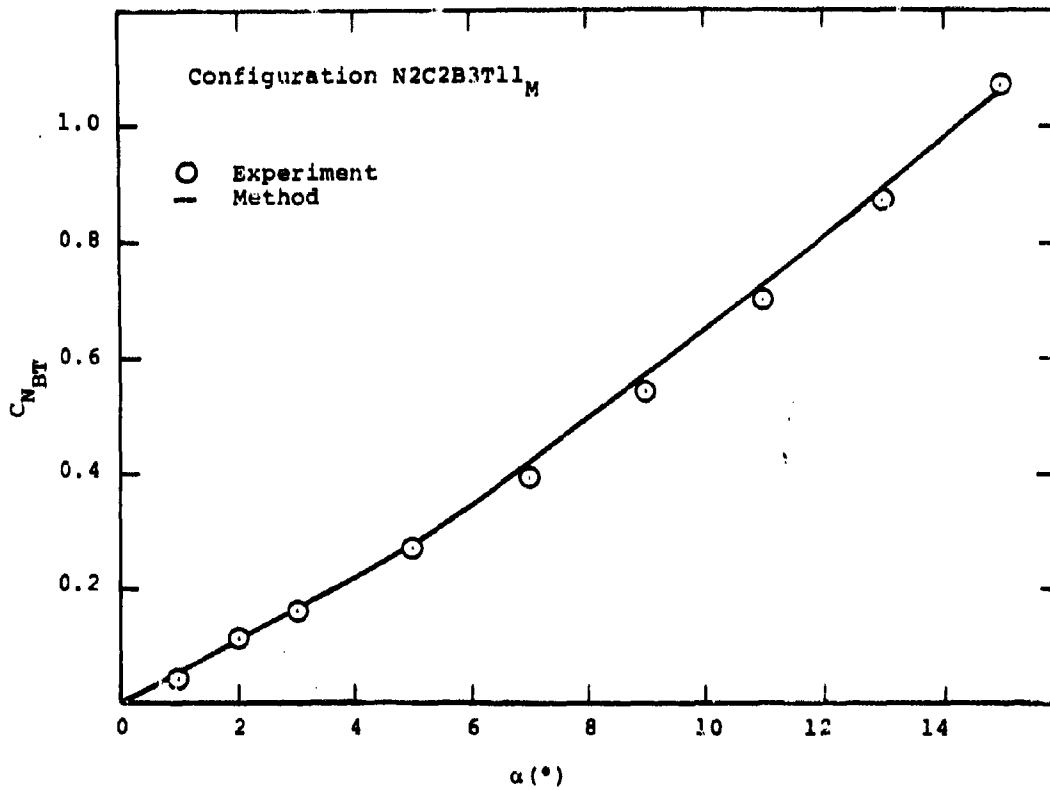


FIGURE 77. COMPARISON BETWEEN PREDICTED AND EXPERIMENTAL TOTAL BODY-TAIL NORMAL FORCE COEFFICIENT.

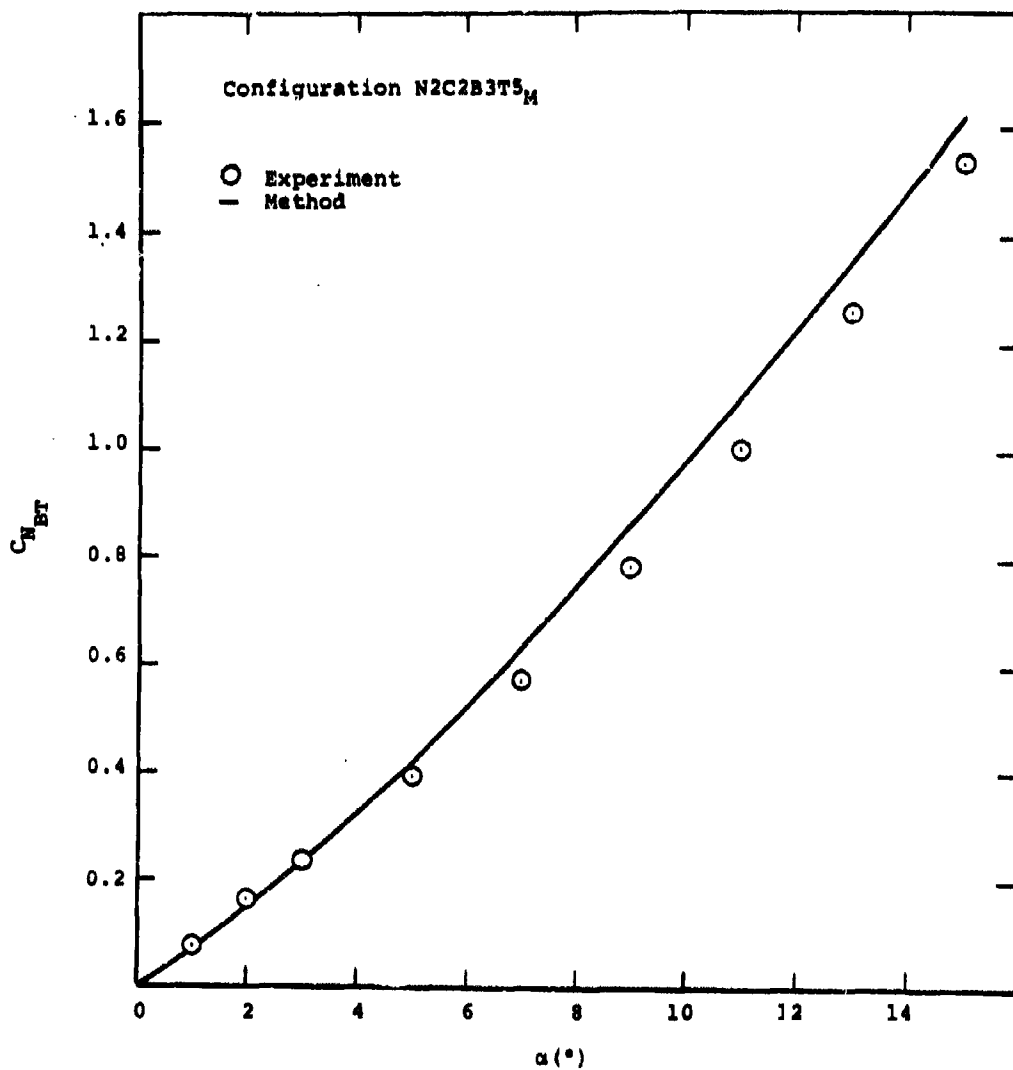


FIGURE 78. COMPARISON BETWEEN PREDICTED AND EXPERIMENTAL TOTAL BODY-TAIL NORMAL FORCE COEFFICIENT.

Total Body-Tail Pitching-Moment Coefficient

The total body-tail pitching-moment coefficient, $C_{M_{BT}}$, is given by the following relation for undeflected fins.

$$C_{M_{BT}} = C_{M_B} + \sum_{i=1}^2 \left[C_{N_T R_{T(B)}} \right]_i \frac{\bar{X}_{T(B)}_i}{d} \frac{S_T}{S_R} + C_{N_B(T)} \frac{\bar{X}_N}{d} \quad (56)$$

Making the assumption that

$$\bar{X}_{T(B)}_1 = \bar{X}_{T(B)}_2 = \bar{X}_{T(B)} \quad (57)$$

and combining equations (54), (56), and (57) yields

$$C_{M_{BT}} = C_{M_B} + 2C_{N_T R_{T(B)}} \frac{\bar{X}_{T(B)}}{d} \frac{S_T}{S_R} + C_{N_B(T)} \frac{\bar{X}_N}{d} \quad (58)$$

These values are also tabulated in Table II.

The comparison with experiment is shown in figure 79. Agreement is excellent throughout the angle of attack range. Additional comparisons are given in Figures 80, 81, and 82 for the same configurations previously shown in 76-78, respectively. The effect of fin position is only slightly over-predicted in figure 80 and the effect of a different base is handled well in figure 81. However, the effect of fin span on $C_{M_{BT}}$, figure 82, appears to be

substantially under-predicted. By comparing figures 81 and 82, it is seen that the effect of larger fins is to greatly reduce the value of $C_{M_{BT}}$. Thus, it appears possi-

ble that the cause of the discrepancy in figure 82 is the over-prediction of $C_{M_{T(B)}}$, the pitching moment due to the

tail in the presence of the body. Referring to equation (58), $C_{M_{T(B)}}$ is the second term on the right hand side

and all the components that make-up $C_{M_{T(B)}}$ are well

predicted. Thus, the cause of the discrepancy must lie in either C_{M_B} or $C_{M_{B(T)}}$. Examining the last term first,

both $C_{N_{B(T)}}$ and \bar{X}_N are reasonably well predicted.

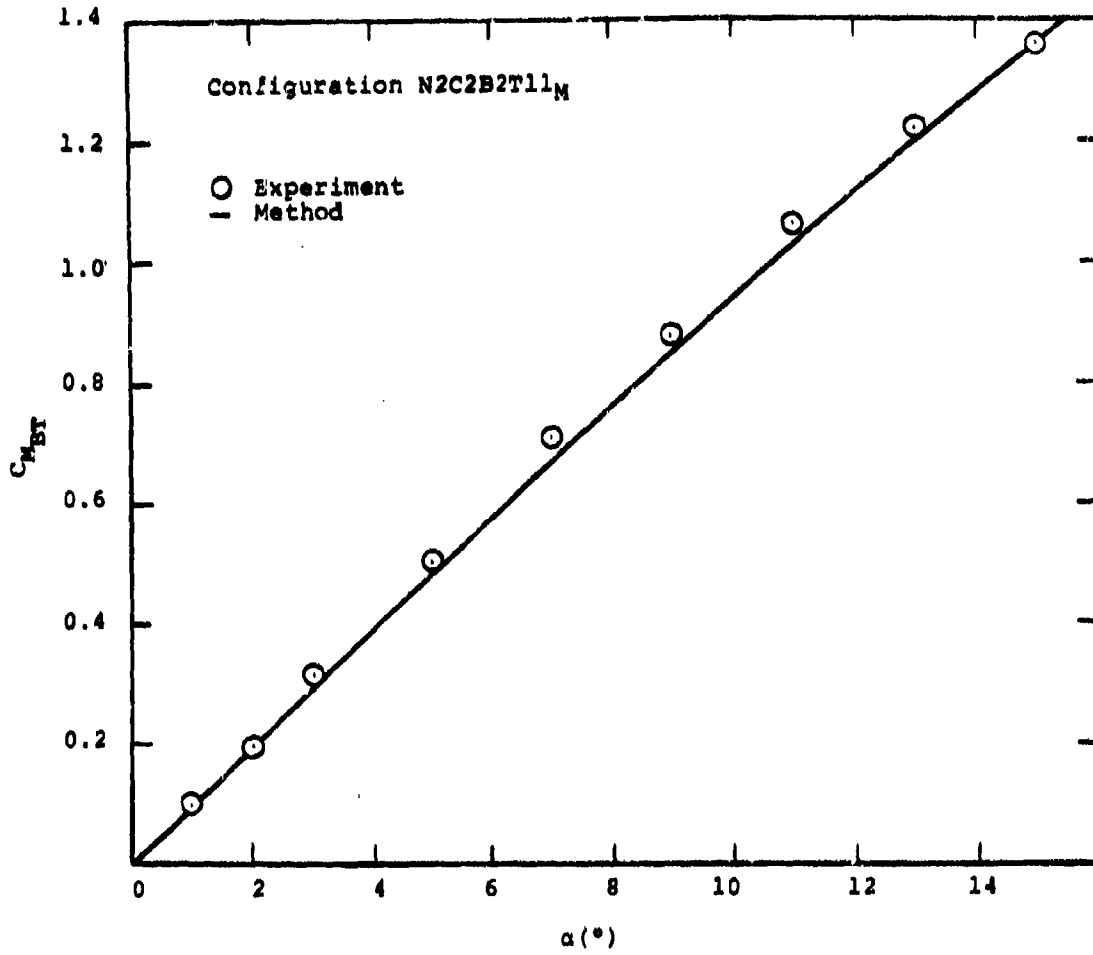


FIGURE 79. COMPARISON BETWEEN PREDICTED AND EXPERIMENTAL TOTAL BODY-TAIL PITCHING MOMENT COEFFICIENT.

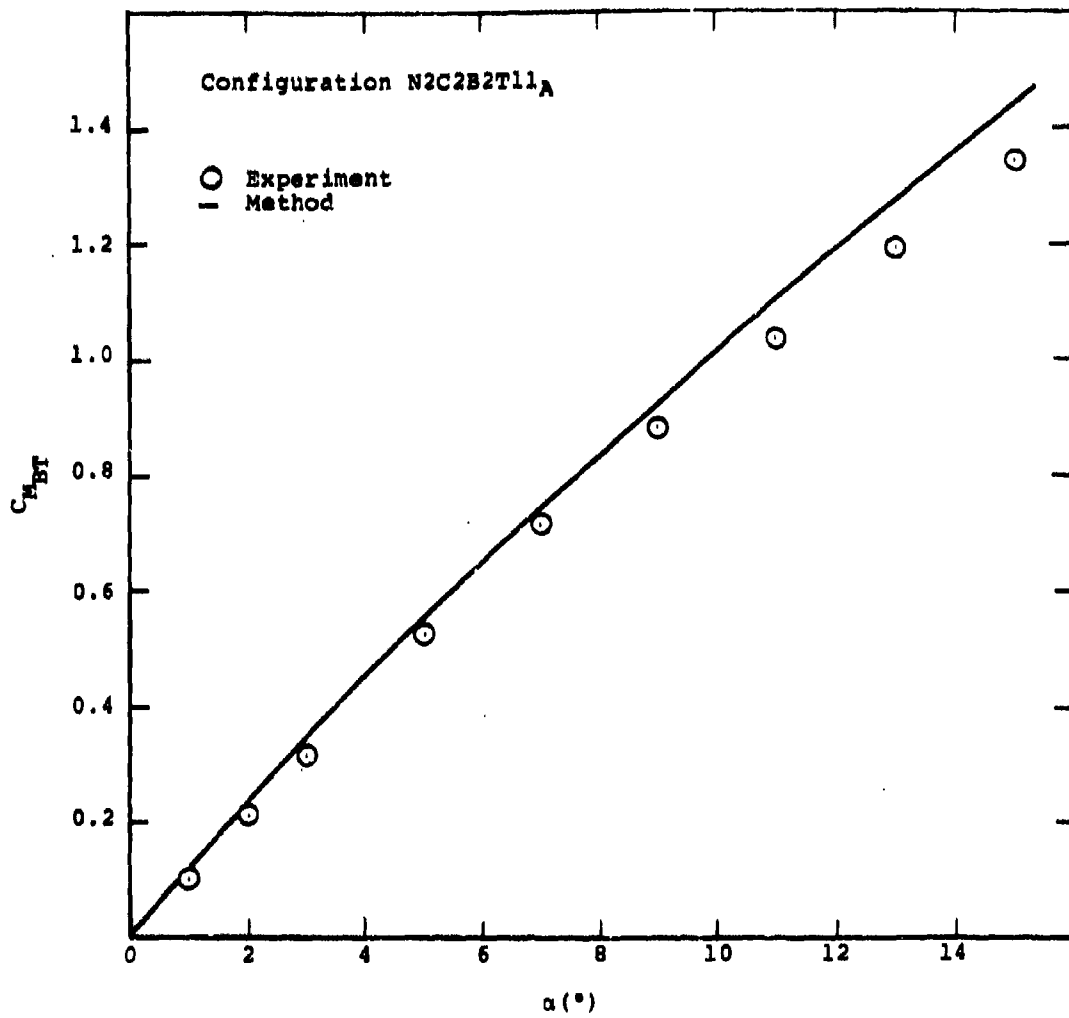


FIGURE 80. COMPARISON BETWEEN PREDICTED AND EXPERIMENTAL TOTAL BODY-TAIL PITCHING MOMENT COEFFICIENT.

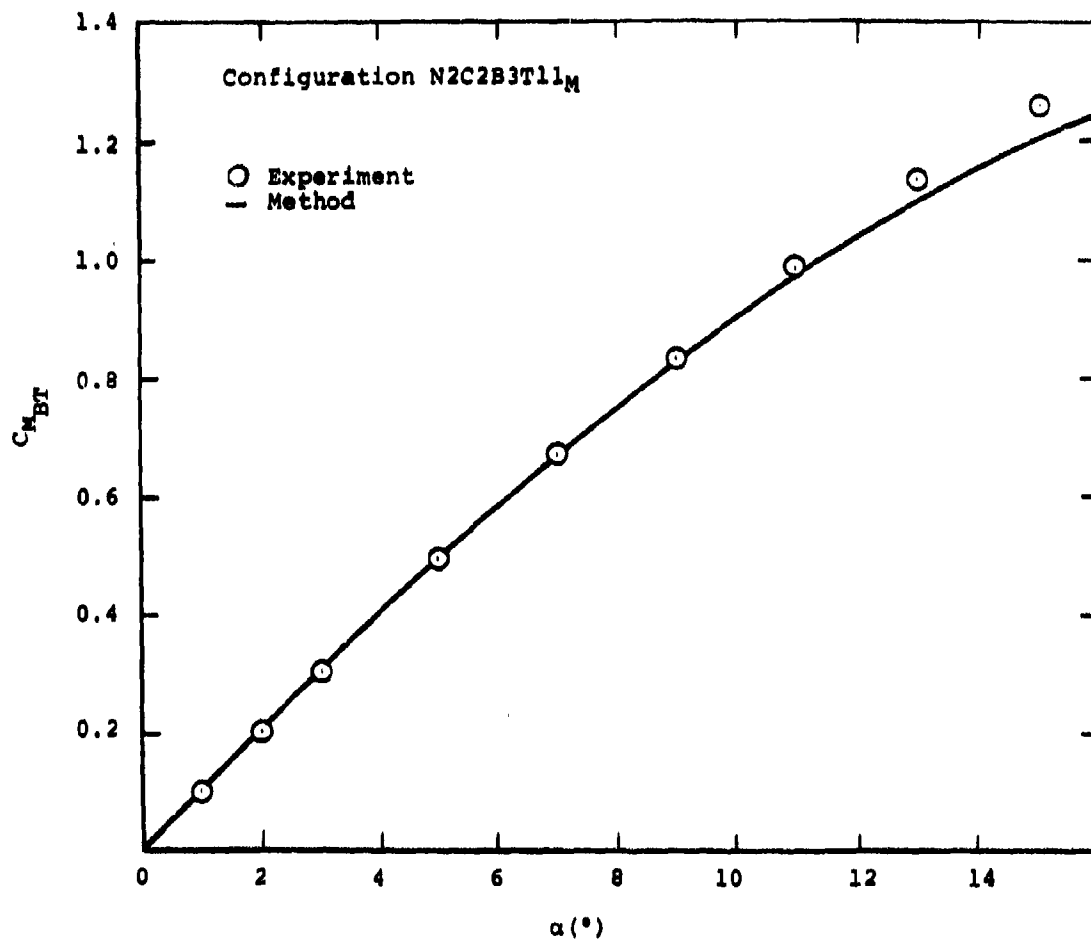


FIGURE 81. COMPARISON BETWEEN PREDICTED AND EXPERIMENTAL TOTAL BODY-TAIL PITCHING MOMENT COEFFICIENT.

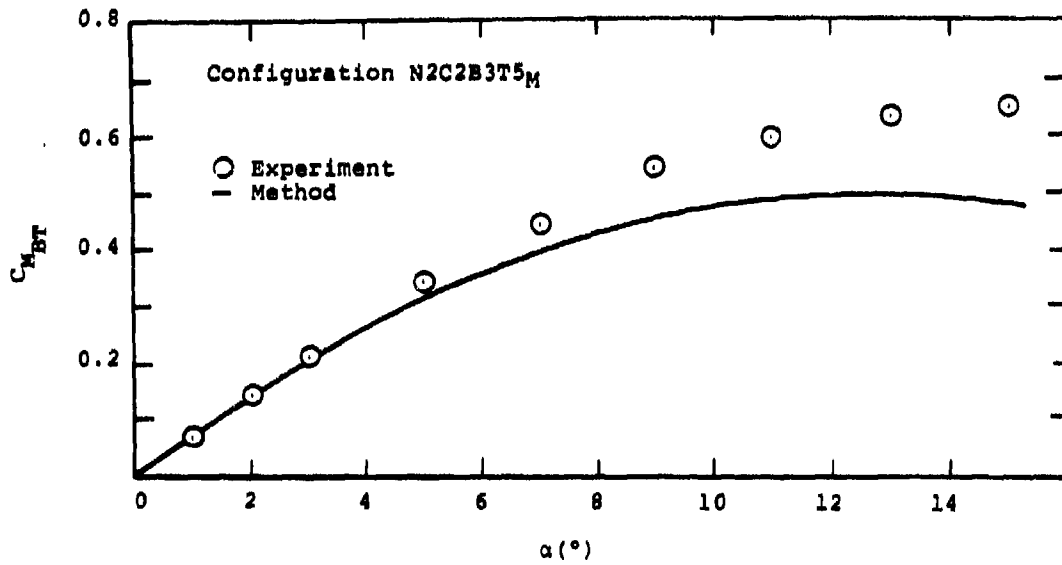


FIGURE 82. COMPARISON BETWEEN PREDICTED AND EXPERIMENTAL TOTAL BODY-TAIL PITCHING MOMENT COEFFICIENT.

Therefore, by process of elimination, the discrepancy is due to the prediction of C_{M_B} . Recalling the method for estimating C_{M_B} , comparisons with data showed that the experimental values of the nonlinear term were slightly more negative than the values found by applying the method. However, in figure 82 just the opposite is the case. The methods for C_{M_B} and C_{N_B} use an effective separation point concept. If this effective separation point were to move downstream when the fins were attached then there would be additional loading over the aft portion of the body that has not been accounted for in the present methods. This would increase the total pitching moment over the prediction, consistent with the data.

VIII. CONCLUSIONS AND RECOMMENDATIONS

The work described in this report demonstrates the utility and power of the systematical experimental approach to semi-empirical prediction method construction. Through a combination of experiment and theory, methods are now available for estimating, with good accuracy, the hydrodynamic characteristics of certain types of submersible vehicles. At present the methods are applicable only to vehicles having undeflected, cruciform tails, at pitch angles of attack to 15 degrees. The techniques can be easily extended to deflected tails through generation and correlation of appropriate data. The models as fabricated will permit systematic tail deflections. In this way, the return on initial investment can be considerably increased.

With developments in vehicle performance requirements, it may become necessary to maneuver at combined pitch and roll, or yaw, or to deploy forward control surfaces to enhance maneuverability or stationkeeping. The models, at present, are not flexible enough to permit testing of such concepts. However, they can be made to do so in a relatively straightforward manner.

The most obvious required extension to the developed methods is the addition of propulsion effects. To accomplish this would require considerable modification. It is thought that in view of the configurational developments which may be desirable, the addition of power would best be postponed until some of the other concepts mentioned above have been investigated.

Recommendations

It is recommended that the following developments of this initial work be considered:

- i) Modify the models such that forward controls and combined pitch-roll attitudes can be attained. Mount the forward controls on individual balances. Automate attitude and deflection changes to the greatest extent possible. In this way, test time will be reduced and data quantity increased.

- ii) Modify the models such that power effects are included. This may be done following i), or immediately. A systematic investigation of power parameters will be necessary for a wide range of geometric configurations and it may be thought advisable to postpone this step until i) has been completed.

REFERENCES

1. Fidler, J. E. and Bateman, M. C., "Aerodynamic Methods for High Incidence Missile Design", *AIAA, J. of Spacecraft & Rockets*, vol. 12, no. 3, March 1975.
2. NACA Rept. No 1307, *Lift and Center of Pressure of Wing-Body-Tail Combinations at Subsonic, Transonic, and Supersonic Speeds*, by W. C. Pitts, J. N. Nielsen, and G. E. Kaattari, 1957.
3. Martin Marietta Corp. Rept. OR 12,399, *Aerodynamic Methodology (Isolated Fins and Bodies)*, by J. E. Fidler and M. C. Bateman, 1973.
4. NACA Rept. No. 1048, *A Study of Effects of Viscosity on Flow Over Slender Inclined Bodies of Revolution*, by H. J. Allen and E. W. Perkins, 1951.
5. NACA Rept. No. 184, *The Aerodynamic Forces on Airship Hulls*, by M. M. Munk, 1924.
6. NEAR Inc., *Methods for Predicting Submersible Hydrodynamic Characteristics - Initial Data Analysis*, by J. E. Fidler, and J. N. Nielsen, Contract No. N61339-76-C-0076, 1976.
7. NACA RM A51C14, *A Semi-empirical Method for Calculating the Pitching Moment of Bodies of Revolution at Low Mach Numbers*, by E. J. Hopkins, 1951.
8. NASA CR-2473, *Effect of Symmetrical Vortex Shedding on the Longitudinal Aerodynamic Characteristics of Wing-Body-Tail Combinations*, by M. R. Mendenhall and J. N. Nielsen, 1975.
9. NASA TN D-6996, *Prediction of Static Aerodynamic Characteristics for Space-Shuttle-like and Other Bodies at Angles of Attack from 0° to 180°*, by L. H. Jorgensen, 1973.

10. United States Air Force Stability and Control Datcom, 1975.
11. Office of Naval Research Report No. ONR-CR215-226-3, *Calculation of Component Forces and Moments of Arbitrarily Banked Cruciform Missiles with Control Deflections*, by M. J. Hensch, C. A. Smith, J. N. Nielsen, and S. C. Perkins, Jr., 1976.
12. Goldstein, S., *Modern Developments in Fluid Dynamics*, Dover Publications, New York, 1965.
13. Hoerner, S. F., *Fluid-Dynamic Drag*, Brick Town, New Jersey, 1965.
14. Schoenherr, "Resistance of Plates", *Transactions, Society of Naval Architects and Marine Engrg.*, 1932.
15. Cornell Aeronautical Laboratory Rept. No. CAL-37, *The Aerodynamics of Low-Aspect-Ratio Wings and Wing-Body Combinations*, by A. H. Flax and H. R. Lawrence, 1951.
16. Hoerner, S. F., *Fluid-Dynamic Lift*, published by Mrs. L. A. Hoerner, Brick Town, New Jersey, 1975.
17. NACA RM L52G18, *Investigation of the Effects of Variations in the Reynolds Number Between 0.4×10^6 and 3.0×10^6 on the Low-Speed Aerodynamic Characteristics of Three Low-Aspect-Ratio Symmetrical Wings with Rectangular Plan Forms*, by G. W. Jones, Jr., 1952.
18. IAS Preprint No. 313, *The Lift Distribution on Low-Aspect-Ratio Wings at Subsonic Speeds*, by H. R. Lawrence, 1951.
19. Cornell Aeronautical Laboratory Rept. No. CAL-62, *Experimental Investigation of Influence of Edge Shape on the Aerodynamic Characteristics of Low-Aspect-Ratio Wings at Low Speeds*, by G. E. Bartlett and R. J. Vidal, 1954.
20. NACA TM 1176, *Test Report on Three- and Six-Component Measurements on a Series of Tapered Wings of Small Aspect Ratio (Partial Rept: Triangular Wing)*, by Lange/Wacke, 1948.

21. NACA TN 1650, *Chordwise and Spanwise Loadings Measured at Low Speed on a Triangular Wing Having an Aspect Ratio of Two and an NACA 0012 Airfoil Section*, by B. H. Wick, 1948.
22. Nielsen, J. N., *Missile Aerodynamics*, McGraw-Hill, Inc., New York, 1960.
23. Martin Marietta Rept. OR 13,375-1, *Aerodynamic Methodology: Bodies with Tails at Arbitrary Roll Angle*, by J. E. Fidler and M. C. Bateman, 1974.

NCSC REPORT TM-238-78

INITIAL DISTRIBUTION LIST

427	Commander, Naval Sea Systems Command (SEA 032)	(Copy 1)
	(SEA 034)	(Copy 2)
	(SEA 035, Dr. T. Peirce)	(Copy 3)
	(SEA 03513, Mr. L. Pasiuk)	(Copy 4)
	(SEA 92)	(Copy 5)
	(FMS 393)	(Copy 6)
	(FMS 395)	(Copy 7)
	(Library)	(Copy 8)
1	Chief of Naval Material (MAT 08T23, Mr. Vittucci, Mr. Remson, Mr. Romano)	(Copies 9-11)
5	Commander, Naval Ship Engineering Center (Library)	(Copy 12)
	(Code 6136, Mr. Keane, Mr. Louis, Mr. Goldstein, Mr. Jones)	(Copies 13-16)
236	Commander, David Taylor Naval Ship R&D Center (Library)	(Copy 17)
	(Code 1564, Dr. Feldman, Mr. Sheridan)	(Copy 18-19)
	(Code 1548, Mr. Folb)	(Copy 20)
266	Commanding Officer, Naval Underwater Systems Center (Library)	(Copy 21)
	(Mr. Goodrich)	(Copy 22)
	(Mr. Nadolink)	(Copy 23)
265	Commander, Naval Oceans Systems Center (Code 5332)	(Copy 24)
	(Code 6302)	(Copy 25)
	(Library)	(Copy 26)
484	Director, Naval Research Laboratory (Library)	(Copy 27)
210	Commander, Naval Surface Weapons Center, White Oak (Mr. M. Krimins)	(Copy 28)
	(Library)	(Copy 29)
463	Commander, Naval Surface Weapons Center, Dahlgren (DK 21, Dr. F. Moore)	(Copy 30)
	(Library)	(Copy 31)
154	Superintendent, Naval Academy, Annapolis (Library)	(Copy 32)
222	Superintendent, Naval Postgraduate School, Monterey (Library)	(Copy 33)
54	Chief of Naval Research (ONR 211, Dr. Siegel)	(Copy 34)
	(ONR 438, Mr. Cooper)	(Copy 35)
	(ONR 211, Dr. Whitehead)	(Copy 36)
	(ONR 202, CDR R. Parisean)	(Copy 37)
268	Commander, Naval Weapons Center, China Lake (Code 4063, Mr. R. E. Meeker)	(Copy 38)
162	Commander, Naval Air Systems Command (AIR 320C)	(Copy 39)
---	Commanding Officer, Eglin Air Force Base (AFATL, DLMI, Mr. C. B. Butler)	(Copy 40)

NCSC REPORT TM-238-78

---	Commanding Officer, Picatinny Arsenal, Dover, NJ 07801 (Applied Sciences Div., Fluid Mechanics Branch, Mr. A. A. Loeb)	(Copy 41)
---	Commanding Officer, Redstone Arsenal, U. S. Army Missile R&D Command (DRDMK-TDK, Mr. Ray Deep)	(Copy 42)
---	Ames Research Center, National Aeronautics and Space Administration (MP 227-8, Dr. Gary Chapman)	(Copy 43)
	(MS 227-5, Mr. F. Steinle)	(Copy 44)
	(MS 202-3, Library)	(Copy 45)
---	Langley Research Center, National Aeronautics and Space Administration (MC 360, Mr. P. Roffitt)	(Copy 46)
	(MS 406, Mr. C. Jackson)	(Copy 47)
---	National Aeronautics and Space Administration, Washington (Code RAA, Mr. A. Gessow)	(Copy 48)
---	Stevens Institute of Technology, Davidson Laboratory, Hoboken, NJ 07030 (Library)	(Copy 49)
	(Dr. Al Strumpf)	(Copy 50)
11	Applied Research Laboratory, Penn State University (Library)	(Copy 51)
	(Mr. W. R. Hall)	(Copy 52)
19	Applied Research Laboratory, University of Texas (Library)	(Copy 53)
664	Applied Physics Laboratory, Johns Hopkins University (Library)	(Copy 54)
	(Dr. W. Venezia)	(Copy 55)
---	Virginia Polytechnical Institute, Blacksburg, VA 24061 (Library)	(Copy 56)
---	Massachusetts Institute of Technology, Cambridge, MA 02139 (Library)	(Copy 57)
	(Dr. Abkowitz)	(Copy 58)
---	Library of Congress, Washington (Science & Technology Library)	(Copy 59)
340	Director, Woods Hole Oceanographic Institute	(Copy 60)
302	Director, Scripps Institute of Oceanography	(Copy 61)
621	Commanding Officer, Naval Oceans Research & Dev. Activity	(Copy 62)
---	Society of Naval Architects and Marine Engineers (SNAMNE) 74 Trinity Pl., New York, NY 10006	(Copy 63)
77	Director of Defense Research & Engineering, Washington	(Copy 64)
6	Director, Advanced Research Projects Agency, Washington	(Copy 65)
---	The Analytical Sciences Corp., 6 Jacob Way, Reading, MA 01867 (Library)	(Copy 66)
75	Director, Defense Documentation Center	(Copies 67-78)